

## **YEAR END TECHNICAL REPORT**

August 29, 2016 to September 28, 2017

# **Chemical Process Alternatives for Radioactive Waste**

**Date submitted:**

November 3, 2017

**Principal Investigator:**

Leonel E. Lagos, Ph.D., PMP®

**Florida International University Collaborators:**

Dwayne McDaniel, Ph.D., P.E. (Project Manager)

Amer Awwad, M.S., P.E.

Anthony Abrahao, M.S.

Ahmadreza Abbasi Baharanchi, Ph.D.

Aparna Aravelli, Ph.D.

William Tan, Ph.D.

DOE Fellows

**Prepared for:**

U.S. Department of Energy

Office of Environmental Management

Under Cooperative Agreement DE-EM00000598



**Applied Research Center**

FLORIDA INTERNATIONAL UNIVERSITY

This document represents one (1) of four (4) reports that comprise the Year End Reports for the period of August 29, 2016 to September 28, 2017 prepared by the Applied Research Center at Florida International University for the U.S. Department of Energy Office of Environmental Management (DOE-EM) under Cooperative Agreement No. DE-EM0000598.

The complete set of FIU's Year End Reports for this reporting period includes the following documents:

Project 1: Chemical Process Alternatives for Radioactive Waste  
Document number: FIU-ARC-2017-800006470-04b-255

Project 2: Environmental Remediation Science and Technology  
Document number: FIU-ARC-2017-800006471-04b-254

Project 3: Waste and D&D Engineering and Technology Development  
Document number: FIU-ARC-2017-800006472-04b-245

Project 4: DOE-FIU Science & Technology Workforce Development Initiative  
Document number: FIU-ARC-2017-800006473-04b-253

Each document will be submitted to OSTI separately under the respective project title and document number as shown above.

### **DISCLAIMER**

This report was prepared as an account of work sponsored by an agency of the United States government. Neither the United States government nor any agency thereof, nor any of their employees, nor any of its contractors, subcontractors, nor their employees makes any warranty, express or implied, or assumes any legal liability or responsibility for the accuracy, completeness, or usefulness of any information, apparatus, product, or process disclosed, or represents that its use would not infringe upon privately owned rights. Reference herein to any specific commercial product, process, or service by trade name, trademark, manufacturer, or otherwise does not necessarily constitute or imply its endorsement, recommendation, or favoring by the United States government or any other agency thereof. The views and opinions of authors expressed herein do not necessarily state or reflect those of the United States government or any agency thereof.

# TABLE OF CONTENTS

---

TABLE OF CONTENTS.....	i
LIST OF FIGURES .....	iii
LIST OF TABLES .....	viii
PROJECT 1 OVERVIEW .....	1
TASK 17.1.1 CFD MODELING OF NON-NEWTONIAN FLUIDS (FIU YEAR 7) .....	3
EXECUTIVE SUMMARY .....	3
NON-NEWTONIAN CFD MODELING .....	4
MODELING OF RETRIEVAL PROCESSES .....	11
PIPELINE FLUSHING .....	20
CONCLUSIONS.....	28
TASK 17.1.2 CFD MODELING OF NON-NEWTONIAN FLUID UNDERGOING SPARGING (FIU YEAR 7).....	30
EXECUTIVE SUMMARY .....	30
INTRODUCTION .....	31
LITERATURE REVIEW .....	32
NUMERICAL APPROACH .....	35
RESULTS & DISCUSSIONS .....	38
CONCLUSIONS AND FUTURE WORK .....	47
TASK 18.2 DEVELOPMENT OF INSPECTION TOOLS FOR DST PRIMARY TANKS (FIU YEAR 7) .....	50
EXECUTIVE SUMMARY .....	50
INTRODUCTION .....	52
MAGNETIC MINIATURE ROVER .....	53
PNEUMATIC PIPE CRAWLER .....	70
DST FULL SCALE SECTIONAL MOCKUP .....	75
CONCLUSIONS AND FUTURE WORK .....	82
TASK 18.3 INVESTIGATION USING AN INFRARED TEMPERATURE SENSOR TO DETERMINE THE INSIDE WALL TEMPERATURE OF DSTS (FIU YEAR 7).....	84
EXECUTIVE SUMMARY .....	84
INTRODUCTION .....	85
SENSOR VALIDATION TESTS.....	86
SENSOR INTEGRATION WITH INSPECTION TOOLS .....	90
CONCLUSIONS AND FUTURE WORK .....	92
REFERENCES .....	93
TASK 19.1 PIPELINE CORROSION AND EROSION EVALUATION (FIU YEAR 7) .....	94

EXECUTIVE SUMMARY .....94  
 INTRODUCTION .....95  
 CONCLUSIONS.....103  
 REFERENCES .....104

TASK 19.2 EVALUATION OF NONMETALLIC COMPONENTS IN THE  
 WASTE TRANSFER SYSTEM (FIU YEAR 7).....105

EXECUTIVE SUMMARY .....105  
 INTRODUCTION .....106  
 EXPERIMENTAL TESTING .....107  
 CONCLUSIONS AND FUTURE WORK .....115  
 REFERENCES .....116

## LIST OF FIGURES

---

Figure 1. Turbulent velocity profile for the transitional case. ....	6
Figure 2. Turbulent velocity profile for the fully turbulent case. ....	7
Figure 3. Variation of shear rate versus different ratios. ....	8
Figure 4. Contour and profile of mean and turbulent axial velocity profiles, $Re = 25300$ . ....	8
Figure 5. Shear dependency on $u_{rms}/\eta$ and $TDR/TKE$ , $Re = 25300$ . ....	9
Figure 6. Structures found in core flow which belong to top envelope in Figure 5(b). ....	9
Figure 7. Axial velocity for modified RANS-HB and other RANS simulations. ....	10
Figure 8. Interactions of liquid, suspended solids and settled solid fields during tank mixing operations, image and description from Rector et al., (2010). ....	12
Figure 9. Mesh and initialization of a multiple region domain created in Star-CCM+. ....	14
Figure 10. 2D computational domain created for the 1:21 scaled tank with 43” internal diameter. ....	15
Figure 11. 3D computational domain created for the 1:21 scaled tank with 43” internal diameter. ....	15
Figure 12. Multiphase simulation of jet flow in a multi-region domain. ....	16
Figure 13. Initial conditions for simulation of jet flow in a multi-region domain. ....	16
Figure 14. Evolution of flow from 0 sec to 60 sec, contour of solid volume fraction. ....	17
Figure 15. Velocity contour and vector filed in 2D simulation of 43” tank with MJP suction ports. ....	18
Figure 16. Velocity contour and vector filed in 2D simulation of 43” tank without MJP suction ports. ....	18
Figure 17. Velocity profile at the location of MJP and TRN suction ports, MJP port on (left) and off (right). ....	19
Figure 19. FIU’s proposed test loop. ....	26
Figure 20. FIU’s proposed variable-length loops (left) and an existing 270-ft pipeline at FIU (right). ....	26
Figure 22. General flow structure in PJM vessel (left), radial wall jet depiction (Poreh et al. 1967) (right). ....	31
Figure 23. Bubble column flow regime based on characteristic length and flow rate. ....	32
Figure 24. Boundary Conditions, physical characteristic (left) and Initial conditions (right) of Caixia Chen simulation. ....	38
Figure 25. Replication of Xe's simulation results compared to chen's experimental data. ....	39
Figure 26. Cross section view of mesh for parametric study. ....	39

Figure 27. Circumferentially time averaged (a) air volume fraction and (b) air axial velocity profile simulation results compared to Amin’s experimental data. .... 40

Figure 28. Developed simulation grid refinement study of the time averaged (a) air volume fraction (b) air axial velocity ..... 41

Figure 29. Instantaneous velocity at the center of the bubble column at a height of (a) 40% of liquid height and (b) 80% of liquid height. .... 42

Figure 30. H/D comparison (  $HD = 5.2 - .34$  ) of (a) air volume fraction and (b) air axial velocity at 40% of the liquid height..... 43

Figure 31. H/D comparison (  $HD = 5.2 - .34$  ) of (a) air volume fraction and (b) air axial velocity at 80% of the liquid height..... 44

Figure 32. Time averaged air volume fraction profile across a 2D plane for H/D= 5.8-.34 with a clip to range of .5 (not to scale). .... 44

Figure 33. Time averaged air volume fraction on an axial section view for (a)  $HD = .34$ , (b)  $HD = 3.8$ , (c)  $HD = 5.8$  at (1) 40% and (2) 80% of the liquid height. .... 46

Figure 34. Inspection entry points of the AY-102 double-shell tank. .... 52

Figure 35. Side view of primary tank and refractory air slot..... 53

Figure 36. Refractory air slot layout and description for AY-102..... 53

Figure 37. Refractory slot layout for Tank type AZ, SY, AW, AN and AP..... 54

Figure 38. The redesigned inspection tool without the hood. Both the camera and the LED lights are connected perpendicularly to the base-PCB. Three extra connector-pins (yellow) are added on the base-PCB to provide connections to the sensors. .... 54

Figure 39. Initial conceptual design with a temperature sensor attached (purple) to the top of the inspection tool. The design also includes a patch-LED inserted on the front PCB, replacing the bulb LED..... 55

Figure 40. CAD drawing showing various PCBs for the electronic components. .... 56

Figure 41. Conceptual design of temperature sensor integration for measuring the ambient temperature. .... 57

Figure 42. Conceptual design of iButton integration for measuring both the ambient temperature and humidity. .... 57

Figure 43. Conceptual design of radiation sensor integration for measuring beta, gamma and x-rays..... 57

Figure 44. Conceptual design of non-contact infrared temperature sensor for measuring the surface temperature of the tank bottom. The circular cutout (on right) through the inspection tool’s body allows the IR sensing element to be fitted to measure the surface temperature of the tank..... 57

Figure 45. Base, Camera and Sensors PCB designs. .... 58

Figure 46. Old inspection tool with wire cluttering issue (top) and new inspection tool with custom-made PCB (bottom). .... 58

Figure 47. (left) Sensor hoops populated with both the temperature and iButton sensors (left) and populated camera PCBs with both the patch and mixed LED lights for the lighting source of the mini inspection tool (right). ..... 59

Figure 48. Temperature sensor hood (left), inspection tool fitted with iButton humidity and temperature sensor (middle), and inspection tool fitted with RD2014 radiation sensor (right). The sensor hoods share common electrical and communication interfaces. .... 59

Figure 49. Waterproof controller box housing all the electronic components that interface with the inspection tool and operator (left) and box diagram showing the layout of the controller box (right). ..... 60

Figure 50. Xbox controller attached to the controller box to provide the operator with the option of controlling both the mini inspection tool and the cable management system manually. . 60

Figure 51. Ventilation channel proposed inspection..... 61

Figure 52. FIU’s robotic platform..... 61

Figure 53. Automated cable management systems..... 62

Figure 54. Automated cable management system dimensions. .... 62

Figure 55. Original cable management (left) and redesign prototype with winder (right). ..... 63

Figure 56. Redesigned cable management system with an active cable releasing capability. .... 63

Figure 57. Active cable feeding systems. .... 64

Figure 58. Prototype of the automated tether management system. .... 65

Figure 59. Cable management system equipped with active cable release capability..... 65

Figure 60. Image stream obtained from the onboard camera during a test in the mock up channel. Red lines show the wall boundaries while the dotted-green line is the estimated central line, with respect to the wall boundaries..... 66

Figure 61. Image processing pipeline for detecting the channel boundaries..... 67

Figure 62. Raw image from the camera (left) and processed image with the detected channel boundaries overlaid in green (right)...... 67

Figure 63. The control outputs of the PID controller..... 68

Figure 64. Full-scale sectional mock-up showing the starting and end point traversed by the mini inspection tool (left) and the experiment setup with operator’s computer, control box and cable management system (right). .... 69

Figure 65. Image capture of the inner concrete wall of the mock-up (left) and the mini inspection tool reaching the end of the refractory slot (right). ..... 69

Figure 66. AY-102 air supply lines..... 70

Figure 67. FIU’s pneumatic pipe crawler. .... 71

Figure 68. Pneumatic pipe crawler. .... 71

Figure 69. Current pneumatic pipe crawler prototype. .... 72

Figure 70. Sensor integration..... 73

Figure 71. New instrumentation module. .... 74

Figure 72. Crawler current pneumatic actuator (left) and considered pancake cylinder (right)... 74

Figure 73. Original mockup design. .... 75

Figure 74. Current mockup design..... 75

Figure 75. Existing configuration of the DST’s leak detection system. .... 76

Figure 76. Layout of the tank foundation drains (left) and cooling channels (right)..... 77

Figure 77. Concrete foundation with drain slots..... 77

Figure 78. Refractory pad with cooling channels. .... 78

Figure 79. Tank central plenum. .... 78

Figure 80. Mockup foundation and refractory pad concrete coating..... 79

Figure 81. Primary tank layout. .... 79

Figure 82. The full-scale HLW tank mockup. .... 80

Figure 83. Design of the refractory pad structure with cooling channels..... 81

Figure 84. Plywood boxes that form the refractory. .... 81

Figure 85. a) Experimental set up      b) tank covered with insulation..... 86

Figure 86. a) HSTs fixed under the plate      b) DAQ system with thermocouples      c) DAQ dashboard. .... 87

Figure 87. Emissivity experiment with Raytek sensor a) carbon steel plate b) stainless steel tank wall..... 88

Figure 88. IR sensor head on the rover: a) empty chassis b) actual rover in the tank channels c) detailed view. .... 90

Figure 89. IR sensor head attached at: a) front b) top (angular) c) rear..... 90

Figure 90. a) IR sensor head on the pneumatic pipe crawler b) sensor head and crawler inside the clear pipe. .... 91

Figure 91. (a) UT sensors, (b) Wireless network, and (c) Mounting system..... 97

Figure 92. (a) Permasense corrosion monitoring system and (b) Permasense WT 210 series UT sensor [4]..... 97

Figure 93. Permasense sensor system a) on pipe section b) detailed view..... 98

Figure 94. Sample thickness measurements for 2 in elbow section from Oct 2016 to Jan 2017. 99

Figure 95. Pipe loop design for aging. .... 100

Figure 96. Pump for sand water media [5]. .... 101

Figure 97. a) Coupon, b) Coupon installed on an elbow. .... 101

Figure 98. In-service component aging loop. .... 107

Figure 99. HIHTL burst pressure profiles..... 108

Figure 100. Ruptured hose section..... 109

Figure 101. O-ring test apparatus..... 110

Figure 102. Gasket test apparatus. .... 111

Figure 103. Tensile strength testing of EPDM and Garlock® coupons. .... 111

Figure 104. EPDM coupon tensile strength..... 111

Figure 105. Garlock® coupon tensile strength..... 112

Figure 106. Coupon tensile strength comparison to baseline data..... 112

Figure 107. Hose sample coupons. .... 113

Figure 108. Aged (bottom) vs. un-aged (top) coupons..... 113

Figure 109. Unaged (baseline) hose sample. .... 114

Figure 110. 6-Month aged hose sample (79°C)..... 114

## LIST OF TABLES

---

Table 1. Sources for Simulation Data, TANK AY-102, 1:8 & 1:21 Scaled Tanks .....	14
Table 2. Parameters Used in Creation of 2D and 3D Computational Domains .....	14
Table 3. Calculation of Suspension Velocity for Particles in a 3” pipe.....	21
Table 4. Candidate Simulants for Use in Initial Phases of the Flushing Tests .....	23
Table 5. Matrix for Flushing Test using 165-ft Test Loop .....	24
Table 6. Information Required from Flushing Test .....	27
Table 7. Amin's Non-Newontian Rheological Characteristics .....	40
Table 8. Potential Sensors for Integration.....	56
Table 9. Temperature (IR Sensor and HSTs) in °F.....	87
Table 10. Experimental Results with ½ in Carbon Steel Plate (Temperature Readings in °F).....	88
Table 11. Experimental Results on Stainless Steel Plate (Temperature Readings in °F) .....	88
Table 12. Sample UT Sensor Measurements for 3-in Straight Section .....	99
Table 13. Sand and Water Testing.....	102
Table 14 . 6-month O-Ring Pressure Test Results.....	109
Table 15. 6-Month Garlock® Gasket Testing Results.....	110

## PROJECT 1 OVERVIEW

---

The Department of Energy's (DOE's) Office of Environmental Management (EM) has a mission to clean up the contaminated soils, groundwater, buildings and wastes generated over the past 60 years by the R&D and production of nuclear weapons. The nation's nuclear weapons complex generated complex radioactive and chemical wastes. This project is focused on tasks to support the safe and effective storage, retrieval and treatment of high-level waste (HLW) from tanks at Hanford and Savannah River sites. The objective of this project is to provide the sites with modeling, pilot-scale studies on simulated wastes, technology assessment and testing, and technology development to support critical issues related to HLW retrieval and processing. Florida International University (FIU) engineers work directly with site engineers to plan, execute and analyze results of applied research and development.

Although a number of tasks have been initiated and completed over the course of the cooperative agreement, at the end of this past year, there were 5 active tasks. These tasks are listed below and this report contains a detailed summary of the work accomplished for FIU's Performance Year 7.

**Task 17.1 – CFD Modeling of HLW Processes in Waste Tanks:** The objective of this task is to provide the sites with mathematical modeling, validation, and testing of computer programs to support critical issues related to HLW retrieval and processing. Specifically, FIU is developing a computational fluid dynamics model based on multiple platforms to simulate mixing and retrieval processes for HLW at Hanford. This has led to two subtasks. One is focused on improving the modeling of non-Newtonian fluids by modifying approaches to characterize the viscosity and the second is related to the validation of the jet impingement correlations for the modeling of pulse jet mixers.

**Task 18.2 – Development of Inspection Tools for DST Primary Tanks:** The objective of this task is to develop inspection tools that will assist engineers in evaluating the structural integrity of the primary and secondary tank floors in the double shell tanks (DSTs) at the Hanford Site. This effort has led to the development of two inspection tools (two subtasks within Task 18.2), both able to provide live visual feedback: a magnetic wheeled miniature motorized rover that can travel through the refractory cooling channels under the primary tank or through the drain lines under the secondary tank, and a pneumatic pipe crawler that can inspect tank ventilation pipes and its central plenum.

**Task 18.3 – Investigation Using Infrared Temperature Sensors to Determine Wall Temperatures of DSTs:** Engineers at Hanford are interested in understanding the temperatures inside the primary tanks to safeguard against exceeding specified limits. In addition, the wall temperature can be used to calibrate temperature dependent ultrasonic transducer systems that are used to determine thicknesses of the tank walls. The objective of this task is to evaluate the ability of infrared sensors to detect tank wall temperatures from the annulus of the DST's via bench-scale testing.

**Task 19.1 – Pipeline Erosion and Corrosion Evaluation:** The objective of this task is to provide the sites with a means to evaluate the structural integrity of waste transfer pipeline components. This has involved the evaluation of potential sensors and the viability of utilizing them to provide real time data for long durations of time. The sensors can be installed and provide thickness measurements of pipeline components and fittings found in jumper pits, evaporators, and valve boxes.

Task 19.2 – Evaluation of Non-metallic Components in the Waste Transfer System: The objective of this task is to provide the Hanford Site with data obtained from experimental testing of the hose-in-hose transfer lines, Teflon® gaskets, EPDM O-rings, and other nonmetallic components used in their tank farm waste transfer system under simultaneous stressor exposures. The experiments will be limited to various combinations of simultaneous stressor exposure to caustic solutions, high temperatures and high pressure. Evaluation of baseline materials will be conducted for comparison to materials that have been conditioned with the various simultaneous stressors.

## TASK 17.1.1

# CFD MODELING OF NON-NEWTONIAN FLUIDS (FIU YEAR 7)

### EXECUTIVE SUMMARY

---

Study of waste processes at Hanford and Savannah River Sites (SRS) require extensive experimental and/or computational investigations with a number of complexities. Processes such as in-tank mixing and retrieval, pipe transfer, and flushing operations deal with numerous parameters that need to be included in tests or simulations. Efforts during this performance period focused on implementation of shear dependency into RANS-HB, review and extension of mixing and retrieval processes in simulation platforms, and review of flushing and critical velocity studies using experimental approaches.

The high level waste (HLW) in Hanford tanks is typically non-Newtonian in nature. Rheology of the waste can be represented by the Herschel-Buckley (HB) model of viscosity. The computational modeling of these processes can combine the HB model with a Reynolds-averaged Navier-Stokes (RANS) platform to create a RANS-HB simulation approach. RANS models, despite their simplicity and cost effectiveness, employ scale averaging of flow features that require improvements. This includes the shear rate for correctly capturing the viscosity variations in the flow and the flow field variables such as velocity and pressure.

This computational fluid dynamics (CFD) effort focused primarily on the transfer of waste in straight pipelines. The goal was to improve the predictions of RANS-HB flow simulation of a non-Newtonian fluid in a straight pipe using a shear dependency modification correlation obtained from a quasi-direct numerical simulation (Q-DNS) platform. Some peripheral work was also done to further validate the last year's RANS-alpha model, and compare the shear dependency between RANS-alpha and Q-DNS-HB simulations.

Investigation of the mixing and retrieval processes required a comprehensive literature review of the processes involved, working and limiting conditions, simulants, and related numerical work. The goal was to simulate the in-tank processes using a simple modeling approach in Star-CCM+ or Comsol multiphysics platforms, which could yield easier-to-interpret data and results as compared to existing work done on the Fluent platform. This investigation resulted in expansion of the initial task discussed to multiphase flow simulations and preliminary results were obtained.

Lastly, efforts focused on development of a test loop that could bridge technical gaps associated with waste transfer lines and flushing of systems at Hanford and Savannah River. The objective was to investigate parameters that affect flushing and develop a test plan and an experimental setup for optimizing flushing operations. A test plan is currently being developed and is under review.

## NON-NEWTONIAN CFD MODELING

---

### Introduction

Accurate simulation of flow systems involving non-Newtonian fluids such as waste processing systems in the US Department of Energy's sites has attained a great deal of attention. Computational fluid dynamics (CFD) can play a significant role in assisting engineers to safely and optimally transfer the waste from single shell tanks to double shell tanks, according to Meyer et al. (2005). CFD simulations can be validated by experiments and run with different types of simulants that can be used for further predictions. A 1.5 wt% Laponite-water simulant was used in experimental and simulation studies by Escudier et al. (1996 & 2005) and Peltier et al. (2015), respectively. Variation of shear stress in this simulant can be modeled using HB rheological model developed by Herschel and Bulkley (1926).

Previous efforts by this author, Baharanchi et al. (2016), created a method to obtain and utilize alternative viscosity values during RANS simulations for pipe flow of 1.5 wt% Laponite-water simulant. This method, known as the alpha-method, demonstrated successful improvement of the velocity profiles for laminar, transitional, and turbulent regimes of flow. Results compared the performance of different versions of the alpha viscosity model against those of the original HB and shear rate correction of Gavrilov and Rudyak (2014) in regards to mean axial velocity profile as well as viscosity profiles in limited cases.

In this research, simulation results from the RANS-alpha method were considered for study of three primary goals: (1) validation of turbulence quantities obtained by RANS-alpha simulations, (2) analysis of the shear dependency behavior, and (3) implementation of the shear dependencies of Q-DNS-HB into RANS-HB. For the first goal, profile of normalized velocity ( $u^+$ ) versus non-dimensional wall distance ( $y^+$ ) were created for the turbulent and transitional cases and compared with the same quantities reported by Escudier et al. (1996). This work aims to evaluate the validation of results when turbulent quantities were considered in addition to time and scale averaged velocity profiles.

For the second goal, additional simulations using the RANS-alpha method were ran for Reynold numbers of 10k, 15k, and 20k as an extension of FIU's previous investigations, but with a shift in focus towards shear dependency analysis using two criteria developed at FIU. The RANS simulations were based on the  $k$ - $\epsilon$  turbulence model and a modified HB-based viscosity model (alpha model). Later, shear dependency analysis of the most recent results obtained from a quasi-direct numerical simulation (Q-DNS) was considered. Results of this analysis were used to obtain relationships between the shear rate and turbulence variables in dissipative scales of turbulence referred to as baseline shear dependency in this work.

For the third goal, the baseline shear dependency obtained from Q-DNS simulations were incorporated into a RANS-HB simulation with the same Reynold number of 25.3K. This incorporation was done according to an algorithm that was developed inside the Q-DNS simulation. FIU compared shear rate variations between Q-DNS-HB and RANS-alpha simulations to evaluate similarities. The results suggested a significant improvement of RANS H-B modeling using the modified shear rate.

## NUMERICAL APPROACH

As noted previously, the RANS model used for this investigation is a k-ε turbulence model and the viscosity was modeled using the alpha model which is a HB-based viscosity model. Different versions of this model were used in the simulation of flow with different levels of mesh resolution to ensure that the results guarantee grid independence. Details of the equations solved, viscosity models, and turbulence modeling could be found in FIU’s year-end report for FY 2015 and Baharanchi et al. (2016). Here, the parameters of the turbulence velocity profile are defined as  $u^+ = u/u^*$  and  $y^+ = yu^*D/\mu_w$ , where  $u^*$  is the friction velocity defined as  $u^* = \sqrt{\tau_w/\rho}$ , where  $\tau_w$  is the shear stress at the wall and  $\rho$  is the fluid density. Other variables,  $y$ ,  $D$ , and  $\mu_w$  are wall distance, pipe diameter, and viscosity of the fluid at the wall.

Shear rate plays a critical role in simulation studies of non-Newtonian fluids. Analysis from Gavrilov and Rudyak (2014) showed that there is a strong dependency between shear rate and dissipation rate of turbulent kinetic energy. In this work, variation of the shear rate against a quantity defined by Eq.(1) was obtained for dissipative scales.

$$\frac{u_{rms}}{\eta} = \frac{\sqrt{\frac{2K}{3}}}{\frac{\nu^{3/4}}{\varepsilon^{1/4}}} \quad (1)$$

$u_{rms}$  and  $\eta$  represent velocity and length scale of turbulent structures. In this equation  $K$ ,  $\nu$ , and  $\varepsilon$ , represent TKE, kinematic viscosity, and TDR, respectively. This quantity has the same units of shear rate,  $sec^{-1}$ , and is zero for non-dissipative scales. In the case where the average value of  $\varepsilon$  is obtained from spatial analysis,  $\eta$  will then represent Kolmogorov length scale, which is the smallest scale in turbulent flow. In RANS,  $K$  and  $\varepsilon$  are obtained from the solution to the closure equations of TKE and TDR and are directly accessible from STAR-CCM+. In Q-DNS, TKE and TDR must be obtained from fluctuations of velocity components. TKE is defined as  $TKE = 0.5*(\dot{u}_x^2 + \dot{u}_y^2 + \dot{u}_z^2)$ , where prime denotes fluctuations and  $u$  is the axial velocity component. Definition of  $u_{rms}$  and TDR are according to Eq.(2) and Eq.(4), respectively.

$$u_{rms} = \sqrt{\frac{1}{3}(u_{x,rms}^2 + u_{y,rms}^2 + u_{z,rms}^2)} \quad (2)$$

$$u_{x,rms} = \sqrt{\dot{u}_x^2}, \quad u_{y,rms} = \sqrt{\dot{u}_y^2}, \quad u_{z,rms} = \sqrt{\dot{u}_z^2} \quad (3)$$

$$\varepsilon = \mu \left( 2 \frac{\overline{\delta u_x^2}}{\delta x} + 2 \frac{\overline{\delta u_y^2}}{\delta y} + 2 \frac{\overline{\delta u_z^2}}{\delta z} + \left( \frac{\overline{\delta u_x}}{\delta y} + \frac{\overline{\delta u_y}}{\delta x} \right)^2 + \left( \frac{\overline{\delta u_x}}{\delta z} + \frac{\overline{\delta u_z}}{\delta x} \right)^2 + \left( \frac{\overline{\delta u_y}}{\delta z} + \frac{\overline{\delta u_z}}{\delta y} \right)^2 \right) \quad (4)$$

Another variable that was introduced for the study of shear dependency behavior was TDR/TKE. This ratio has units of  $s^{-1}$  similar to the shear rate and was obtained from the equations described above. Variation of this variable in the domain formed the second criterion for the shear dependency study and was used in conjunction with the first criterion to complete the analysis.

For brevity, study parameters for RANS-alpha, RANS-HB, and QDNS-HB simulation are not included in this report. They are available in FIU’s FY 2015 report.

### RESULTS & DISCUSSION

Results for the turbulence velocity profiles were obtained for all the models used in FY 2015. Figure 1 and Figure 2 show the results for transitional,  $Re = 3400$  and fully turbulent,  $Re = 25300$ , respectively. These results indicated that best agreements between simulation results and experimental data were obtained with the Inv.\_Local\_alpha method and Inv.global\_alpha model versions for  $Re = 3400$ , and  $Re = 25300$  cases, respectively.

Interestingly, Inv.global\_alpha model was also rated the best model version for the fully turbulent case ( $Re = 25300$ ) in FY 2015 when FIU considered the mean velocity profile instead of the turbulent velocity profile. Therefore, this model version could best represent both mean and turbulent velocity profiles for the fully turbulent case.

In the case of transitional flow, ratings here were different from the ratings obtained in FY 2015. Perhaps the alternation between laminar and turbulent regimes in a transitional flow posed a challenge to a fully turbulent RANS model like the  $k-\epsilon$  model that was used in this work. Therefore, no consensus could be achieved regarding the alpha model for the transitional case.

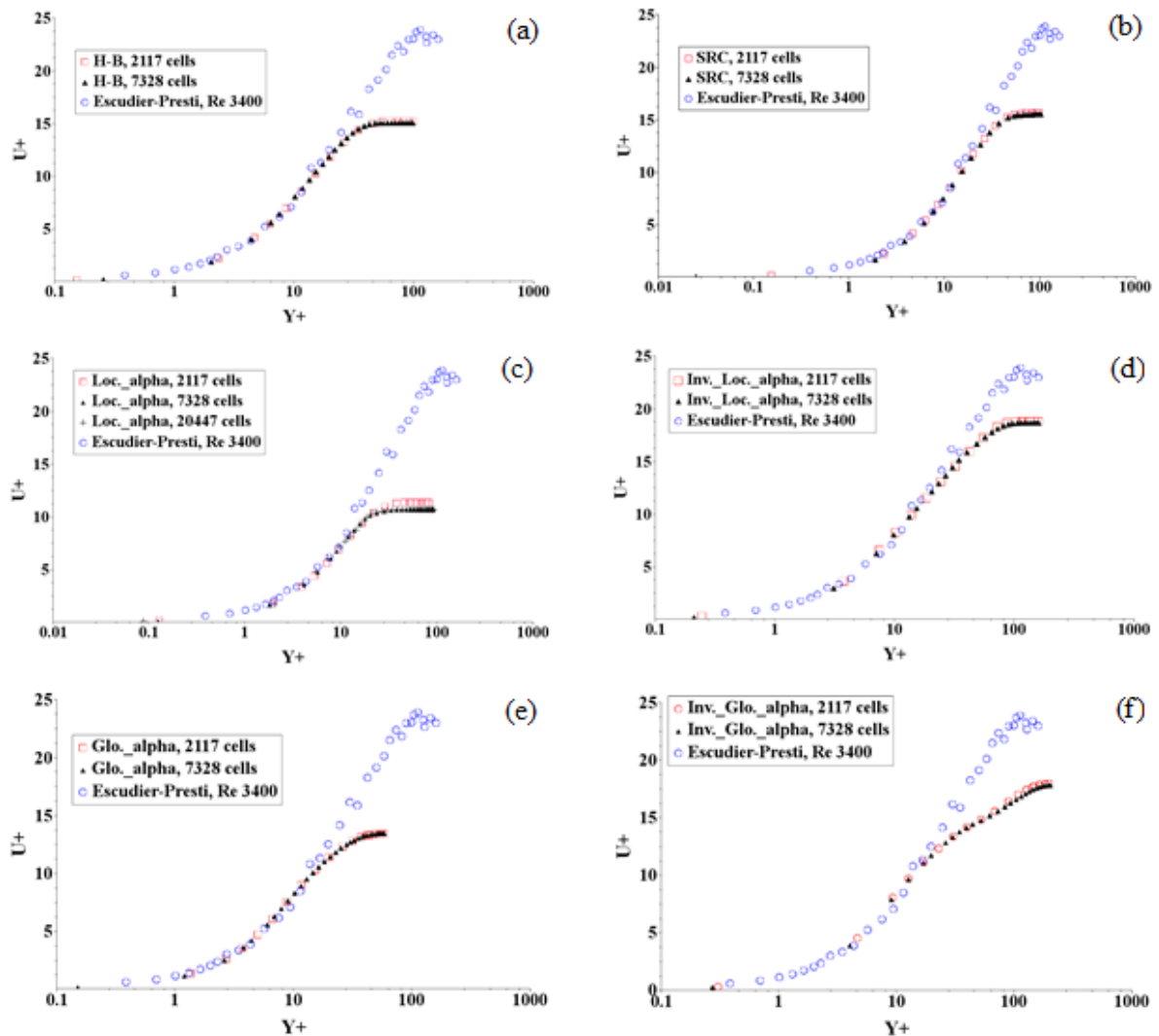


Figure 1. Turbulent velocity profile for the transitional case.

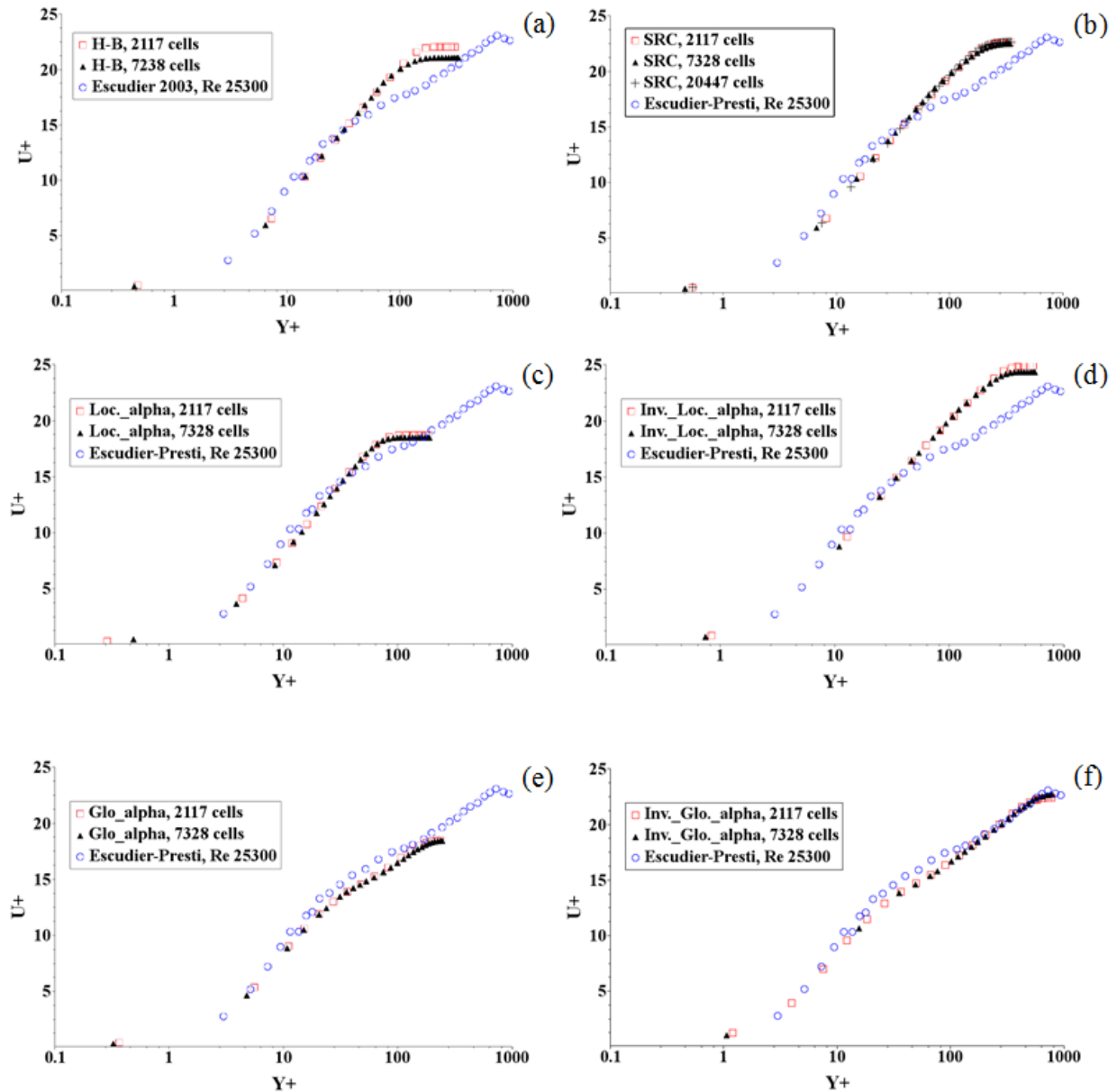


Figure 2. Turbulent velocity profile for the fully turbulent case.

FIU extended the same analysis of shear rate which was performed last year for both RANS-HB and Q-DNS-HB results. In RANS-alpha simulations, various Reynolds numbers,  $Re = 10000, 15000, \text{ and } 20000$ , were considered to observe similarities between profiles of shear dependencies. In Q-DNS-HB simulations, it was shown that mean and turbulent profiles could be successfully captured first.

Results as shown in Figure 3 demonstrated similar profiles that were non-linear and increase and shift to the right with increasing Reynolds number. This is a result of higher shear and velocity fluctuations in higher Reynolds numbers. Additional and similar analysis was performed using the ratio of turbulent dissipations to turbulent kinetic energy, which has the same units as shear rate (1/sec). For each Reynolds number shown in Figure 3, a profile with small slope is preceded with a profile having a larger slope. The former is indicative of variations in the vicinity to solid

boundaries and the slope of this profile grows with increasing Reynolds number. In contrast, variations with almost equal slopes were observed at small values of TDR/TKE for different Reynolds numbers. Similarity between these profiles suggest that a correlation can be obtained and implemented into the RANS-HB modeling to directly modify the shear rate based on TDR/TKE values.

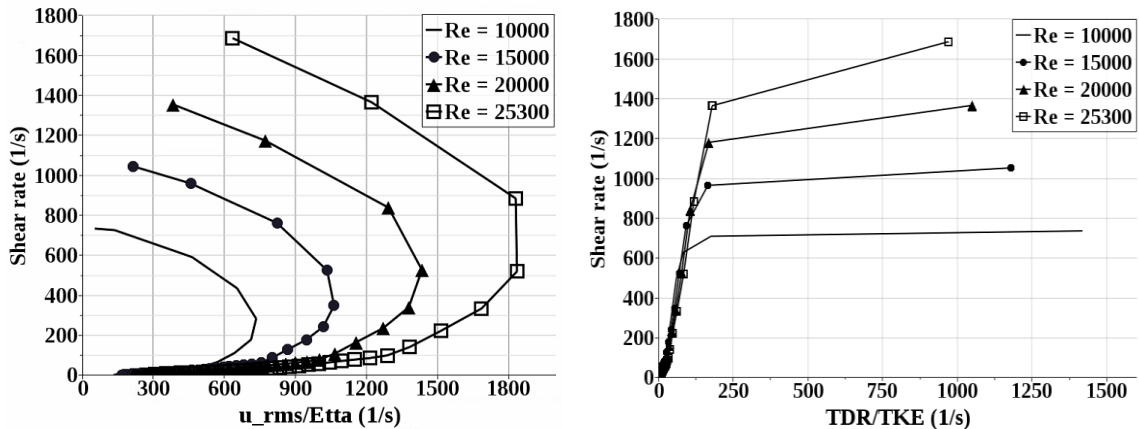


Figure 3. Variation of shear rate versus different ratios.

Figure 4 shows profiles of mean and turbulent velocities for the axial velocity component obtained from the Q-DNS. Experimental profiles of mean and turbulent velocity were obtained from Escudier et al. (1996 & 2005) and Escudier and Presti (2003), respectively. As observed, good agreement existed between the simulation and experimental results, which allowed further investigation on shear rate dependency parameters.

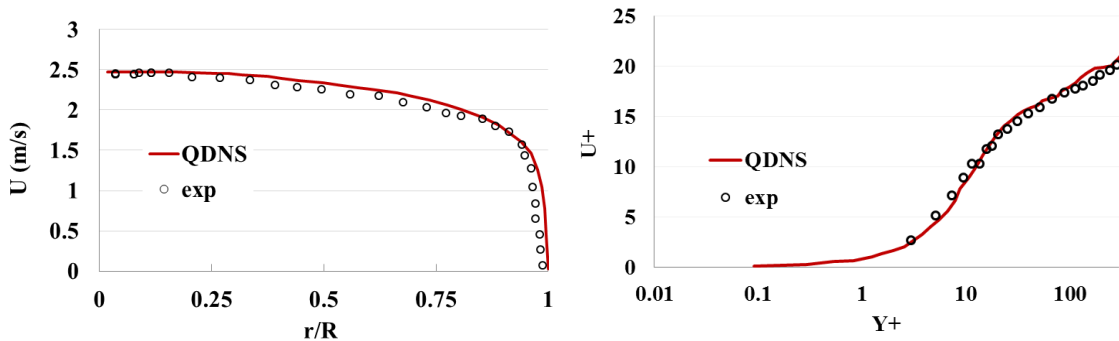


Figure 4. Contour and profile of mean and turbulent axial velocity profiles, Re = 25300.

For study of shear dependency in the Q-DNS-HB modeling investigation, efforts focused on the fully turbulent flow case. Variation of shear rate versus  $u_{rms}/\eta$  and TDR/TKE were obtained and plotted for turbulent structures, as shown in Figure 5(a,b). Figure 5(a) shows that a qualitative similarity existed between Q-DNS-HB and RANS-alpha simulations. In addition, a qualitative similarity was found between the variation of shear rate in Figure 3 and the bottom envelope in Figure 5 (b). However, the RANS-alpha method imposed a significant underestimation of shear rate and  $u_{rms}/\eta$ .

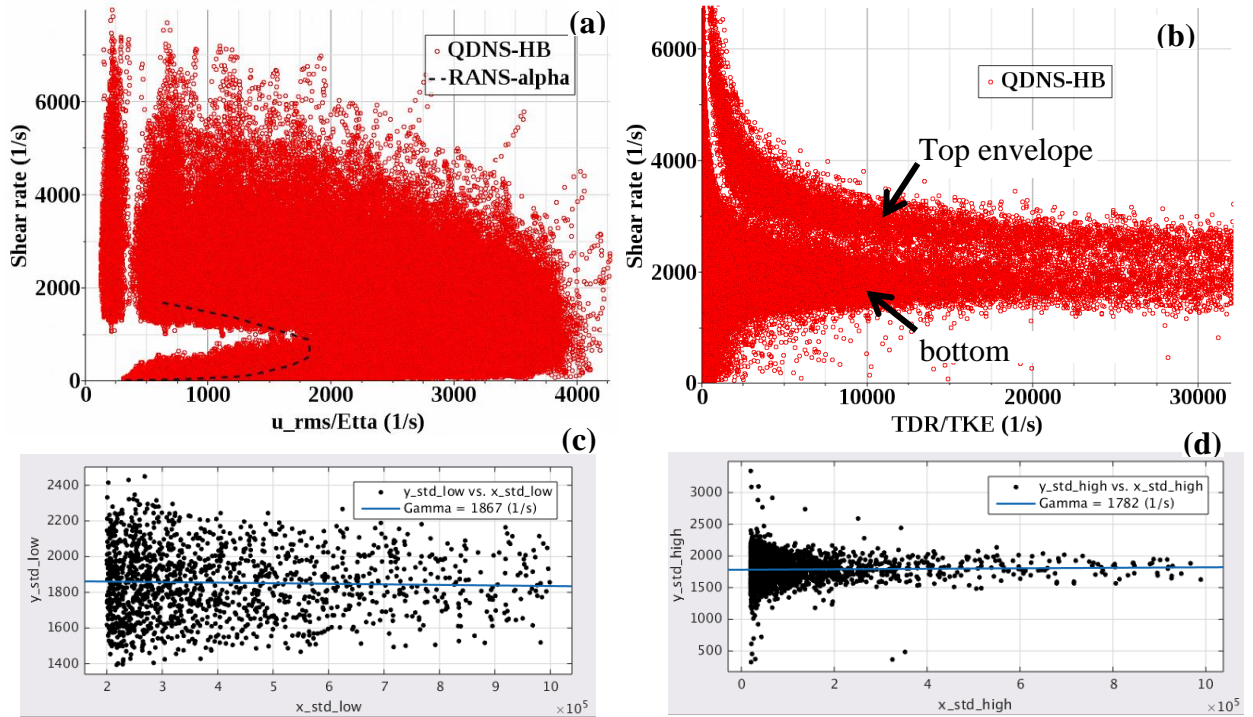


Figure 5. Shear dependency on  $u_{rms}/\eta$  and TDR/TKE,  $Re = 25300$ .

Variation of shear rate versus TDR/TKE, as shown in Figure 5 (b), revealed two envelopes which were partly similar. The top envelope was found to contain computational cells on solid boundaries and in structures that exist in the core flow, as shown in Lijia Xu et al. [24]. It was found that the top envelope was related to regions of small  $u_{rms}/\eta$  which can be separated from the bottom envelope by  $u_{rms}/\eta < 400 \text{ s}^{-1}$ . Results of this structure separation in the flow field is shown in Lijia Xu et al. [24]. This figure also shows a fine resolution display of these structures obtained through adjusting the threshold of Q-criterion on the course resolution.

Another observation from Figure 5 (b) is that both top and bottom envelopes show reductions of shear rate with an increase of TDR/TKE. Here, more attention is given to higher values of the dissipation rate. A regression analysis was performed in Matlab, as shown in Figure 5(c-d), and values of 1867(1/s) and 1782 (1/s), were obtained for the top and bottom envelopes, respectively.

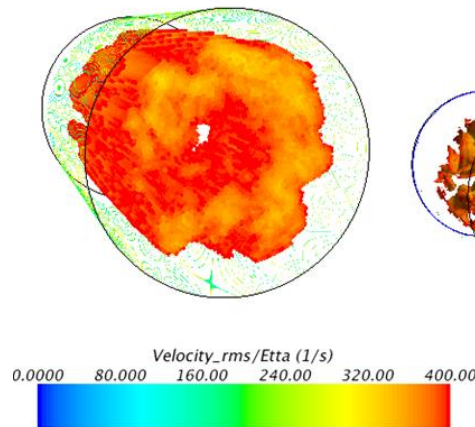


Figure 6. Structures found in core flow which belong to the top envelope in Figure 5(b).

An algorithm for shear rate assignment was developed based on the results presented above. In this algorithm, the distinction between converged values is based on values of  $u_{rms}/\eta$  for each cell in the RANS-HB simulations. Equation 4 shows the model that was used for alteration of shear rate in the RANS-HB simulation:

$$\gamma = \begin{cases} 1867 \text{ (1/s)} & \frac{u_{rms}}{\eta} \leq (\frac{u_{rms}}{\eta})_{THS} \ \& \ \epsilon_{HB} > \epsilon_{THS} \\ 1782 \text{ (1/s)} & \frac{u_{rms}}{\eta} > (\frac{u_{rms}}{\eta})_{THS} \ \& \ \epsilon_{HB} > \epsilon_{THS} \\ \gamma_{HB} & \epsilon_{HB} \leq \epsilon_{THS} \end{cases} \quad \text{(Eq. 5)}$$

In this model,  $\gamma_{HB}$  denotes an unaltered shear rate which is obtained directly from the velocity field, and parameters  $\epsilon_{THS}$  and  $(u_{rms}/\eta)_{THS}$  are defined as thresholds for the dissipation rate and  $u_{rms}/\eta$ , respectively. FIU set the  $\epsilon_{THS}$  to an extremely small number to include the smallest dissipation rates in the modifications. The value of  $(u_{rms}/\eta)_{THS}$  was set to  $400 \text{ s}^{-1}$ , as was found previously.

Application of the proposed shear modification model was tested in a RANS-HB simulation of flow with  $Re = 25300$ . Results of this implementation, referred to as RANS-HB(modified) in Figure 7, closely matched the profile of the RANS-alpha method and was less than 2 percent different than the Q-DNS-HB profile. This result indicated successful implementation of the proposed shear rate algorithm. More work will be needed to mathematically define the  $(u_{rms}/\eta)_{THS}$  and converged values of shear rate at high TDR/TKE values and relate these quantities to flow conditions. In addition, this algorithm can be tested for different flow Reynolds numbers of the same simulant as well as other simulants.

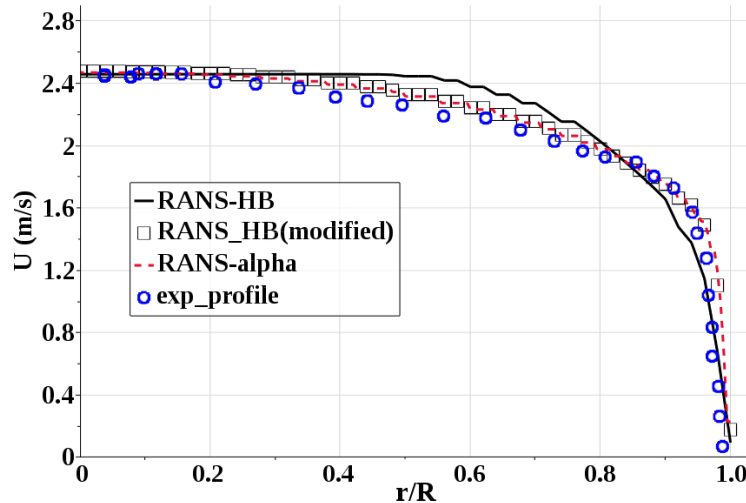


Figure 7. Axial velocity for modified RANS-HB and other RANS simulations.

## MODELING OF RETRIEVAL PROCESSES

---

### INTRODUCTION

Selection of baseline experimental and simulation data is a critical step in conducting numerical simulations of waste mixing and transfer. An extensive literature review was conducted in order to obtain the correct properties and dimensions that can be used in construction of the computational domains, meshes, and simulations.

According to Rector et al. (2010), solids in the tanks at Hanford are generally composed of submicron particles of Boehmite and Gibbsite. The presence of these components can introduce particle gels with non-Newtonian behaviors; more specifically, a Bingham plastic type of fluid may exist (Lee 2012). By referring to observations of Powell et al. (1995), Wells et al. (2013) explains that slurry rheology may change from Newtonian to non-Newtonian and can cause a significant reduction of mobilization of the clay layer. The effect can be a 40% increase of required flow rate to achieve the same waste mobilization metric, as usually identified by the effective cleaning radius (ECR). According to Adamson and Gauglitz (2011), suspending particles of a non-Newtonian slurry with higher yield stress is more difficult, but once erosion happens, particles stay suspended to a greater degree, as compared to situations with slurries with a lower yield stress. The combined effect will be higher concentrations in the transfer lines.

It is critical to know how the yield stress varies with the concentration of solids in the slurry. According to Lee (2012), a simulant composed of 22 wt% and 28 wt% Kaolin clay in water will have a yield stress of 3 Pa and 10 Pa, respectively. These stress values are recommended by RPP-PLAN-51625 for the simulant representing the slurry in Hanford tanks. In particular, this yield stress of the sediment layer at the bottom of the tank may be significantly different from the liquid above the solid sediment, the supernatant, which has suspended particles in it. This information is critical for the simulation since, if the mixture multiphase model is used, then different rheograms are needed for the solid layer and the supernatant. Therefore, a portion of the literature review was dedicated to finding this variation.

In this research effort, attention was given to the properties of different simulants used in full-scale or scaled experiments and simulations related to processes at or between Hanford tanks. Focus was on reported data of tests conducted in 2011 and 2013, as well as related simulations. FIU reviewed the procedure and results of some scaled tests conducted by Lee and Thien (2013) and Wells et al. (2013) using a four-component simulant (gibbsite, sand, zirconium oxide, stainless steel, as well as Wells et al. (2011) using a five-component simulant (gibbsite, silicon carbide, zirconium oxide, stainless steel, bismuth oxide). Details and reports regarding simulant development and refinement processes are provided by Wells et al. (2011) and Lee (2012a, 2012b).

For simulations in Star-CCM+, data and geometrical dimensions pertaining to the 2013 tests with the four-component simulation were considered. Rationale for this selection is for simplicity and the amount of accessible information.

According to Peurrung et al. (2013), the modeling and scaled testing of the waste handling processes is a necessity since full-scale vessel testing may be too costly and time consuming. For this reason, design and optimization of several processes in waste mixing and transport are based on results from pilot-scale experiments, which are difficult to extrapolate to full-scale behavior, according to Rector et al. (2010). Thus, both scaled and full-scale CFD simulations are needed.

These researchers used high-performance multiphase flow simulations to resolve design, operational safety, and optimization issues for high-level waste transport processes.

The current approach in simulating these systems is to use one of the commercial CFD programs with a multi-fluid option to model the different phases. The primary drawback with this approach is that some programs are limited in their parallel scaling. As an example, use of Fluent for design verification was rejected due to substantial difficulty in result validation, according to Peurrung et al. (2013). However, FIU's review indicates that Star-CCM+ has appropriate parallel computing performance and ease of implementation of user defined functions which suggests a level of suitability for this CFD application.

Numerical simulation of mixing of solid-liquid slurries using high-speed fluid jets is a technical challenge because of the large separation of spatial and time scales (Rector et al., 2010). Peak jet velocity at the nozzle is on the order of 10 meters per second, which results in a Courant limit time step on the order of thousandths of a second. Therefore, a complete cycle of rotation of the high-speed jets in a tank takes approximately 1 minute and the simulation needs a large number of time steps. For example, a typical pulse-jet simulation takes weeks or even months to complete on a mid-size computer cluster for a single proposed operational configuration, according to Rector et al. (2010). In addition, CFD simulation must consider the strong interactions between fluid flow, solid transport, and erosion/suspension from/to the sediment layer, as shown in Figure 8. Peurrung et al. (2013) concluded that jet mixing simulations of a scaled tank experiment can take only 5 hours using 5000 processor cores while it may take 336 hours (two weeks) if run on a cluster with 64 processor cores. Therefore, an essential step in conducting simulation of the mixing system is obtaining an estimate of the minimum number of processors needed to simulate mixing and transport processes as quickly and accurately as possible.

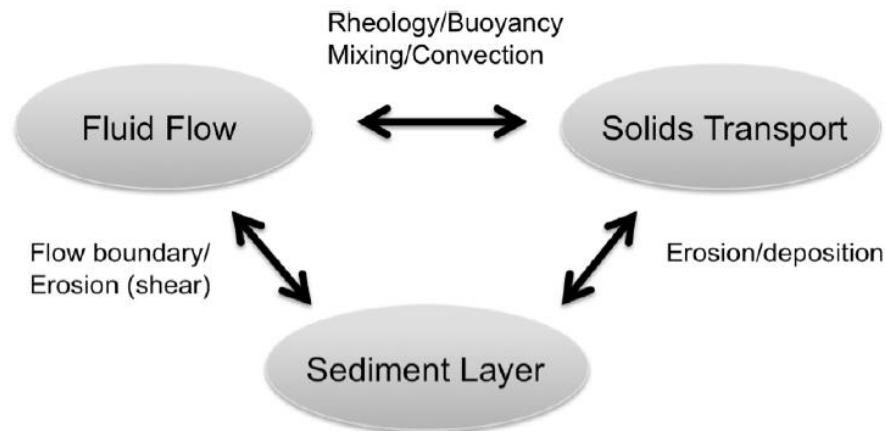


**Figure 8. Interactions of liquid, suspended solids and settled solid fields during tank mixing operations, image and description from Rector et al., (2010).**

### *Literature Review*

General approaches in the literature regarding the simulation of the mobilization of sediment first requires the erosion of the sediment surface and then focuses on the suspension of the sediment. Efforts were focused on literature and simulations for the initial erosion of the solid phase. These simulations were conducted to better understand the fundamental problems and limitations that exist with current simulation methods.

The literature contains a number of numerical studies on sediment erosion using an Eulerian-Eulerian approach, which is also referred to as the two-fluid model approach. In this approach, both solid and fluid phases are treated as a continuum and equation sets are solved separately for each individual phase that is present in the flow. Some of the research using this method has been conducted by Parsi et al. (2015), Rector et al. (2010), He et al. (2009), and Gustavasson and Almstedt (2000). An alternative approach is the Euler-Lagrange method where the solid is treated as a discrete phase (particles) and has been used by Mercier et al. (2014) and Kim et al. (2015). In this work, the first approach is considered and the following paragraphs explain the details of the procedure.

Several process vessels will hold waste at various stages within the Hanford Waste Treatment and Immobilization Plant (WTP). These vessels have mixing system requirements to limit hydrogen gas accumulation and ensure that pump transfer and normal operations occur (Rector et al., 2012). The WTP Pretreatment Facility requires a uniform feed from each waste tank that consistently matches tank average concentrations during the extraction process. This acceptance criterion requires an accurate method for determining the tank average concentration through a limited number of samples during mixing. CFD modeling can be used to provide a meaningful prediction of suspended solids behavior to guide both sampling (in terms of sampling location) and extraction processes. For this application, a reliable CFD code with formal verification and validation is needed (SRNL-PNNL, 2013).

In addition, another key uncertainty in the waste feed delivery system is a potential variation in undissolved solids (UDS) transferred in individual batches in comparison to an initial sample used for evaluating the acceptance criteria (Wells et al., 2011). Variation in UDS can lead to pipeline plugging, which has been identified as a significant issue for the WTP, according to Rector et al. (2009). This uncertainty is due to a challenging and perhaps one of the more limiting WTP waste acceptance criteria parameters, which is the critical velocity of the slurry. Critical velocity is defined as the velocity of the slurry above which particulates will remain mobilized in the carrier solution and be transported down the pipe. Critical velocity is important for WTP receipt to ensure that solids in HLW feed will remain suspended and not accumulate in plant piping. The CFD modeling work of Rector et al. (2009) shows capabilities of obtaining detailed distributions for settled and suspended solids.

Wells et al. (2011) introduced metrics for waste operations. Operations are particle settling, mobilization, suspension, and pipeline transfer. The metrics include particle settling velocity ( $U_t$ ), critical shear stress for erosion of particles ( $\tau_c$ ), cloud height ( $H_c$ ), effective cleaning radius (ECR), and pipeline critical transport velocity ( $U_c$ ). Among these, the transfer concentration is the primary metric used for DST sampling and batch transfer performance, according to Lee (2012) and Wells et al. (2013). Equations that describe models for each metric, including Archimedes number, jet-suspended impeller speed, and jet velocity, that are needed to achieve a certain degree of solid suspension for each metric, can be found in reports of Wells et al. (2011) and Rector et al. (2009).

## NUMERICAL APPROACH

Representation of the sediment layer at the bottom of double-shell tanks at the start of simulation (initial condition) required a known shape of the sediment layer. First, a very simple laminar flow simulation was considered to quickly test the capability of Stat-CCM+ in capturing flow features including the presence and mobilization of a simulant layer. An arbitrary region was created with an initial solid volume fraction equal to the maximum packing ratio ( $\epsilon_{\text{solid}} = \text{max\_packing ratio}$ )

0.624, for spherical particles) inside another larger arbitrary region, as shown in Figure 9. An interface on each side of the smaller domain was created to ensure continuity between the domains.

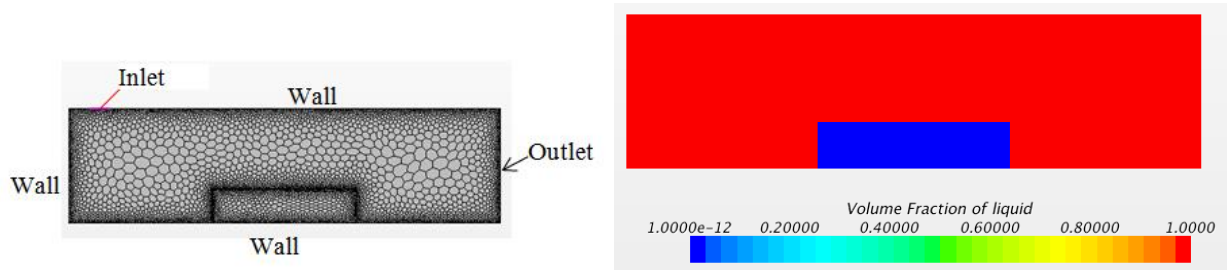


**Figure 9. Mesh and initialization of a multiple region domain created in Star-CCM+.**

Later, 2D and 3D models of a 1:21 scaled tank (internal diameter of 43 inch) were created with inclusion of all air lift circulators (ALCs), mixer jet pumps, a transfer line, and a sediment layer. In creation of these domains (Figure 10 and Figure 11) information in Table 1 and Table 2 were used.

**Table 1. Sources for Simulation Data, TANK AY-102, 1:8 & 1:21 Scaled Tanks**

Tank internal diameter	Lee and Thien (2013), lee (2012) and Jensen et al. (2012)
Mixer jet pump	Lee and Thien (2013), lee (2012) and Jensen et al. (2012)
Transfer pump suction line	Lee and Thien (2013), lee (2012) and Jensen et al. (2012)
Air lift circulators (ALC), numbers	Thien (2012), Lee (2012)
Transfer lines	Lee and Thien (2013), Lee (2012)
Shape of the tank bottom	Lee (2012).
Thickness of sediment layer	Jensen et al. (2012), Thien et al. (2011) , Greer and Thien (2012)
Thickness liquid layer	Jensen et al. (2012), Greer and Thien (2012)
Solid concentration	Lee and Thien (2013), Wells et al. (2013)
Data collection times	Jenson et al. (2013), Well et al. (2013)
Flow rate data	Wells et al. (2013)

**Table 2. Parameters Used in Creation of 2D and 3D Computational Domains**

Property	43” Tank
Tank internal diameter (m)	1.1
Mixer jet pump nozzle diameter (m)	0.0071
Mixer jet pump nozzle elevation (m)	0.0218
Mixer jet pump suction diameter (m)	0.0135
Mixer jet pump suction elevation (m)	0.0061
Mixer jet pump axial offset in 0° & 180° angles(m)	0.3230
Transfer pump suction diameter (m)	0.28

Transfer pump suction velocity (m/s)	1.16 – 3.44
Transfer pump suction elevation (m)	0.0071
Transfer pump axial offset in 90° angles (m)	0.0884
Transfer pump suction inlet diameter (m)	0.0064- 0.0122* 0.0071**
Transfer line diameter (m)	0.0095* 0.0079**
Air lift circulators (ALC), Count	22
Air lift circulators (ALC), Diameter (m)	0.036
Air lift circulators (ALC), Elevation (m)	0.035
Sediment layer thickness (m)	0.067
Liquid layer thickness (m)	0.43
* lee (2012) for SSMD of AY-102 tank.	
** Jensen et al. (2012) for SSMD of AY-102 tank.	

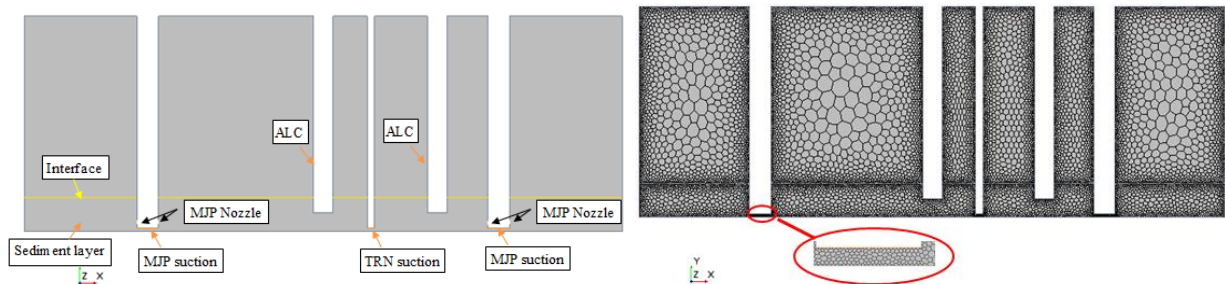


Figure 10. 2D computational domain created for the 1:21 scaled tank with 43” internal diameter.

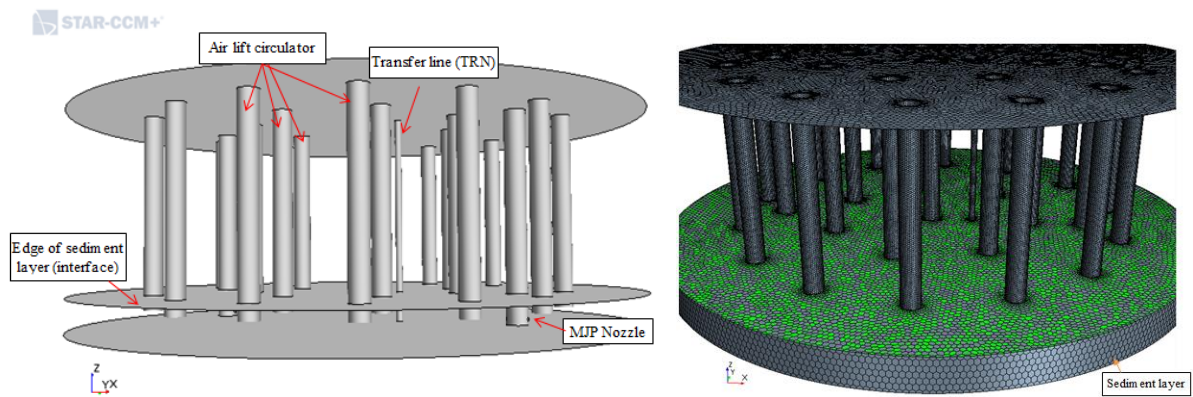


Figure 11. 3D computational domain created for the 1:21 scaled tank with 43” internal diameter.

During this performance period, a limited number of 2D simulations were run for flow in the scaled 43-inch tank. The purpose of these simulations was to evaluate the correct setup of interface between the sediment layer and the rest of the tank and evaluating the effect of suction and nozzle ports. Simulation were run in steady and single-phase modes with fixed jets and standard k-ε model. Nozzle and suction ports of the mixture jet pumps (MJP) were not connected using a field function for mass flow rate. Instead, a constant value was assigned for the target mass flow rate

that represents a steady situation for this step of the work. In reality, a slurry pump connects these ports.

**RESULTS & DISCUSSION**

Results (Figure 12) of the simulation using an initial constant viscosity for the solid phase in indicated diffusion of the solid which smeared the interface between solid and fluid. This result did not show erosion and suspension of the solid which is directly associated with the viscosity inside and on top of the sediment.

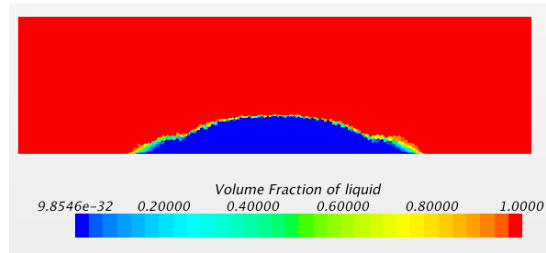


**Figure 12. Multiphase simulation of jet flow in a multi-region domain.**

According to Marcier et al. (2012-2014), Bonelli et al. (2012), and Rector et al. (2010), erosion occurs if the shear stress on the sediment is greater than its yield stress. Initially, values of the shear stress were obtained and it was observed that maximum shear stress was approximately 0.064 Pa in the areas close to the jet inlet and lower values were observed on the top of the sediment layer. These shear stress values were lower than the yield stress values found in Bonelli et al. (2006), Marcier et al. (2012-2014), and Bamberger et al. (2010). Therefore, implementation of the erosion law was pointless, since no erosion would occur at this stress level. As an alternative, an artificial viscosity was assigned to regions where the solid volume fraction was equal or larger than 0.624. This artificial viscosity was set to a large value (ten times larger than the viscosity of the liquid) to reflect higher resistance to flow inside the smaller domain. Initial conditions are shown in Figure 13.

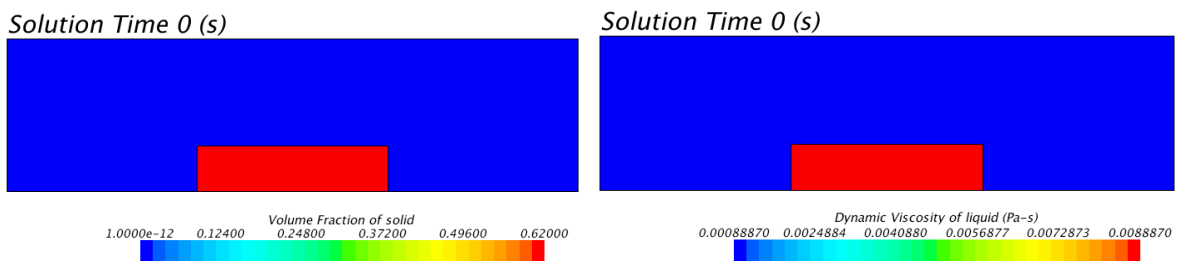


**Figure 13. Initial conditions for simulation of jet flow in a multi-region domain.**

Simulations with the above parameters were run and continued for 60 seconds. Results, as shown in Figure 14, indicated deformation of the sediment layer and suspension of solids in the supernatant. Results show that there was still residue left in the domain after 60 seconds, which was an unrealistic situation caused by the artificial viscosity assigned to the solid region. Continuity of flow across the interfaces and flow inside the smaller regions are shown after the solid is pushed from the domain.

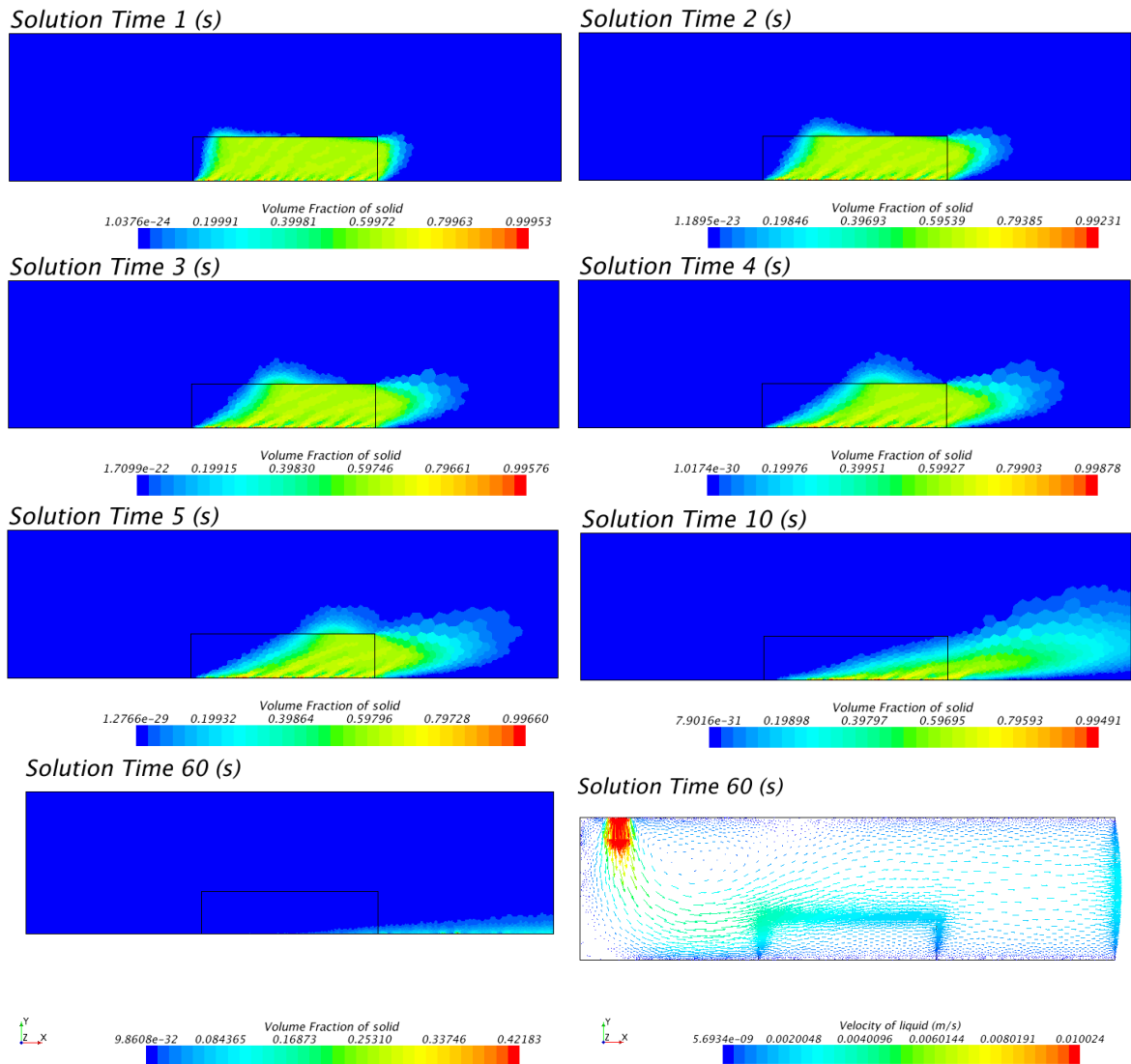


**Figure 14. Evolution of flow from 0 sec to 60 sec, contour of solid volume fraction.**

2D simulations of flow in the scaled 43-inch tank with open MJP suction ports encountered difficulty in convergence and fluctuation of results were observed. The contour of the velocity magnitude, as is shown in Figure 15, indicated the presence of large vortices in the entire domain as a result of the jet penetration effects. The reported values for the mass flow rate were 0.163 and 0.49 kg/s in suction ports of the transfer line and MJP, respectively, which were slightly different from the target values. However, the results did not show long straight penetrations of the jets as expected and the jets were immediately attached to the tank bottom at a very short distance from the nozzles, according to the vectors of velocity shown in this figure. In addition, the results show a strong radial velocity just under the MJPs (shows as red vectors) where strong upward motion was expected to occur due to suction effects. By looking at any of the MJPs, it was observed that this large velocity was created as a result of backward flow of one of jets and realignment with another jet, which were supposed to be oppositely moving in radial directions. The reason for this backward flow behavior is unknown at this time. Three velocity profiles were also plotted at these suction ports for qualitative and quantitative assessments.

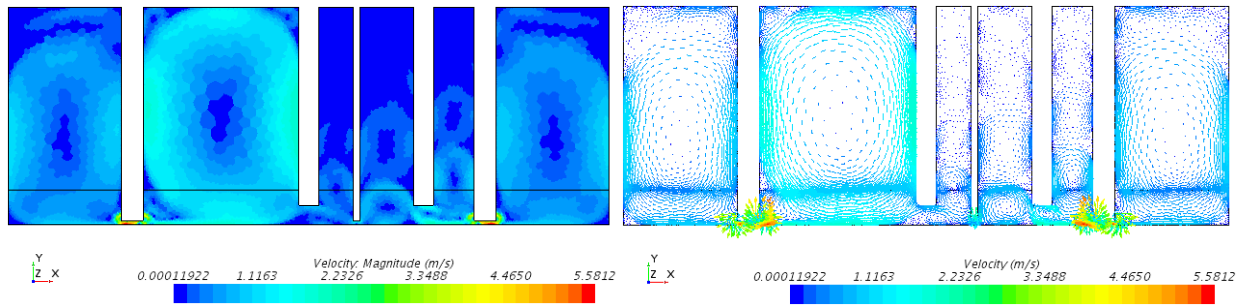


**Figure 15. Velocity contour and vector filed in 2D simulation of 43” tank with MJP suction ports.**

Later, the effect of treating the suction ports of MJPs as being closed (wall B.C.) was studied. The purpose of this study was to see if strong asymmetry was caused by the presence of the MJP’s suction ports. This simulation, with MJP suction ports set to the wall B.C., converged to results that did not fluctuate. As shown in Figure 16, only a dominant large vortice existed in the domain which was located between the left MJP and the central ALC. A display of velocity vectors in Figure 16 showed penetration of two opposing jets in the domain; however, an immediate backflow of one of the two jets was observed. This result indicated no high-velocity region under the suction ports of MJPs and transfer lines.

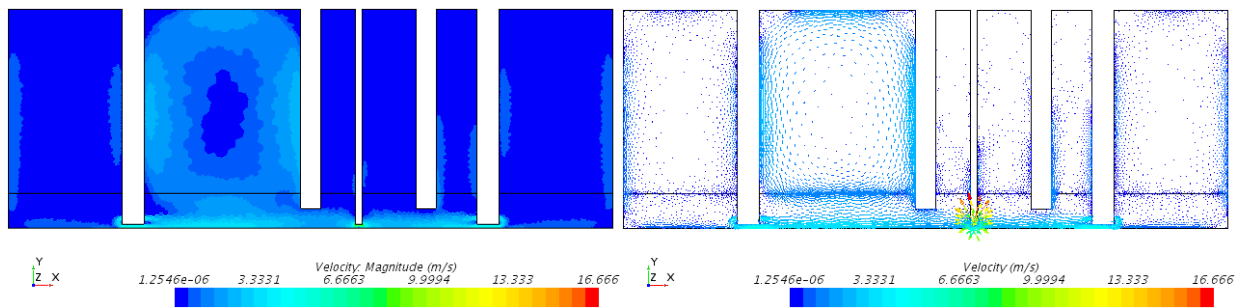


**Figure 16. Velocity contour and vector filed in 2D simulation of 43” tank without MJP suction ports.**

Another observation was obtained by comparing the velocity profiles at the location of suction ports between the two simulations explained above. The left diagram in Figure 17 does not show a symmetrical profile at any of the ports in the first simulation. The calculated face-average velocity value at the transfer line was 1.78 m/s, which was slightly different from the target value of 2.2 m/s. This discrepancy could be caused by the rectangular configuration of the ports, pipes, and the tanks two-dimensional domain as opposed to the actual circular configurations. The right diagram in this figure indicated symmetrical velocity profiles at the suction port of the transfer line.

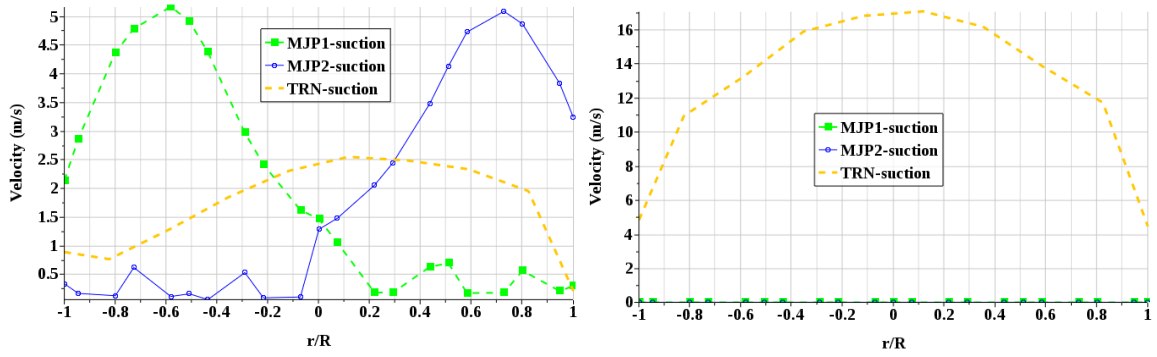


Figure 17. Velocity profile at the location of MJ1 and TRN suction ports, MJ1 port on (left) and off (right).

## PIPELINE FLUSHING

---

### LITERATURE REIEW

A review of the literature was conducted that focused primarily on reports generated from previous flushing practices using (1) non-Newtonian HLW at Hanford and Savannah River sites, and (2) HLW simulants at national laboratories. The goal was to recognize the existing technological gaps and to develop test mythologies that could potentially bridge those gaps. This section explains the theoretical analysis and mythologies that were considered for future testing.

Results reported for flushing tests of 15 simulants in the WTP-RPT-175 Rev. 0 document (Poloski et al., 2009a) indicated that a minimum flush-to-line volume ratio of two would likely leave behind only small traces of particles in the pipeline. Increasing this ratio to three was suggested without guaranteeing that it would clean the pipeline completely. In addition, use of a system with automatic valve control based on different feedbacks was strongly suggested. The reported results for several tests indicated that velocity in the pipeline could reach values close to 20 ft/s before and after a maximum point in density profile. This maximum indicated a maximum of solid concentration in the pipe outlet. In several cases, high velocities were obtained even in steady conditions (flat sections of the density and velocity profiles) where traces of particles were probably flowing in the system. Flow of this solid-liquid mixture with these reported velocities which were higher than the upper limit set by the design guide (24590-WTP-GPG-M-0058, Rev. 0, Hall, 2006) can cause some level of erosion in the pipeline. This excessive velocity could be due to the nature of the system as the pneumatic system used for flushing provided flow rates on the order of 500 gpm to 1000 gpm for a 100-gallon loop. Erosion levels can be magnified by increased flush duration which could be the scenario in a cross-site pipeline at Hanford. To control the flow rate while maintaining pressure, an electric pump or other method can replace the pneumatic flush system.

Further, application of the suspension velocity correlation of Kale and Patwardhan (2005) and Wells et al. (2011) was examined. This correlation was originally developed for pulse jet mixer (PJM) applications and potential application of this correlation to pipeline flushing was investigated. Erosion of a sediment bed sitting in a pipe invert with a bed height equal to the fraction of pipe inside diameter was considered. It was assumed that a high-velocity flow entering a partially plugged pipe acts like a jet which impacts on the surface of the sediments. Determining the velocity of this jet, which is sufficient to erode this sediment layer with a length equal to multiple pipe diameters, is desired. The nozzle diameter was assumed to be the hydraulic diameter of the unplugged portion of the pipe's cross-sectional area, defined as  $d_j = 4 * A_{unplugged} / P_{unplugged}$ . Results of this preliminary application were compared to the critical velocity calculated from correlation of Oroskar and Turian (1980). Since the suspension velocity is usually higher than the critical velocity, this comparison could be used as a primitive check on the analysis. Table 3 shows the results obtained for a solid loading of 20%, solid and liquid densities of 2500 and 999 kg/m<sup>3</sup>, respectively, liquid viscosity of 1 cP, and length of the sediment layer of 1 meter or 13.2 times the pipe diameter (pipe diameter was selected as 3 inches or 0.078 m).

**Table 3. Calculation of Suspension Velocity for Particles in a 3” pipe**

D_pipe/z	V_susp	d_nozzle* (m)
2	10.43114	0.0046
3	7.780723	0.054
4	6.592275	0.059
5	5.954697	0.062
6	5.562316	0.064
7	5.297831	0.066
8	5.107917	0.067
This value is 0.04m in the analysis of Wells et al. (2011)		

To address some of the technical gaps noted in the literature review, it was suggested that FIU’s current pipeline unplugging system could be modified and used for flushing, re-suspension and potentially critical velocity studies. The current loop is 270 ft in length but there is room for expansion up to 2000 ft, if needed.

#### *Experimental Approach for Flushing Study*

To provide the necessary pressure head and flow rates in flushing tests, three systems were considered: (1) use of an elevated water tank with a fixed water level, (2) use of a variable-speed electric water pump, and (3) use of compressed air to pressurize water in a flush vessel. The third configuration is meant to advance the flushing system that was used in previous testing (Poloski et al., 2009a). The systems in the first and third configuration would be equipped with a motor-operated valve for flow rate adjustment. Results in WTP-RPT-175 Rev. 0 showed that adequate flushing was obtained with pressure reaching values of 80 to 100 psi during flushing of simulants. To construct the second system, an electric water pump capable of delivering 100 gpm of water at 80 psi could be a candidate to avoid high velocities in the system. A review of existing manufacturer products has indicated that a variable frequency drive may be needed to meet these requirements.

FIU’s flushing test loop will have some differences from the existing loops used for the Hanford waste testing. A controller module could be used to control the opening and closing of a motor-operated valve in the first and third system configuration, or to ramp up/down and shut off the electric pump in the second system configuration. All systems could be excited with a regulated signal from a controller module to provide variable pressure in the pipeline if such a practice could result in better flushing performance. This controller can analyze the signals received from a tank level transmitter and two Coriolis meters placed upstream (right after the water pump, elevated tank, or the flush vessel) and downstream (close to the capture tank) of the loop to correctly adjust the flow rate and duration of the flush. Signals from the upstream and downstream meters will indicate flow velocity and traces of particles (density), respectively. If density signals from the upstream and downstream meters are very close, then almost pure water is being discharged to the capture tank and the controller shuts off the water pump to end the flushing operation. As per FIU’s communications with manufacturers, Micro-Motion F series-2700 and 5700 models provide 4 to

20 mA signal outputs of mass and density that could be input into a LabView program for flow rate and velocity calculations and further used by the controller module.

A slightly more complicated but more accurate system would incorporate a sampling port with a valve just before the capture tank. Visual inspections or analysis through a particle size analyzer can then help to qualitatively and quantitatively evaluate the flush performance. Complexity can be increased by operating based on signals received from other instruments, such as a PulseEcho sensor, a Lasentec sensor, or from an optical probe in a clear section of the system (Goosen et al., 2011). The system could be designated empty if no results come from the PulseEcho and Lasentec sensors. Use of PulseEcho and Lasentec sensors in the loop can be an extension of the sensor utilization from particle velocity and size measurements in documents WTP-RPT-175 Rev. 0 0 (Poloski et al., 2009a) and WTP-RPT-189 Rev. 0 (Poloski et al., 2009b) to provide real-time monitoring of the particle presence and concentration during flushing operations.

In this study, a stationary bed will be manually created in the system. The procedure will be based on the sequential creation of sliding and stationary beds in the loop. FIU will initially run the system without the flushing tank/pump components in order to fill the system. Then, by changing valve configurations, the slurry will be circulated in the system without running through the mixing tank. This step is necessary to keep the solid content constant in the loop. At this stage, the system will function similar to the WRPS Waste Certification Loop. Then, the system will be run in steady state mode and near the deposition velocities to obtain a sliding bed that will be moving in the entire horizontal sections of the system. The effort will first focus on achieving a uniform bed in the entire system. Later, different sediment shapes will be achieved by ramping the velocity in different modes and rates.

FIU is currently investigating instrumentation that is capable of detecting particles in dilute concentrations in high-velocity streams. This condition occurs close to the end of the flushing operation. According to Denslow et al. (2011), PulseEcho cannot be used for this application because of insufficient backscattered signals. This issue was not reported for the Lasentec sensor. Results reported by Bontha et al. (2000) showed the capability of this sensor to detect particles in the range of 0.8 to 1000  $\mu\text{m}$ . Lasentec can produce particle size distributions and update this information every two seconds (according to Poloski et al., 2009a) which is a relatively long time for this application. FIU is currently interested in the possibility of obtaining data from Lasentec in much shorter time intervals.

Initial phases of this study will involve simple simulants which can physically represent actual waste in the WTP. Simple simulants that were used in PNNL's M1 tests (Poloski 2009a, b and Yokuda et al., 2009) will be considered. The goal will be to compare results obtained by FIU's loop with those obtained in M1 test results as a baseline test. Other important criteria in the selection of simulants is the availability of flushing test results and the similarity of test loops to FIU's loop. For this reason, simulants used in the PNNL-17639, WTP-RPT-175 Rev. 0 report (Poloski 2009a) were considered. Various simulants in the form of glass beads (two sizes, 10  $\mu\text{m}$  and 100  $\mu\text{m}$ ), 50  $\mu\text{m}$  alumina, and 316 stainless steel (two sizes, 10  $\mu\text{m}$  and 100  $\mu\text{m}$ ) in water-kaolin suspension will be considered.

For the initial studies, FIU will choose one or two simulants from a matrix of 6 non-Newtonian simulants based on ease of testing and availability of material. Instability issues associated with simulants used in the PNNL-18316 WTP-RPT-189 Rev. 0 document (Poloski et al., 2009b) will be considered. In preparation of the test matrix for simulant selection, size, density, yield stress,

and viscosity will be considered. Water will be the primary component of the carrier fluid. Kaolin clay and MgSO<sub>4</sub> (in 10 ppm) will be used to adjust the shear viscosity and yield stress, respectively. Kaolin clay with particle size of 1 μm and density of 2~3 g/cm<sup>3</sup> will be considered. Medium- and high- rheology simulants ( $\tau_y = 3$  and 6 Pa) with small, medium, and high density, and medium and large particle sizes will be considered in the initial test matrix. Table 4 shows the matrix for simulant selection for the flushing tests.

**Table 4. Candidate Simulants for Use in Initial Phases of the Flushing Tests**

name	Al <sub>2</sub> O <sub>3</sub> -MR	GB-MR	SS-MR	Al <sub>2</sub> O <sub>3</sub> -HR	GB-HR	SS-HR
Volume fraction % (Mass fraction %)*						
Coarse Particle	9.5(25.6)	8.4(16.9)	3.9(22.9)	9.7(25.7)	10.7(20.6)	4.8(26.5)
Kaolin Clay	8.9(16.0)	7.7(15.5)	6.5(11.8)	10.7(18.7)	9.6(18.4)	6.4(11.2)
Water	81.6(58.4)	83.9(67.6)	89.6(65.3)	79.6(55.6)	79.7(61.1)	88.8(62.2)
Al <sub>2</sub> O <sub>3</sub> : Aluminum Oxide, density: 4~6 g/cm <sup>3</sup> , particle size:50μm G.B. : glass beads, density: 2~4 g/cm <sup>3</sup> , particle size: 100μm SS: Stainless Steel, density:8~10 g/cm <sup>3</sup> , particle size: 100μm MR and HR stand for medium rheology ( $\tau_y = 3$ Pa) and high rheology ( $\tau_y = 6$ Pa), respectively. * Mass fraction will be varied in each round of tests. Values are available in Poloski et al. (2009a) and are the baseline for future variations. Solid loading will be changed with ±5% and ± 10% increments.						

Initial testing will start with a 165-foot loop which is similar to PNNL’s M1 test loop in length. FIU will also focus on mid-density material such as aluminum oxide in both high and medium rheologies. Studies will continue with high-density stainless steel in later phases in addition to the full range of particle sizes and different test loops lengths.

Variables considered in the test matrix will include: simulant material (carrier material type, particle type and concentration), operation of pump mode (fixed, ramped, pulsing), flush duration, number of flushes (1, 2, and 3), bed formation (triangular, rectangular, and waveform) and loop length (165, 330, 495, 660, and 825 ft).

In the initial phases of the flushing study, a fixed-volume test strategy will be used. A potential test matrix is provide in Table 5, with a total of 24 tests for the initial phase of testing. This table shows the test matrix using a simulant with 16% kaolin clay, 25.6% AL<sub>2</sub>O<sub>3</sub> and 58.4% water for the 165 foot test loop that creates a uniform sediment bed. Resultant flush duration and line to volume ratio are also calculated and shown in the left two columns. The sediment shape will not be the priority in the initial phases and uniform beds will initially be obtained in the system. Best flush practices will be evaluated by starting the flushing with a resulting total flush-to-line volume of 2. Low values were selected because testing results in WTP-RPT-175 Rev. 0 showed a sudden drop of velocity after the velocity reached a maximum. The challenge will be to examine low values by keeping the flow velocity constant during flushing. In this test phase, the tank level indicator will be used for flush volume calculations. The indicator signal will also be used for stopping the pump.

When signals received from the Lasentec indicate there are no particles detected, the pump will be stopped. For performance evaluations, signals from a Coriolis meter will be considered as well.

Therefore, columns related to total and per-flush line-to-volume ratio are tentative. This practice will be similar to those reported in WTP-RPT-175 Rev. 0. In subsequent phases, FIU may consider target flush volumes and stop the pump based on the signal received from the tank level indicator. In addition, non-uniform sediment shapes, stainless steel beads and longer test loops may be considered in a future test matrix.

**Table 5. Matrix for Flushing Test using 165-ft Test Loop**

Test Number	Flush Mode	Number of flushes	Flush to line volume ratio, (per flush)	Resultant Duration Per flush (sec)	Resultant flush to line volume ratio
1	Constant*	1	2	27.4	2
2	Ramped	1	2	27.4	2
3	Pulsed	1	2	27.4	2
4	Constant*	2	1	13.7	2
5	Ramped	2	1	13.7	2
6	Pulsed	2	1	13.7	2
7	Constant*	1	3	41	3
8	Ramped	1	3	41	3
9	Pulsed	1	3	41	3
10	Constant*	2	1.5	20.5	3
11	Ramped	2	1.5	20.5	3
12	Pulsed	2	1.5	20.5	3
13	Constant*	1	4	54.8	4
14	Ramped	1	4	54.8	4
15	Pulsed	1	4	54.8	4
16	Constant*	2	2	27.4	4
17	Ramped	2	2	27.4	4
18	Pulsed	2	2	27.4	4
19	Constant*	1	5	68.4	5
20	Ramped	1	5	68.4	5
21	Pulsed	1	5	68.4	5
22	Constant*	2	2.5	34.2	5
23	Ramped	2	2.5	34.2	5
24	Pulsed	2	2.5	34.2	5

\* This value must be found experimentally. The default value is 12 ft/s if no plugging formation will be observed. Ramping starts from a safe velocity (default 8 ft/s) that must also be found and the continues to 12 ft/s Pulse will be between the safe velocity (default 8 ft/s) and the maximum velocity (12 ft/s)

Proposed test loop operations

Defining a correct test protocol consisting of sequential steps was an important step in developing a suitable test plan. The proposed protocol includes the following general steps:

1. Create and mix the simulant in the mixing tank.
2. Run the slurry pump to fill the system.

3. Circulate the slurry by bypassing the mixing tank and create a stationary bed after creating a sliding bed and stopping it. At this stage, the system will function similarly to the WRPS Waste Certification Loop (Bontha et al., 2010).
4. Control the solids loading by changing the concentrations in the slurry mixing tank and bring the mixing tank back to the loop. Return to step 3.
5. Start the flushing test and stop after a certain time or after a certain flush volume.
6. Evaluate how much solid is left behind after step 5. One of the following will be used:
  - a. Capture the residual solids in a special filter bag inside the capture tank.
  - b. Circulate the residuals in a loop using the slurry pump and capture the residual solids progressively in a special filter inside a water tank. This step requires cleaning the slurry pump using water in a special cleaning line.

The proposed test loop will be an integrated test loop for flushing studies with the potential for evaluating critical velocities. This loop, as shown in Figure 18 and Figure 19, was designed to have the following features: (1) detection of the onset of particle deposition using the PulseEcho sensor, (2) inline monitoring of particles in the flush stream, (3) post-flush evaluation of solid residuals, (4) cleaning of slurry pump and its attached line, (5) modularity in length (165, 330, 495, 660, and 825 ft), (6) automatic control of valves and the flush pump, (7) automatic termination of flush operation using signals from Lasentec and an in-tank level transmitter, and (8) several visualization sections for easy visualization of the flow.

FIU is in the process of assessing the availability of equipment that is necessary for simulant preparation as well as flow rate and pressure measurements. The current test loop at FIU is a pipeline system, approximately 270 feet in length and consists of 3-inch-diameter carbon steel schedule 40 pipes. The system is currently ready to be connected to tanks, pumps, and other instrumentation to form a test loop. FIU has the capacity to make this pipeline shorter or longer (up to 2000-ft) for down-scaling and up-scaling purposes. Figure 19 shows a schematic of a down-scaled loop with 90, 180, and 270-foot lengths.

It is expected that the proposed system will allow for visibility of sediment bed or plug formation and characterization of the system before and after flushing operations. A list of proposed instrumentation is included in Table 6.

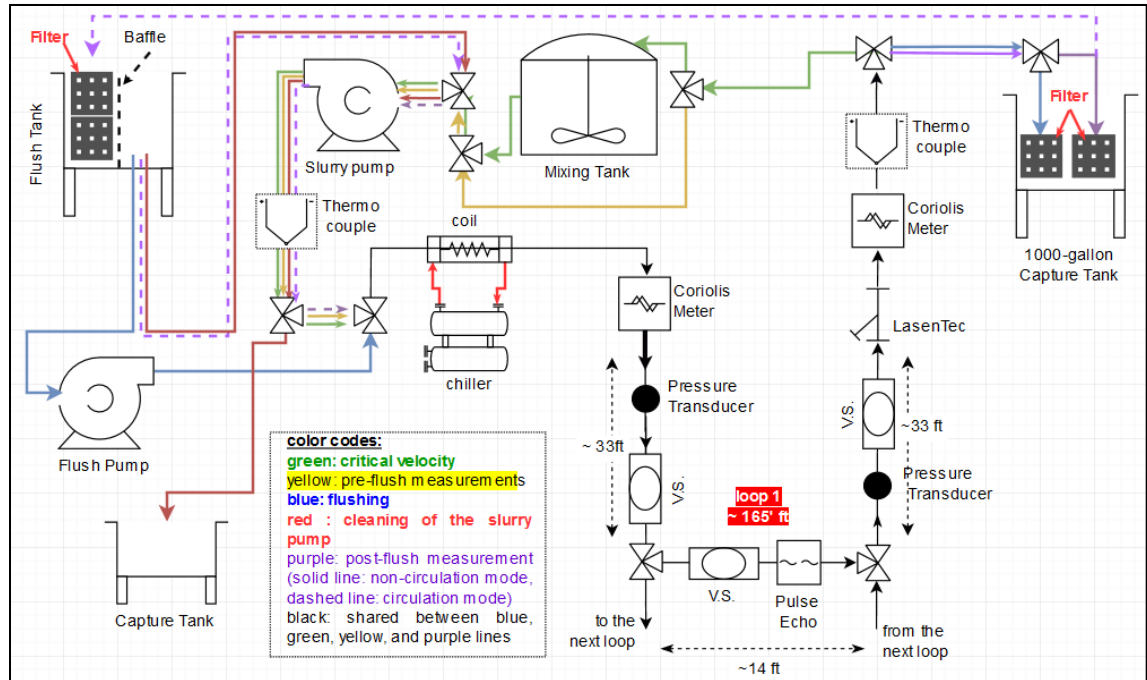
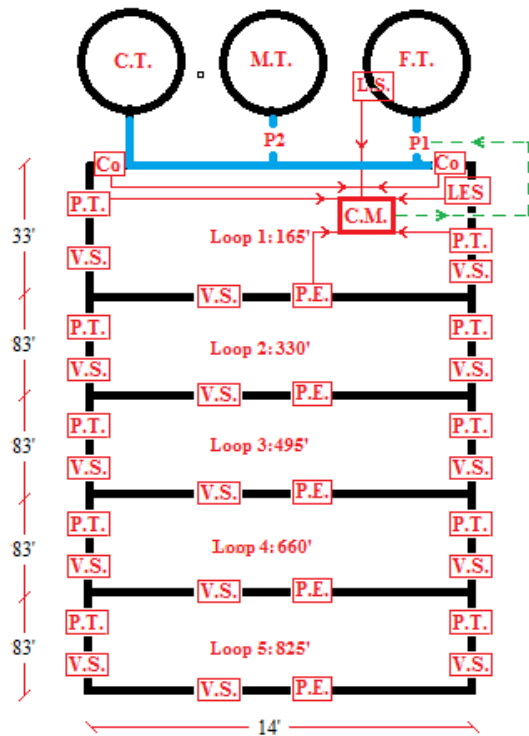


Figure 18. FIU's proposed test loop.



- F.T. : flush tank
- C.M.: controller module
- C.T. : capture tank
- M.T.: mixing tank
- LES : Lasentec
- L.S.: tank level sensor
- P1 : flush pump
- P2 : slurry pump
- P.E.: PulseEcho sensor
- V.S.: Visualization section

Figure 19. FIU's proposed variable-length loops (left) and an existing 270-ft pipeline at FIU (right).

**Table 6. Information Required from Flushing Test**

<b>Variable</b>	<b>Instrument type</b>	<b>#</b>
Mass flow rate	Coriolis meter Micro-Motion F series model 2700	2
Density		
Pressure	differential pressure transducer	2,4,5,6,8,10
Mixing tanks with agitator	400 Gallons	1
Water tank	1000 Gallons	1-2 <sup>(a)</sup>
Capture tank	1000 Gallons	1-2
Electric water pump	TBD <sup>(b)</sup>	1
Slurry velocity and stratification	PulseEcho	2 <sup>(c)</sup>
Sediment bed characterization	PulseEcho	1
Particle trace measurement	The Mettler Toledo Lasentec	1
Control module	TBD	1
Motor-operated valves	TBD	1
Tank level transmitter	TBD	1
Rheometer	TBD	1
Slurry pump	TBD (15 HP for 165' loop)	1
Particle size analyzer	TBD	1
Data Acquisition (DAQ)	TBD	1
Flow characterization/observation	Visualization section	3,5 <sup>(d)</sup>
Slurry temperature control	Chiller	1
Slurry temperature	Thermocouple	2

## CONCLUSIONS

---

A turbulent velocity profile obtained from a RANS simulation with the Inverse\_Global\_alpha method closely matched the experimental profile at  $Re=25300$ . Considering the results obtained in the previous year for the mean velocity, it is concluded that this version can reliably represent fully turbulent flows. A conclusion could not be drawn for any versions of the alpha model for the transitional flows when considering both the mean and turbulent velocity profiles together. Efforts for validating turbulent quantities of a transitional flow using a fully turbulent model was not conclusive.

Mean and turbulent velocity profiles were also obtained for the Q-DNS-HB simulation of the fully turbulent flow and a close agreement with the experimental values were obtained. With that verification, shear dependency analysis of the Q\_DNS\_HB simulation results indicated convergence of shear rate to constant values in high  $\epsilon/k$  values. Converged values were  $1867 \text{ s}^{-1}$  and  $1782 \text{ s}^{-1}$  for  $u_{rms}/\eta = [0 \text{ to } 400 \text{ s}^{-1}]$  and  $u_{rms}/\eta > 400 \text{ s}^{-1}$ , respectively.

Furthermore, comparison between RANS-alpha and Q-DNS-HB simulations showed that variations of shear rate versus  $u_{rms}/\eta$  were qualitatively similar. Similarity was observed for the shear rate variations against TDR/TKE if only high values of  $u_{rms}/\eta$  (bottom envelope of  $Y$  versus TDR/TKE) were considered. For this reason, only the Q-DNS-HB simulation results were considered for generation of a shear rate modification algorithm.

Implementation of the Q-DNS-HB-based shear rate modification algorithm in the RANS-HB was successfully demonstrated in Star-CCM+. Shear alterations resulted in remarkable improvement of accuracy over most of the range of  $r/R$  and results converged to those of the RANS-alpha and Q-DNS-HB methods with less than 2 percent deviation. Potential future work could focus on extending the shear dependency analysis presented to different Reynolds numbers and for the same or different simulant/s using Q-DNS-HB and RANS-HB approaches.

CFD simulations of the in-tank waste mobilization showed that simulating erosion without changing the volume fraction directly in Star-CCM+ was possible. It was shown that without solution of the granular temperature and pressure, a symmetric diffusion occurs to the solid layer, which did not comply with asymmetric boundary conditions of the simulation. However, setting a large value of viscosity in the solid layer resulted in deformation of the sediment layer and diffusion of the solid in the liquid phase (suspension). This solid diffusion increased over time at an extremely slow rate, which was related to the fact that the artificial viscosity was set to a significantly large value. Potential future efforts could focus on the incorporation of the calculation for solid pressure and granular temperature, which sets additional bounds to the solid volume fraction.

Simulations in the 1:21 scaled tank showed a significant impact due to the presence of the MJP suction port. This could be due to any inaccurate modeling parameters or potential numerical limitations caused by the proximity of the suction ports to the tank bottom and MJP nozzles. Potential future work could be to evaluate the effects of mesh size and solution schemes on the numerical accuracy and performance. The aim would be to obtain converged solutions with the presence of MJP suction ports that are connected to MJP nozzles via a field function for mass flow rate. A rotating jet could be created via a sliding mesh in the model and similar investigations could be performed.

Finally, a test plan consisting of protocol, matrix, and experimental test loop was proposed to evaluate technical gaps in current flushing operations. The test plan is currently being evaluated by engineers from PNNL and SRNL. Their feedback regarding simulant composition, test matrix, instrumentation, and test protocol will be incorporated into the test plan. Future work will include finalizing the test plan and modification of the current test loop. Subsequent testing phases may involve varying initial sediment configurations, simulant composition and pipeline length. The test loop can also be modified to address other relevant waste transfer issues including critical velocity and erosion and corrosion.

## TASK 17.1.2

# CFD MODELING OF NON-NEWTONIAN FLUID UNDERGOING SPARGING (FIU YEAR 7)

### EXECUTIVE SUMMARY

---

The Waste Treatment and Immobilization Plant (WTP) will house pulsed jet mixers (PJMs) in waste processing tanks that require improved computer models for the prediction of slurry mixing behavior. The nature of the high level-waste (HLW) in these tanks can be represented using non-Newtonian fluid viscosity modeling. In order to enhance and expedite this mixing process, the implementation of sparging to the PJMs is being considered. Currently, the PJM process is undergoing research and validation at NETL's Morgantown site. At this site, an experiment investigating the time for a tracer to become fully mixed in the non-Newtonian fluid while undergoing sparging was conducted. This is due to a lack of knowledge on the effect of rheological properties and sparging flow rates on the flow characteristics of the PJM vessels for improved mixing.

A sparging application that has been researched prominently in the scientific community is that of bubble columns. In the analytical assessment of flow characteristics in bubble columns, the radial air volume fraction and axial velocity profiles are studied. Numerous studies, numerical and experimental, have been conducted on bubble columns with Newtonian fluids. These studies have investigated the effects of alterations on the rheological properties, sparging flow rates, and characteristic ratio ( $\frac{H}{D}$ ). A few experimental works on bubble columns which contain non-Newtonian fluids have been conducted in the literature. These works have looked into the effect of altering the rheological properties and sparging flow rates but not on the  $\frac{H}{D}$  ratio effects. Specifically, there is no literature investigating flow characteristics in  $\frac{H}{D}$  ratios as low as those observed in the PJM waste tanks. Furthermore, no literature on simulating sparged non-Newtonian fluids has been identified. Thus, the purpose of this task is to use CFD in order to study the flow characteristics under PJM characteristic ratio.

The current CFD study uses existing experimental work on non-Newtonian bubble columns to develop and validate a CFD model. The model produced closely matched the experimental radial air volume fraction profile and qualitatively matched the experimental radial air axial velocity profile. This simulation then used the develop simulation to assess the flow characteristics at five different characteristic ratios, namely  $\frac{H}{D} = 5.2, 3.8, 2.4, 1.37, \text{ and } .34$ , where the lowest  $\frac{H}{D}$  ratio pertains to that of the PJM geometric condition. The results showed a trend of flattening radial air volume fraction and radial air axial velocity profile with decreasing characteristic ratio. This was attributed to the relative proximity of the sparging flow rate inlet location to the height of the column, not giving enough time for fully developed flow. In addition, a slight increase in volume fraction magnitude and a decrease in air velocity magnitude are observed with decreasing characteristic ratio. A plug profile for both air axial velocity and air volume fraction is expected for sparging under PJM geometric conditions.

## INTRODUCTION

Many engineering processes at various U.S. Department of Energy sites include the flow of nuclear waste in a liquid form that is characterized as a non-Newtonian fluid. These operations require that the waste be properly mixed. Pulse jet mixing (PJM), as shown on the left of Figure 20, is one of the methods selected by the DOE to mix the HLW slurry prior to the vitrification process. This method involves sucking a portion of the waste from the tank into a pressurized vessel and then injecting it back into the tank in order to mix the waste using pressurized jets. This process is repeated over a number of cycles until the desired level of homogeneity is achieved [1].

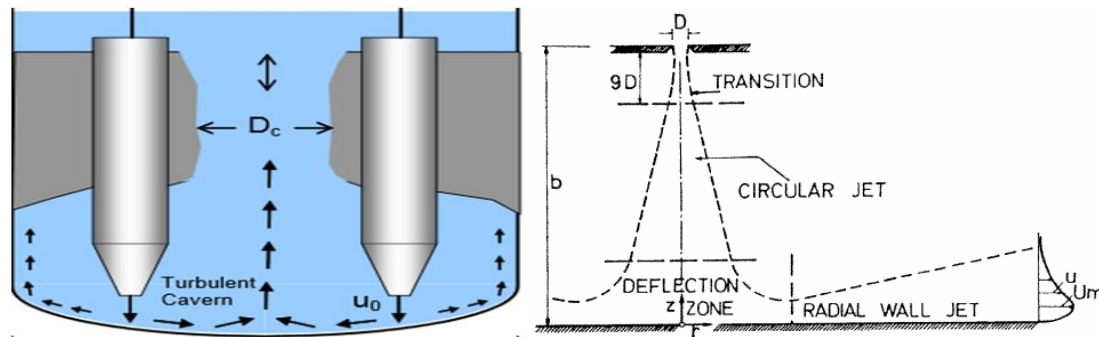


Figure 20. General flow structure in PJM vessel (left), radial wall jet depiction (Poreh et al. 1967) (right).

Currently, the PJM process as applied to the nuclear waste at Hanford is undergoing research and validation. For example, the implementation of sparging during the PJM process is being considered in order to expedite the mixing process. At NETL's Morgantown site, testing of the PJM process with non-Newtonian fluid is currently being directed. An experiment investigating the time for a tracer to become fully mixed in the non-Newtonian fluid while undergoing sparging was conducted. This is due to a lack of knowledge on the effect of rheological properties and sparging flow rates on the flow characteristics of the PJM vessels for improved mixing.

The primary focus of this task is to conduct computational fluid dynamics (CFD) analysis to develop a simulation that is capable of studying the effects that rheological properties, characteristic dimensional properties, and sparging flow rates have on the sparging process. An assessment of this aspect of the PJM process is critical to the successful design and implementation of the PJMs which are used for treatment and storage of nuclear waste.

## LITERATURE REVIEW

Gas-sparged vessels have been used in process industries for a number of years. Bubble column is a general term describing gas-sparged vessels. Bubble columns are widely used in the chemical industry and in several applications within the nuclear energy industry [3]. Specific applications of bubble columns are seen in the production of baker's yeast, citric and amino acids, metals, microbial fuel cells, and many more [4-8]. These kinds of systems are widely used because they offer favorable mass transfer and mixing characteristics at a feasible cost due to their mechanical simplicity [9].

The existing literature on bubble columns articulates the unsteady behavior flow in a bubble column. This unsteady behavior is a significant factor in the mixing and transport progression in bubble column flows and occurs at varying spatial and temporal scales [10]. These unsteady features are undoubtedly affected by geometrical factors (e.g., liquid height, geometric characteristics, and sparger flow rate). For this reason, experimental works on bubble columns are identified by a liquid height, characteristic length, and a superficial gas velocity range (sparger flow rate). One of the significant effects of the mentioned parameters is on the nature of the bubble flow, as shown in Figure 21.

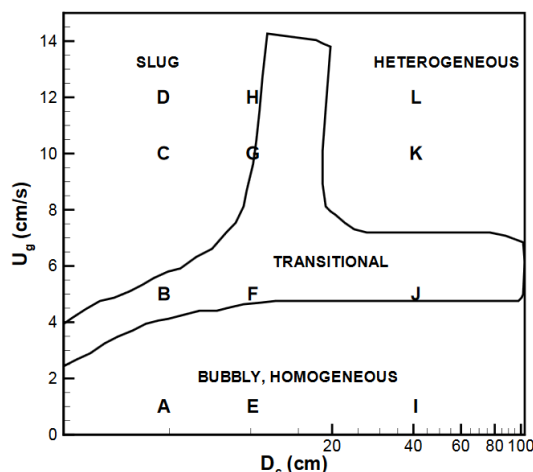


**Figure 21. Bubble column flow regime based on characteristic length and flow rate.**

From Figure 21, it can be seen that there are four different kinds of bubbly flow in a bubble column as a function of the superficial gas velocity  $U_g$  and column diameter  $D_c$ . These are homogenous, heterogeneous (Churn-turbulent), transitional, and slug bubbly flow regimes. Homogenous and heterogeneous bubbly flows characterize the distribution of bubble diameters. Slug flows are characterized by an agglomeration of bubbles which are observed to be passing large bubbles. The context of this effort maintains its focus on homogeneous bubbly flow as that is the flow that is proposed for the PJMs.

In the literature, most of the earlier experimental studies were conducted on rectangular bubble columns and mainly focused on investigating time averaged behavior of a Newtonian fluid. For example, Becker et al., Pflieger et al., Pan et al., and Buwa all studied rectangular bubble columns [11-15]. According to Rampure et al., this was due to the fact that plume oscillations in this geometry were already well established. It was also due to simpler geometry, which reduces

computational requirements while still retaining key characteristics observed in cylindrical bubble columns.

Experimental studies of cylindrical bubble columns, the shape of the waste tanks at Hanford, have also been conducted for Newtonian fluids. For example, Chen et al. [16] studied the effect of column size on heat transfer characteristics and volume fraction profile under  $\frac{H}{D} \cong$  of 10, 5, & 2.5 and superficial gas velocities of .02-.09  $\frac{m}{s}$ . Chen recorded that gas volume fraction profiles were parabolic and symmetric in nature. He also noted that with increasing  $\frac{H}{D}$  there was a flattening of the parabolic gas volume fraction profile. Rampure et al. [10] investigated the effects of  $\frac{H}{D} = 5$  and 10 under superficial gas velocities of .01-.2  $\frac{m}{s}$  on the dynamic and time averaged flow behavior of cylindrical bubble columns. Rampure also noticed that oscillations of bubble swarms had varying time scales, unlike that of rectangular bubble columns. In a later study, Rampure et al. [17] also studied bubble columns at higher superficial gas velocities (up to .4  $\frac{m}{s}$ ) under a similar characteristic ratio ( $\frac{H}{D}=5$ ) by measuring local time-averaged gas holdup and velocity profiles. Rampure also looked into mixing times, where the mixing times asymptotically approached a minimum value as superficial gas velocities were increased. As a more recent example, McClure et al. [18] investigated bubble size distribution (BSD) as a function of sparger design using  $\frac{H}{D}=2.5$  and superficial gas velocities of .01 to .11  $\frac{m}{s}$ . McClure observed that BSD in water air systems changed significantly with column height and insignificantly with increasing superficial velocities at the range tested.

Experimental investigations of cylindrical bubble columns with non-Newtonian fluid are not as plentiful in number as they are with Newtonian fluids. Amin E. et al. [19] showed radial distribution of both upward gas velocity and volume fraction for an array of non-Newtonian fluids in a bubble column with a  $\frac{H}{D}=2.5$  tested at superficial velocities between .04 and .2  $\frac{m}{s}$ . Cécile et al. [20] similarly studied mixing time in a bubble column using non-Newtonian power law fluids as a function of superficial gas velocities. The experiment had an  $\frac{H}{D}=1.75$  and was tested at superficial gas velocities of .001 - .008  $\frac{m}{s}$ . Kawase et al. [21] conducted experiments on a bubble column with fermentation broths having a yield stress behavior. In his work, he detailed total gas hold up as a function of superficial velocity and axial velocity as a function of superficial velocity for a superficial velocity range of .01 and .1  $\frac{m}{s}$ . Although this fluid is the one of interest, no information on radial distributions of these quantities is given which would better serve for proper validation. Lastly, Junya Knitta et al. [22] investigated cylindrical bubble columns with fluids showing both yield stress and power law behavior. Junya also recorded total gas hold up, but noticed that a certain amount did not escape the bubble column due to the yield stress behavior. This experiment was performed for  $\frac{H}{D}=5, 10$  under superficial gas velocities of .01 to .1  $\frac{m}{s}$ .

In addition to the experimental work conducted on cylindrical bubble columns, CFD simulations in this subject have also been conducted but are limited in number. McClure et al. [18, 23] have conducted Euler-Euler transient simulations of Newtonian bubble columns, matching axial velocity and volume gas fractions profiles radially at different heights. Mohan et al. [17] conducted

similar simulations and was able to accurately capture data for a range of superficial gas velocities ( $0-4 \frac{m}{s}$ ). Lijia Xu et al. [24] also used a Euler-Euler approach to investigate gas volume fraction profiles of a slurry in a bubble column. The viscosity model used in this approach was the Thomas semi-theoretical correlation, which does not take into account yield stress.

The CFD studies mentioned recognized the drag force, lift, particle induced turbulence, and virtual mass force as relevant forces to be considered. Furthermore all three studies used RANS modeling, neglected virtual mass force, and agreed that drag was the most dominant force largely contributing to the dynamics of the problem. Worthy of note is that McClure et al. was the only study which took turbulent dispersion into account while Lijia Xu et al. was the only study to incorporate the lift force. All the mentioned CFD studies were conducted using different versions of the commercial code Fluent. To the authors knowledge, there are no CFD simulation models of bubble columns with power law or visco-plastic fluids.

Given the limited examinations conducted on sparged non-Newtonian fluids, it is not surprising that none of the studies investigate the  $\frac{H}{D}$  ratio and shear thickening effect on non-Newtonian bubble columns. This area of study is beneficial to the implementation of sparging as a second means of mixing in the PJM process due to the fact that waste tanks are known to vary in size and thus capacity. These parameters will be the focus of this work.

## NUMERICAL APPROACH

---

In order to investigate rheological and physical effects on a sparged non-Newtonian fluid, a finite volume method was employed using the commercial code ANSYS Fluent v16. All of the theory presented is obtained from the Ansys fluent theory manual [25] and includes the governing equations, initial conditions, and boundary conditions.

### Governing equations

The Eulerian-Eulerian multiphase flow model in ANSYS Fluent V14.5 was chosen to simulate all of the bubble column simulations. An alternative to the Eulerian-Eulerian model for bubbly two-phase flow is the Eulerian-Lagrangian model, where bubbles are individually tracked as a discrete phase. The Eulerian-Lagrangian model for this reason becomes computationally intensive for large quantities of discrete phases, leaving the Eulerian-Eulerian model the feasible alternative for this work.

The main characteristic of the Eulerian-Eulerian model is that it mathematically represents each phase as interpenetrating continua. In addition, the volume of a phase cannot be occupied by another phase, introducing the concept of volume fraction. The sum of all volume fractions is equal to one for all space and time. This is mathematically expressed in ANSYS Fluent V14.5 user's manual for each phase as:

$$\sum_{o=1}^n \alpha_o = 1 \quad (1)$$

where  $\alpha$  represents the volume fraction of phase  $o$ . In the bubble column under question, only two phases exist, namely the non-Newtonian liquid and gas in the form of air. The liquid is referred to as the primary phase and the gas is referred to as the secondary phase. The effective density of each phase is calculated in the following manner:

$$\widetilde{\rho}_o = \alpha_o \rho_o \quad (2)$$

where  $\rho_o$  is the density of phase  $o$ . Furthermore, the conservation of mass and momentum laws are fulfilled by each phase, meaning that a set of equations is solved per phase. The continuity equation for phase  $o$  is:

$$\frac{d}{dt}(\alpha_o \rho_o) + \nabla \cdot (\alpha_o \rho_o \vec{v}_o) = \sum_{p=1}^n (\dot{m}_{po} - \dot{m}_{op}) \quad (3)$$

where  $\vec{v}_o$  is the velocity vector of phase  $o$  and  $p$  represents the second phase. In this study, no mass transfer or reactions occur, equating the continuity equation to zero. The conservation of momentum equation for each phase  $o$  is:

$$\frac{d}{dt}(\alpha_o \rho_o \vec{v}_o) + \nabla \cdot (\alpha_o \rho_o \vec{v}_o \vec{v}_o) = -\alpha_o \nabla P + \nabla \cdot \vec{\tau}_o + \alpha_o \rho_o \vec{g} + \sum_{o=1}^n K_{po} (\vec{v}_p - \vec{v}_o) + (\vec{F}_o + \vec{F}_{vm,o}) \quad (4)$$

where  $P$  is the pressure,  $\vec{\tau}_o$  is the stress tensor,  $\vec{g}$  is gravity,  $K_{po}$  represents the interphase momentum exchange coefficient,  $\vec{F}_o$  is the body force, and  $\vec{F}_{vm,o}$  is the virtual mass force.

The first term on the left hand side of Eq. (4) represents the transient changes in momentum and the second term is the changes of the convection term. The first term on the right hand side takes into account pressure changes. The second term on the right hand side represents the stress tensor term, defined by:

$$\bar{\tau}_o = \alpha_o \mu_o \left( \nabla \bar{v}_o + (\nabla \bar{v}_o)^T \right) + \alpha_o \left( \lambda_o - \frac{2}{3} \mu_o \right) \nabla \cdot \bar{v}_o \bar{I} \quad (5)$$

where  $\lambda_o$  and  $\mu_o$  represent the bulk and shear viscosity of phase o, upper script T symbolizes the transpose, and  $\bar{I}$  is the identity matrix. Furthermore, the third term takes into account acceleration due to gravity. The fourth term includes the interaction forces between the two phases as well as mass transfer between phases. The fifth and final term on the right hand side represents the body force and the virtual mass forces.

In the context of this work, there is no mass transfer and the compressibility of phases will be neglected, yielding the following conservation of mass equation:

$$\frac{d}{dt} (\alpha_o \rho_o) + \nabla \cdot (\alpha_o \rho_o \bar{v}_o) = 0 \quad (6)$$

and the following stress tensor:

$$\bar{\tau}_o = \alpha_o \mu_o \left( \nabla \bar{v}_o + (\nabla \bar{v}_o)^T \right) \quad (7)$$

The interphase exchange coefficient is a function of the drag. The Schiller-Naumann drag model is used as it is well accepted in the area of bubbly multiphase flows ([3], [26]). The drag force predicted by Schiller-Naumann model is described as follows:

$$f = \frac{c_D R_e}{24} \quad (8)$$

where  $c_D$  the coefficient of drag and  $R_e$  is the Reynolds number. The coefficient of drag is computed in the following manner:

$$c_D = \begin{cases} \frac{24(1+15R_e^{.687})}{R_e}, & R_e \leq 1000 \\ .44, & R_e \geq 1000 \end{cases} \quad (9)$$

where

$$R_e = \frac{\rho_o |\bar{v}_p - \bar{v}_o| d_b}{\mu_o} \quad (10)$$

## Turbulence

The turbulence model chosen for this multiphase flow is the RANS  $k - \varepsilon$  RNG model. It is important to note that the standard  $k - \varepsilon$  model was originally intended for single phase flow but several studies such as the ones conducted by Dale McClure, Rampure et al., Sokolichin, and Eigenberger [10, 18, 27] have shown that the standard  $k - \varepsilon$  models give physically accurate results for bubble columns. This fact supports the use of the  $k - \varepsilon$  RANS models in bubble column simulations. Furthermore, Xe et al. [28] and Laborde-Boutet et al. [29] investigated the

implementation of different  $k$ - $\epsilon$  models and compared simulation results with the experimental data of Chen [30]. The results indicated that RNG  $k$ - $\epsilon$  model was best able to capture the flow characteristics in bubble columns within the turbulent regime.

### Rheological modeling

In Fluent, there are a number of ways to model non-Newtonian fluids. For the scope of this work, the power law model in Fluent is discussed. The non-Newtonian viscosity for isothermal conditions is given by:

$$\eta = k * \dot{\gamma}^{n-1} \quad (11)$$

where  $k$  and  $n$  are the consistency index and power law index, respectively. The value of the power law index determines what kind of fluid it is. If  $n$  is equal to one, then it is a Newtonian fluid. If  $n$  is greater than one, it is referred to as a shear thickening fluid and, lastly, if  $n$  is less than one, the fluid is shear thinning.

In order to obtain a reliable CFD model, a number of steps are taken to validate the final model through which sparging of a non-Newtonian fluid may be investigated. This is achieved by first validating a simulation of sparged Newtonian fluid with existing experimental data. Then a second simulation will be conducted in which experimental data of power law fluids is matched. Once a degree of accuracy is reached within the validation process, rheological and physical characteristics of the simulation will be altered systematically and conclusions will be discerned.

## RESULTS & DISCUSSIONS

Xe et al. [28] conducted numerical simulations of bubble column flows in a churn-turbulent regime using a Euler-Euler approach with an RNG  $k-\varepsilon$  model. The numerical simulations matched time averaged radial gas volume fraction and axial velocity profiles with experimental data conducted by Chen et al. [30]. Xe's bubble column simulation was replicated using the geometry and boundary conditions depicted below:

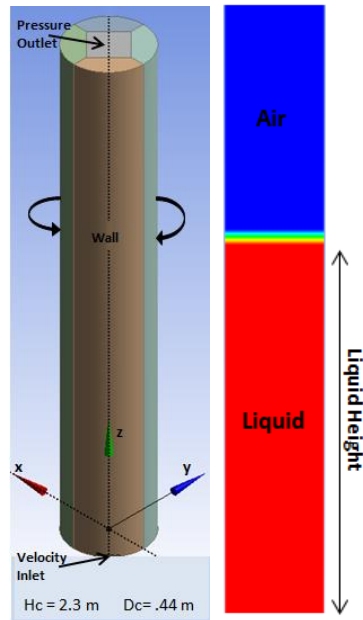


**Figure 22. Boundary Conditions, physical characteristic (left) and Initial conditions (right) of Caixia Chen simulation.**

As can be seen in Figure 22, the .44 m diameter column with a height of 2.3 meters has 3 boundary conditions: namely a velocity inlet, pressure outlet, and a wall. The liquid height in this experiment was kept at 1.1 m. The simulation was run for 90 seconds with a time step of .01 seconds in order to reach a quasi-steady state. The results were obtained by time averaging field variables for the last 30 seconds, for a total simulation time of 120 seconds. Xe et al. used the Schiller Neumann Drag model and thus, was used in this replication. The same simulation was produced using different mesh sizes so that a mesh independent model could be acquired. The comparison between the replicated simulation and Chen's experimental data at one location in the bubble column is shown below:

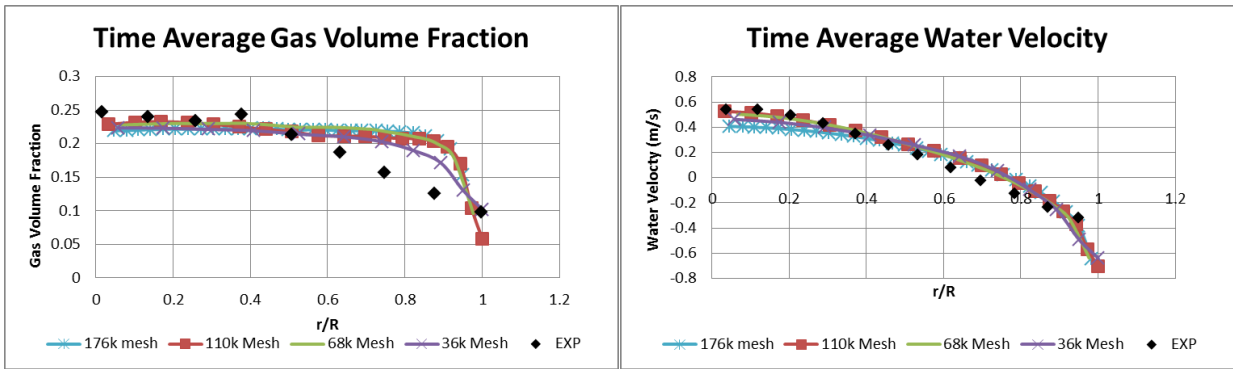


**Figure 23. Replication of Xe's simulation results compared to chen's experimental data.**

From Figure 23, it can be observed that the model is mesh independent. The 36 thousand mesh count starts to deviate from the more refined meshes, so a 68 thousand mesh count is deemed as optimum. Furthermore, the comparison shows that the time averaged velocity is matched very well to the experimental data, as is in Xe’s simulation. The volume fraction profile of the simulation replication matches the experimental data quantitatively well. However, the profile shape of the volume fraction of the simulation has more of a plug profile. This discrepancy is also observed in Xe’s work. The final mesh has 28 cells in the radial direction, 44 in the circumferential and 42 cells in the axial direction per meter, as is shown below in Figure 24.

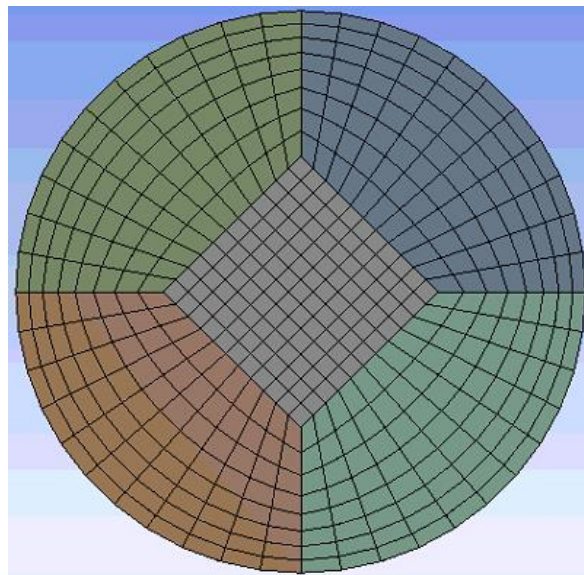


**Figure 24. Cross section view of mesh for parametric study.**

A uniform hexahedral conformal mesh is used, as other meshes tend to introduce instabilities as suggested by others who simulated Newtonian bubble columns [18, 23, 31]. With a model that can capture the general physics of a bubble column operating with Newtonian fluid along with gained perspective of appropriate meshing and numerical methods, a model taking into account a non-Newtonian fluid was initiated.

### Simulation of bubble column operating with non-Newtonian fluid

Amin et al. [19] documented the effects of the power index on bubble columns with non-Newtonian fluids. Unlike the few other works on non-Newtonian bubble columns, Amin documented radial gas velocity and volume fraction profiles for four power law fluids with power indexes ranging from .98 to .21. For this reason, Amin’s work was chosen to be modeled. The characteristics of the fluid chosen to be modeled are listed below:

**Table 7. Amin's Non-Newtonian Rheological Characteristics**

Name	Density ( $\frac{kg}{m^3}$ )	K ( $PA s^n$ )	n	Surface Tension ( $\frac{mN}{m}$ )
CMC	995.65	.32	.68	73.92

The boundary conditions are the same as those listed in Figure 22 but with a diameter of .292 m and a column height of 2.7 m. The liquid height in the experiment is also 1.1 m while the inlet superficial gas velocities tested are  $.0742 \frac{m}{s}$  and  $.1981 \frac{m}{s}$ . The simulation is also run with the same numerical discretization schemes and relaxation factors as the simulation of the Newtonian bubble column in the previous section. The only other alteration to the previous simulation is the rheological model. The power law for non-Newtonian viscosity model in Fluent was used. Below is a comparison between the experimental data Amin et al. obtained and the simulation developed.

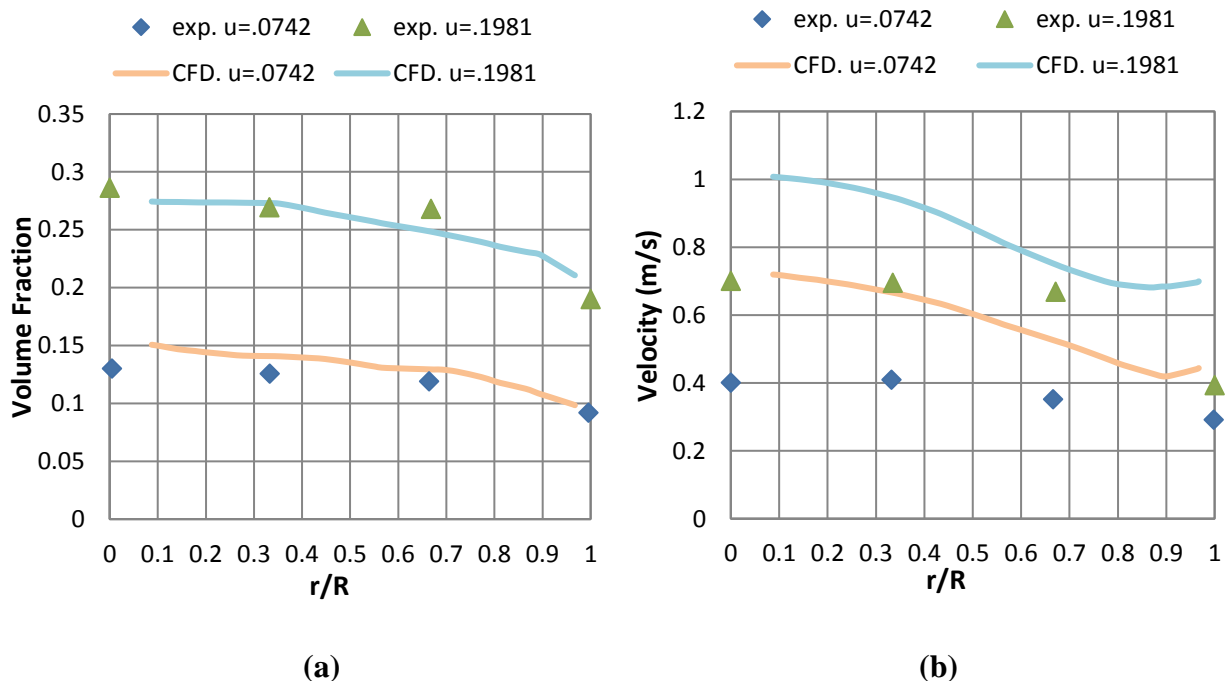
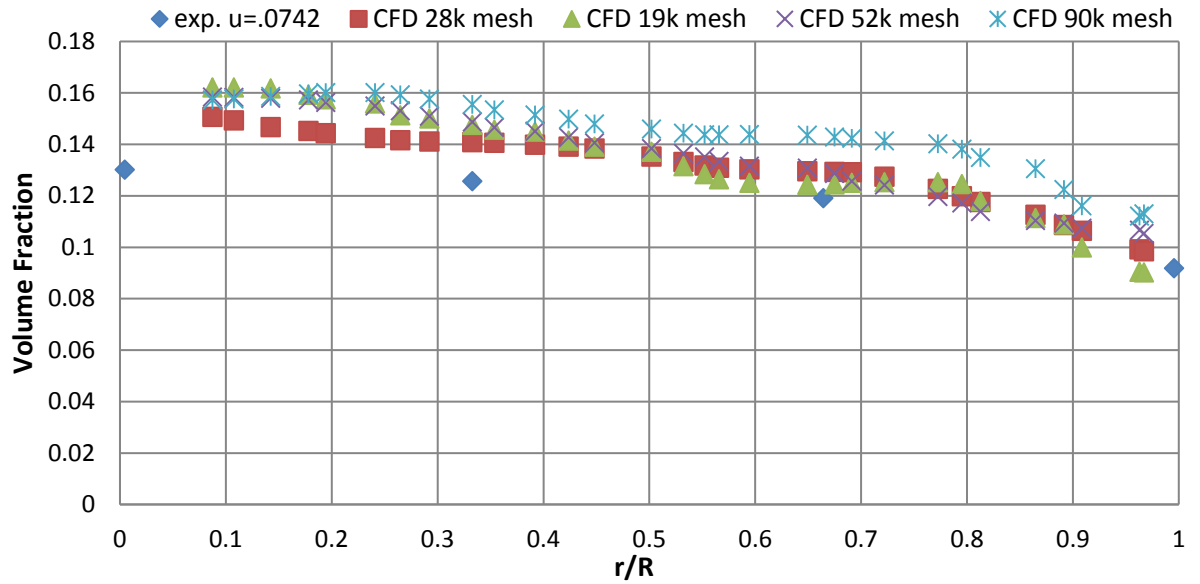


**Figure 25. Circumferentially time averaged (a) air volume fraction and (b) air axial velocity profile simulation results compared to Amin’s experimental data.**

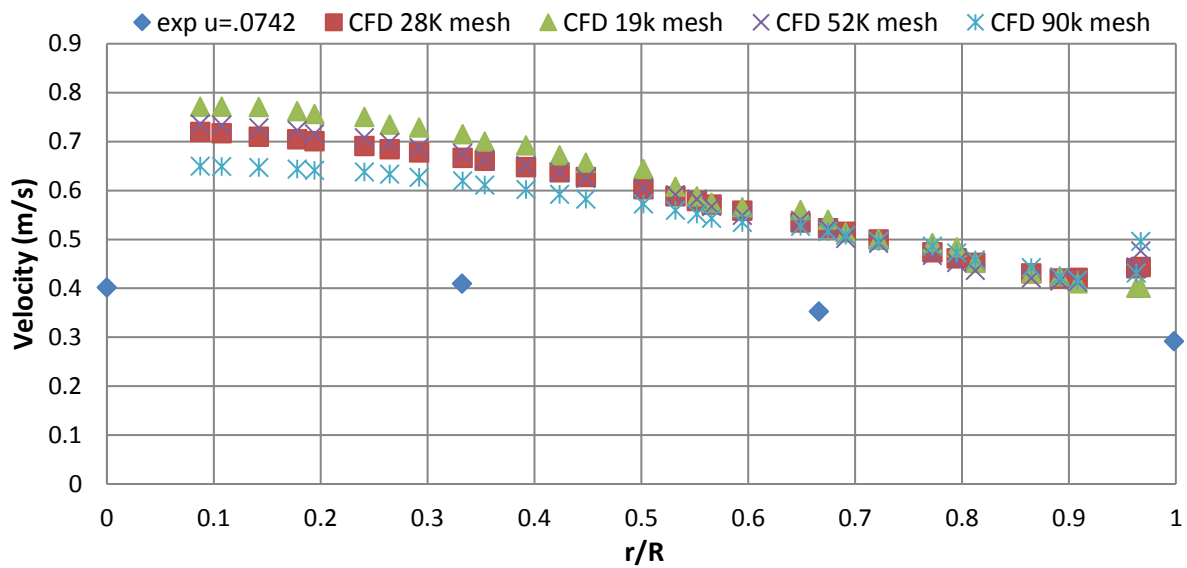
Amin’s experimental data for mean gas volume fraction and mean axial air velocity data extraction are both at a height of 45 cm above the inlet. It is observed in Figure 25 (a) that the volume fraction

profiles predicted by the developed model are in good agreement with Amin’s experimental data. The velocity profile, on the other hand, is over predicted by  $.3 \frac{m}{s}$  for both superficial gas velocities. Other drag and turbulence models were used in order to attempt to remedy the discrepancy but none proved fruitful. The purpose of this study is that of a qualitative investigation. Therefore, the analysis taken hereafter assumes the results to be representative of the flow despite this discrepancy.

Furthermore, grid refinement was conducted in the developed simulation in order to assure stability of the simulation.



(a)



(b)

Figure 26. Developed simulation grid refinement study of the time averaged (a) air volume fraction (b) air axial velocity.

Figure 26 shows that the variability in the simulation results is small with refining mesh, showing a degree of robustness in the simulation. The simulation was also tested for time averaged convergence.

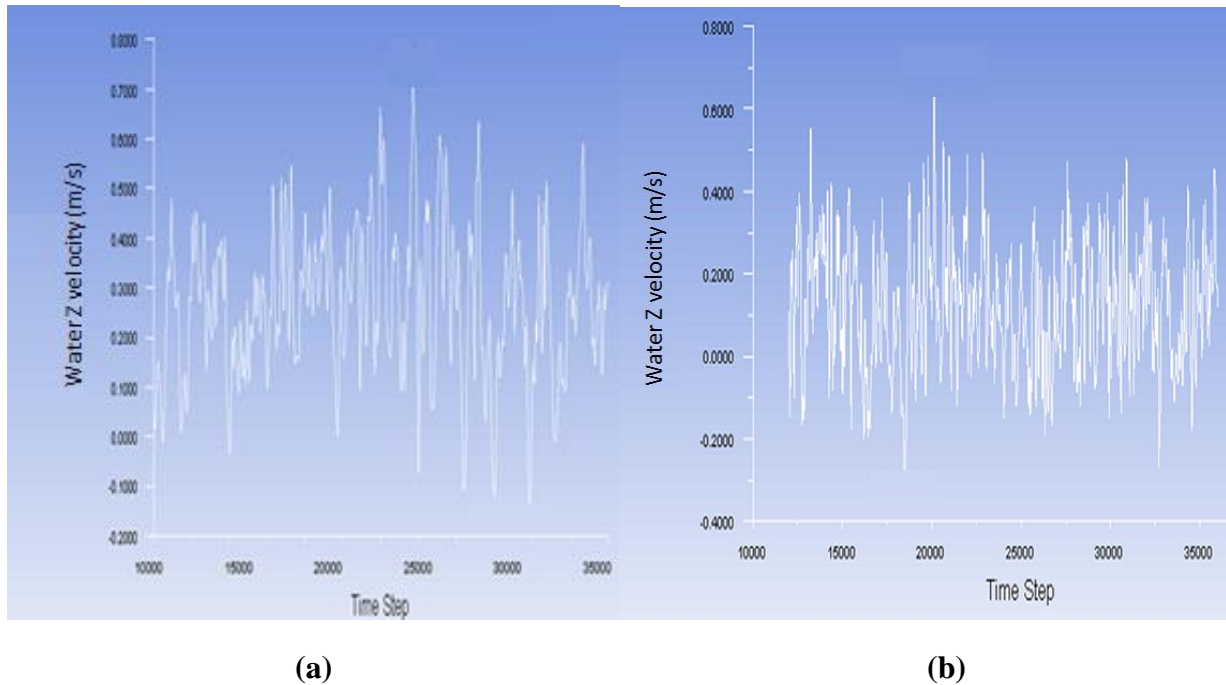


**Figure 27. Instantaneous velocity at the center of the bubble column at a height of (a) 40% of liquid height and (b) 80% of liquid height.**

In Figure 27, the water velocity at a point is observed to fluctuate at a height of (a) 40 % of the liquid height and (b) 80% of the liquid height. The instantaneous water velocity is plotted from 120 seconds to 240 seconds. Although the instantaneous velocity changes with time, there is a general trend of oscillation. The magnitude of oscillation also appears to be transient, but most of the oscillations are near the .5 m/s and .4 m/s mark.

Given that the simulation results 1) qualitatively match Amin's experimental data and are quantitatively within reasonable error, 2) are fairly stable to grid refinements, and 3) are near a quasi-steady state, it is concluded that the simulation can substantiate meaningful qualitative results during a parametric study.

### **Parametric study simulation of bubble column operating with non-Newtonian fluid**

As mentioned previously, there are no studies concerning the effects that  $\frac{H}{D}$  have on the volume fraction and velocity profile of non-Newtonian sparged columns. Particularly, no information on  $\frac{H}{D}$  values as low as those observed in the waste tanks are studied. Thus, the validated simulation will be ran with a varying characteristic ratio number ( $\frac{H}{D} = 5.2 - .34$ ) and study the resulting effects.

### Non-Newtonian $\frac{H}{D}$ Study

The simulation developed was run with an inlet air velocity of  $.1942 \frac{m}{s}$  along with the same diameter of Amin’s et al. experiment. In order to alter the  $\frac{H}{D}$  ratio, the height of the column was changed while the diameter held constant. The distance between the height of the liquid and the outlet pressure boundary condition was kept at a constant of 1.2 m. Like the previous simulations, time averaging was conducted for 30 seconds after waiting 90 seconds for quasi-steady state to be reached. The extraction of data was gathered at 40% and 80% of the liquid height, scaling with the different  $\frac{H}{D}$  ratios. The following results were observed.

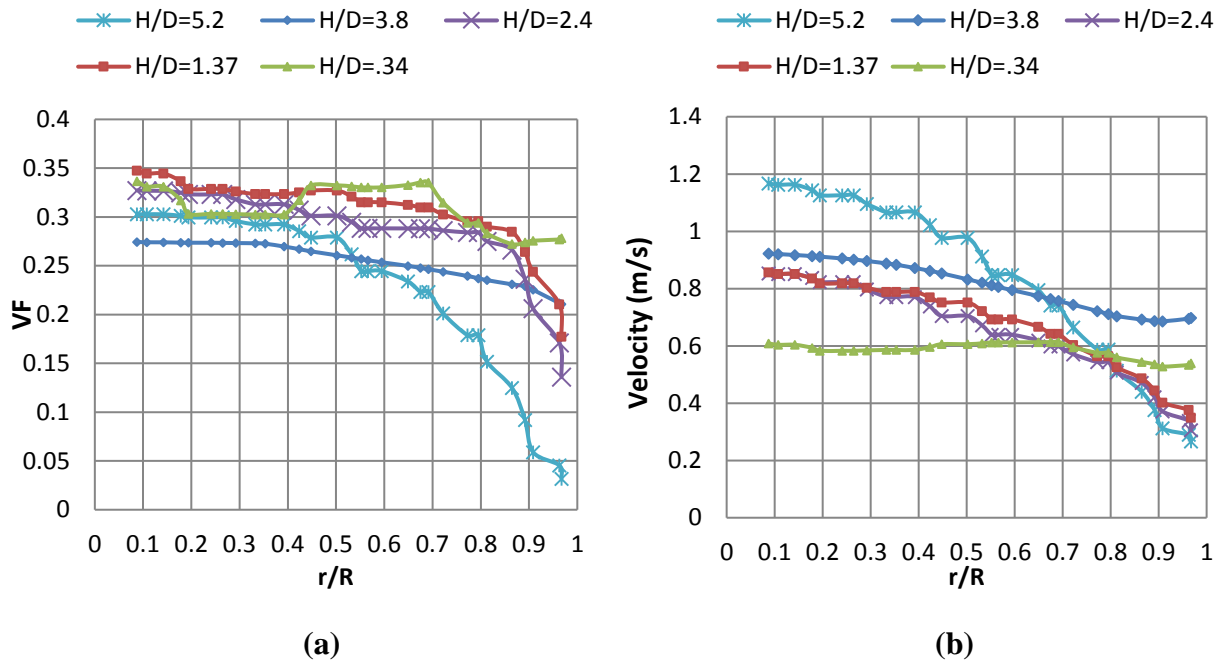


Figure 28.  $H/D$  comparison ( $\frac{H}{D} = 5.2 - .34$ ) of (a) air volume fraction and (b) air axial velocity at 40% of the liquid height.

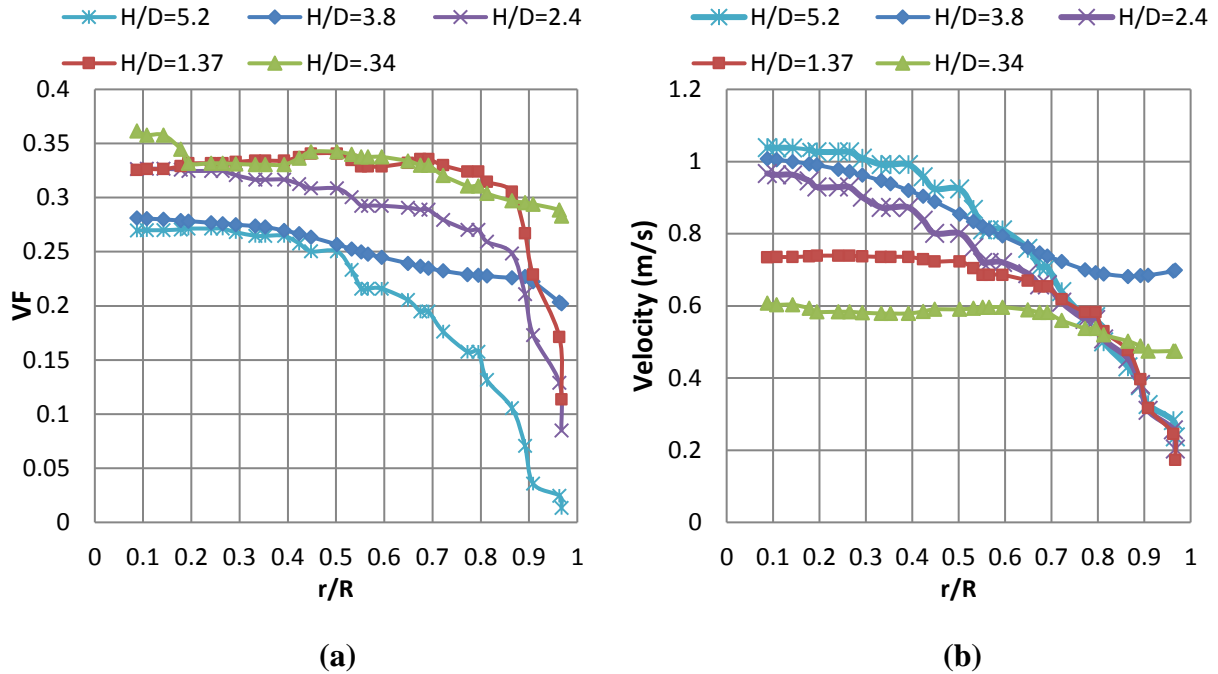


Figure 29. H/D comparison ( $\frac{H}{D} = 5.2-.34$ ) of (a) air volume fraction and (b) air axial velocity at 80% of the liquid height.

From Figure 28 (a), it is observed that the volume fraction profile becomes flatter with decreasing  $\frac{H}{D}$  ratio. At  $\frac{H}{D} = 5.2$ , the most parabolic profile is observed, while at  $\frac{H}{D} = .34$ , the volume fraction is almost flat. A similar trend can be observed in Figure 29 (a). This is due to the fact that as the height of the fluid is reduced, the extraction of data occurs much closer to the inlet. From Figure 30, which shows trends of the air volume fraction profile, evidence is provided for this hypothesis.

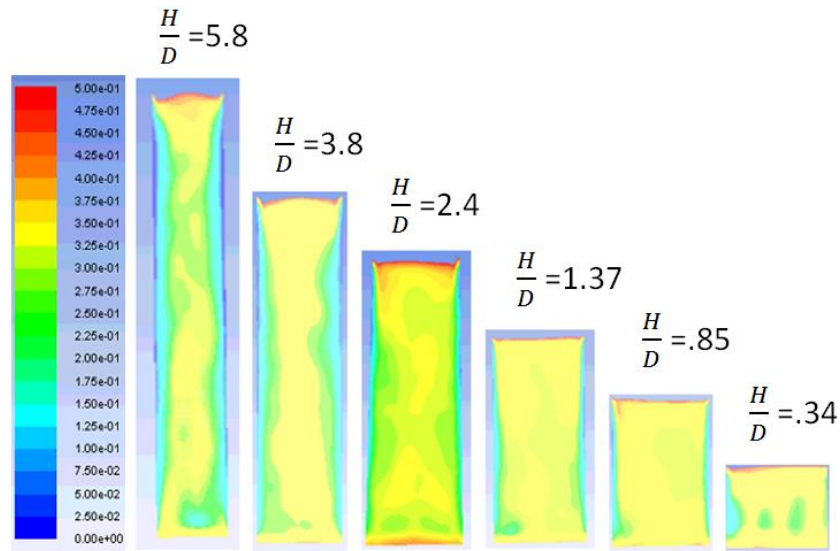


Figure 30. Time averaged air volume fraction profile across a 2D plane for H/D= 5.8-.34 with a clip to range of .5 (not to scale).

It is observed that in all simulations, the air volume fraction near the inlet has a plug profile. Immediately after this plug profile, the volume fraction tends to concentrate itself near the walls. The volume fraction then tends to a developed state where the concentration of air is higher at the center. It is important to note that Figure 30 is time averaged for 30 seconds and that an instantaneous gas volume profile would look entirely different, as the volume fraction plume oscillates from side to side, as shown in previous studies. From this, one can conclude that the volume fraction profile expected in both magnitude and shape are in part a function of where they are extracted in reference to the inlet. This reference distance to the inlet is a percentage of the column diameter, giving significance to the  $\frac{H}{D}$  parameter.

When studying the behavior of the air velocity profile in Figure 28 (b) and Figure 29(b), one can see a similar flattening of the axial air velocity profile with decreasing  $\frac{H}{D}$ . The first noticeable outcome is that the center velocity tends to increase when comparing the same  $\frac{H}{D}$  at 40% liquid height to 80% liquid height. This is due to that fact that the bubbles haven't yet reached terminal upward velocity, so it is expected to see some velocity increase. For this same reason, the velocity tends to be higher with increasing  $\frac{H}{D}$ , since the height of the fluid column is the parameter increasing, giving more time for acceleration to take place.

It was also observed that the behavior near the wall of the air velocity profiles has a noticeable trend. As the velocity profile is given more time to become developed, the effect of the wall is more prominent, giving lower velocities due to the no slip boundary condition at the wall. The noticeable outlier in this trend is the curve formed by  $\frac{H}{D} = 2.4$ .

Lastly, the time averaged volume fraction profiles on a 2D contour surface whose normal is perpendicular to the axial direction was investigated. Below are the time averaged contour plots of air volume fraction.

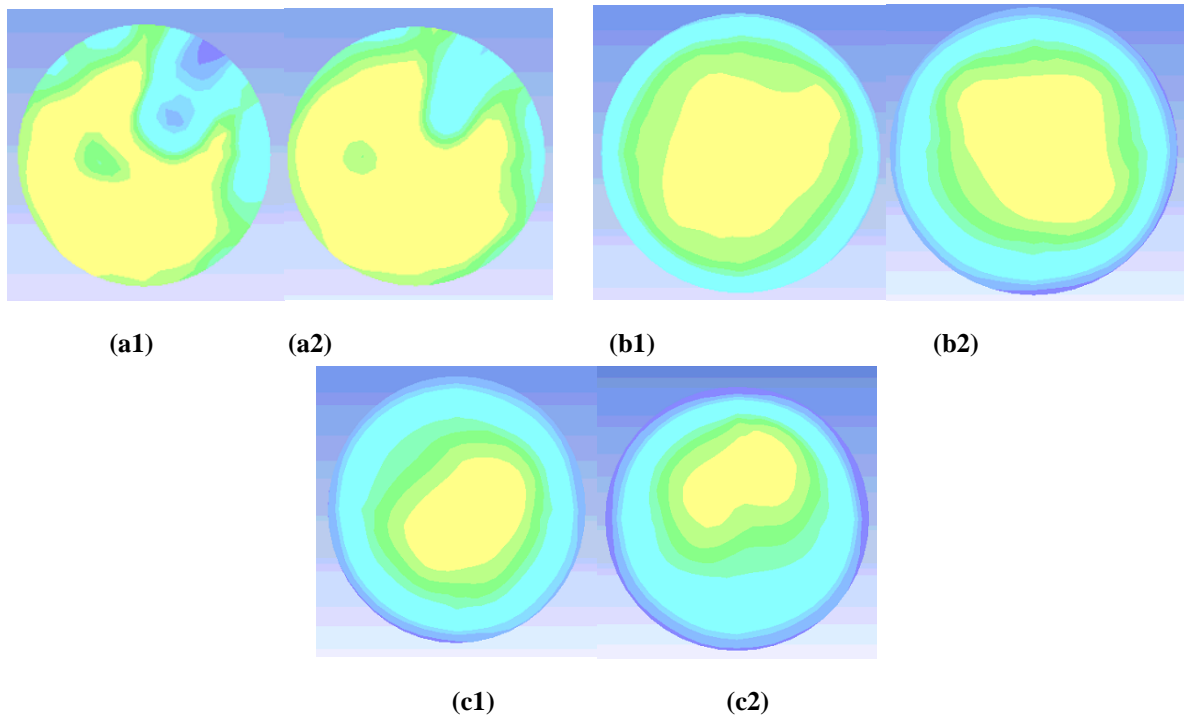


**Figure 31. Time averaged air volume fraction on an axial section view for (a)  $\frac{H}{D} = .34$ , (b)  $\frac{H}{D} = 3.8$ , (c)  $\frac{H}{D} = 5.8$  at (1) 40% and (2) 80% of the liquid height.**

From the simulations, it is shown that there is little difference, from a qualitative point of view, between the time averaged air volume fraction contour plots at 40% and 80% of liquid height. There is a tendency for the volume fraction profile to concentrate near the center and lessen in concentration radially outward until the column wall boundary condition is reached. This behavior is observed in experimental data. In both Figure 31 (a1) and (a2), this tendency is not observed. This could be due to the fact that at a  $\frac{H}{D}$  ratio of .35, the data is extracted too close to the inlet velocity, not giving enough time for wall effects take precedence.

## CONCLUSIONS AND FUTURE WORK

---

The pulse jet mixing process is a vital part of the nuclear waste deactivation and decommissioning mission at the Hanford Site. However, there are a number of areas of uncertainty within the PJM process. This task investigates aspects of the hydrodynamics involved with implementing sparging within the waste tanks.

The effect of the characteristic ratio,  $\frac{H}{D}$ , and power law index on bubble columns with non-Newtonian fluids was investigated. It was observed that a flattening of the profile occurs with decreasing  $\frac{H}{D}$  ratio for both air volume fraction and air axial velocity. This is predicted to be a result of how close the outlet is to the inlet. The wider the diameter of the column through which sparging occurs, the longer vertical distance required for the flow to become fully developed. It is, therefore, expected that if the PJMs were sparged, they would experience a plug air volume fraction and axial velocity profile.

Sparging in the area of non-Newtonian fluids has not been thoroughly investigated. Future work in this area that would be beneficial to the design and development of the PJM process to investigate the effects that altering rheological and physical characteristics of the flow would have on the mixing state of the column. This would directly address the ultimate intent of the PJM process. Furthermore, the synergistic effects on mixing that both sparging and jet impingement has on mixing would be of significant interest.

## REFERENCES

---

1. Chris Guenther , M.S., William Rogers , Sofiane Benyahia , Rahul Garg , Tingwen Li, *TECHNICAL REPORT ON NETL's NON-NEWTONIAN MULTIPHASE SLURRY WORKSHOP* 2013, NETL: Morgan Town, WV. p. 1-65.
2. Poreh, M., Y.G. Tsuei, and J.E. Cermak, *Investigation of a Turbulent Radial Wall Jet*. Journal of Applied Mechanics, 1967. 34(2): p. 457-463.
3. Picardi, R.N., *Numerical Analysis of Multiphase Flow in Bubble Columns and Applications for Microbial Fuel Cells*, in *Mechanical Engineering*. 2015, Virginia Tech: 2015-04-15.
4. Attfield, P.V., *Stress tolerance: the key to effective strains of industrial baker's yeast*. Nature biotechnology, 1997. 15(13): p. 1351-1357.
5. Berovic, M. and M. Legisa, *Citric acid production*. Biotechnology Annual Review, 2007. 13: p. 303-343.
6. Hermann, T., *Industrial production of amino acids by coryneform bacteria*. Journal of biotechnology, 2003. 104(1): p. 155-172.
7. Strik, D.P., et al., *Renewable sustainable biocatalyzed electricity production in a photosynthetic algal microbial fuel cell (PAMFC)*. Applied microbiology and biotechnology, 2008. 81(4): p. 659-668.
8. Kantarci, N., F. Borak, and K.O. Ulgen, *Bubble column reactors*. Process Biochemistry, 2005. 40(7): p. 2263-2283.
9. Hekmat, A., A.E. Amooghin, and M.K. Moraveji, *CFD simulation of gas-liquid flow behaviour in an air-lift reactor: determination of the optimum distance of the draft tube*. Simulation Modelling Practice and Theory, 2010. 18(7): p. 927-945.
10. Rampure, M.R., V.V. Buwa, and V.V. Ranade, *Modelling of Gas-Liquid/Gas-Liquid-Solid Flows in Bubble Columns: Experiments and CFD Simulations*. The Canadian Journal of Chemical Engineering, 2003. 81(3-4): p. 692-706.
11. Becker, S., A. Sokolichin, and G. Eigenberger, *Gas-liquid flow in bubble columns and loop reactors: Part II. Comparison of detailed experiments and flow simulations*. Chemical Engineering Science, 1994. 49(24): p. 5747-5762.
12. Pflieger, D., et al., *Hydrodynamic simulations of laboratory scale bubble columns fundamental studies of the Eulerian-Eulerian modelling approach*. Chemical Engineering Science, 1999. 54(21): p. 5091-5099.
13. Pan, Y., M.P. Dudukovic, and M. Chang, *Numerical investigation of gas-driven flow in 2-D bubble columns*. AIChE Journal, 2000. 46(3): p. 434-449.
14. Yakhot, V., et al., *Development of turbulence models for shear flows by a double expansion technique*. Physics of Fluids A: Fluid Dynamics, 1992. 4(7): p. 1510-1520.
15. Buwa, V.V. and V.V. Ranade, *Dynamics of gas-liquid flow in a rectangular bubble column: experiments and single/multi-group CFD simulations*. Chemical Engineering Science, 2002. 57(22): p. 4715-4736.
16. Chen, W., et al., *Scale-up effects on the time-averaged and dynamic behavior in bubble column reactors*. Chemical engineering science, 2001. 56(21): p. 6149-6155.
17. Rampure, M.R., A.A. Kulkarni, and V.V. Ranade, *Hydrodynamics of Bubble Column Reactors at High Gas Velocity: Experiments and Computational Fluid Dynamics (CFD) Simulations*. Industrial & Engineering Chemistry Research, 2007. 46(25): p. 8431-8447.

18. McClure, D.D., et al., *Development of a CFD model of bubble column bioreactors: part one—a detailed experimental study*. Chemical Engineering & Technology, 2013. 36(12): p. 2065-2070.
19. Esmaeili, A., C. Guy, and J. Chaouki, *The effects of liquid phase rheology on the hydrodynamics of a gas–liquid bubble column reactor*. Chemical Engineering Science, 2015. 129: p. 193-207.
20. Plais, C. and F. Augier, *Effect of liquid viscosity on mixing times in bubble columns*. Theoretical Foundations of Chemical Engineering, 2016. 50(6): p. 969-974.
21. Kawase, Y. and M. Moo-Young, *Hydrodynamics in bubble column bioreactors with fermentation broths having a yield stress*. Applied Microbiology and Biotechnology, 1989. 30(6): p. 596-603.
22. Terasaka, K., et al., *Oxygen transfer into xanthan solutions in partitioned bubble columns*. Journal of chemical engineering of Japan, 2013. 46(1): p. 33-39.
23. McClure, D.D., et al., *Development of a CFD model of bubble column bioreactors: part two—comparison of experimental data and CFD predictions*. Chemical Engineering & Technology, 2014. 37(1): p. 131-140.
24. Xu, L., et al., *Application of population balance model in the simulation of slurry bubble column*. Industrial & Engineering Chemistry Research, 2014. 53(12): p. 4922-4930.
25. Fluent, *Theory Guide*, in *Multiphase Flow*.
26. Fluent, *Users Manual*, in *Multiphase Flow*.
27. Sokolichin, A. and G. Eigenberger, *Applicability of the standard  $k$ - $\epsilon$  turbulence model to the dynamic simulation of bubble columns: Part I. Detailed numerical simulations*. Chemical Engineering Science, 1999. 54(13-14): p. 2273-2284.
28. Xu, L., et al., *Numerical simulation of bubble column flows in churn-turbulent regime: comparison of bubble size models*. Industrial & Engineering Chemistry Research, 2013. 52(20): p. 6794-6802.
29. Laborde-Boutet, C., et al., *CFD simulation of bubble column flows: Investigations on turbulence models in RANS approach*. Chemical Engineering Science, 2009. 64(21): p. 4399-4413.
30. Chen, J., et al., *Fluid dynamic parameters in bubble columns with internals*. Chemical Engineering Science, 1999. 54(13): p. 2187-2197.
31. McClure, D.D., et al., *Mixing in bubble column reactors: experimental study and CFD modeling*. Chemical Engineering Journal, 2015. 264: p. 291-301.

## **TASK 18.2**

# **DEVELOPMENT OF INSPECTION TOOLS FOR DST PRIMARY TANKS (FIU YEAR 7)**

### **EXECUTIVE SUMMARY**

---

In August of 2012, traces of waste were found in the annulus of the AY-102 double-shell tank (DST) storing radioactive waste at the Hanford Site, prompting the need for developing inspection tools that can identify the cause and location of the leak. To help in this effort, FIU is investigating the development of inspection tools able to access the tank's secondary containment, while providing live visual feedback. This effort has led to the development of two inspection tools: a magnetic wheeled miniature motorized rover that will travel through the refractory cooling channels under the primary tank, and a pneumatic pipe crawler that will inspect the tank ventilation header piping. Both inspection routes lead to the central plenum under the primary tank.

The magnetic wheeled miniature tool is a remote controlled rover with four wheels directly driven by independent micro DC motors. It is equipped with a camera to provide live visual feedback of the inspection tasks. To avoid debris, the device will travel upside down magnetically attached to the bottom of the primary tank. A generic sensor hood is designed to allow different sensors to be integrated via a common hardware interface. The miniature tool is tethered to provide both the power and communication links to and from the operator, and its operation is automated depending on the tether tension. To reduce operational fatigue, a semi-autonomous control is incorporated to assist the operator in steering the miniature tool during inspection.

Preliminary system testing for the inspection tool has been carried out at the full-scale sectional mock-up facility built in-house. This included assessing the camera's visual feedback, the inspection tool's pull-force, data collected via the integrated sensors, and tether management during operation. Further design modifications and performance enhancement efforts are currently underway, and FIU has received significant feedback from WRPS engineers on the necessary modifications.

FIU has also continued to test and improve the pneumatic pipe crawler developed for inspection of 3- and 4-inch pipelines. The pneumatic pipe crawler is a worm type robot with a modular design, composed of interchangeable cylindrical modules connected with flexible links. The primary improvement includes the integration of sensors, with the objective of enhancing the inspection tool capabilities, robustness and operational feedback. The integration of the following sensors are being considered: (a) a thermal infrared camera to provide thermal image mapping, hot spot detection and temperature gradient analysis; (b) ambient temperature, pressure and humidity sensors to provide environmental conditions; (c) a wall scanner module to provide radiation, ultrasound, and visual surface mapping; (d) a load cell to provide tether drag estimation; (e) contact pressure sensors to provide grip conditions; and (f) inclinometers to provide slope and orientation of each module of the crawler.

A full scale sectional mockup of the DST floor has been designed and is being manufactured at FIU. The mockup is an 8 ft swath, approximately 40 ft in length that includes the two liners, the annulus, the drain slots and refractory channels. The mockup will be used to demonstrate FIU's

systems and can also be used to evaluate future inspection technologies, sensors and robotic devices in operational conditions equivalent to those at Hanford.

## INTRODUCTION

In August of 2012, traces of waste were found in the annulus of the AY-102 double-shell tank storing radioactive waste at the Hanford Site, prompting the need for developing inspection tools that can identify the cause and location of the leak.

Figure 32 shows three possible entry points for inspection in the AY-102 double-shell tank:

1. the refractory air slots through the annulus,
2. the leak detection piping, and
3. the ventilation header piping.

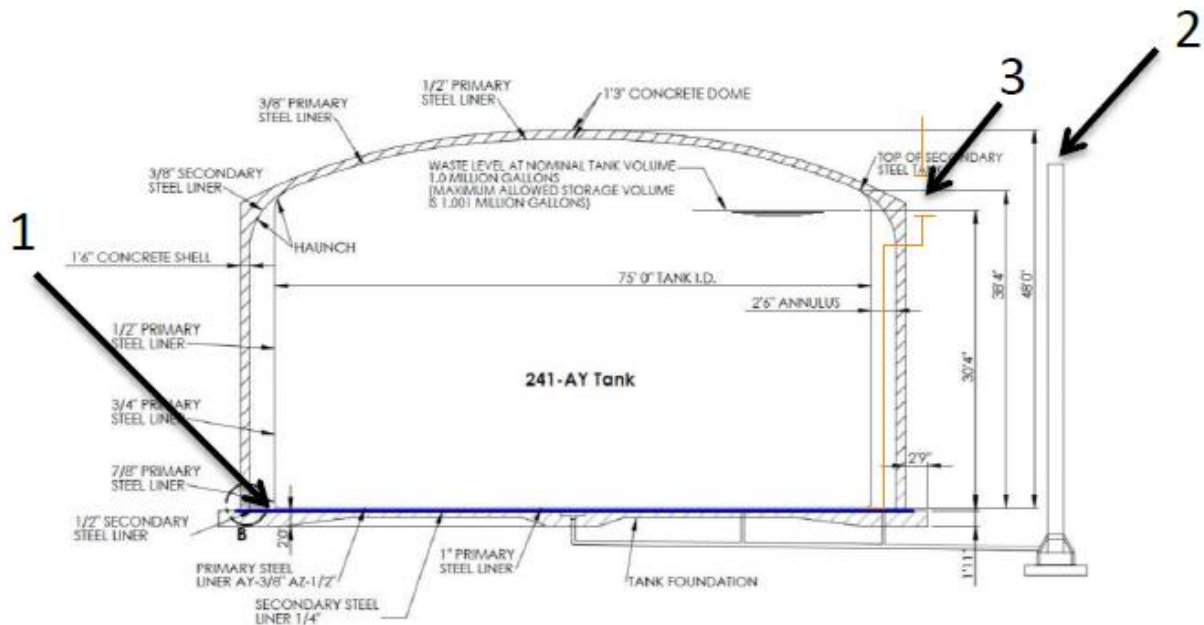


**Figure 32. Inspection entry points of the AY-102 double-shell tank.**

To assist in this effort, FIU is investigating the development of inspection tools able to access the tank secondary containment, while providing live visual feedback. The effort led to the development of two inspection tools:

- a *magnetic miniature rover* that will travel through the refractory air slots, and
- a *pneumatic pipe crawler* that will inspect the ventilation header piping.

The objective of this task is to develop inspection tools that will assist site engineers at Hanford in understanding the health of the DSTs, including the primary and secondary liners.

## MAGNETIC MINIATURE ROVER

### Background

FIU is developing a technology that will access the primary tank floor of DSTs at Hanford through the annulus and refractory air slots (Figure 33) and provide visual feedback of the condition within the air slots. The refractory air slots range from 1 inch to 3 inches in width and provide a complex maze to navigate through, including four 90° turns to reach the center of the tank (Figure 34). Pictured is documentation on AY-102, a tank possessing one of the more difficult inspection paths due to the layout of the refractory cooling channels; other double-shell tanks contain channels whose layouts resembles a web structure with much larger angles at the turns rather than the sharp 90° turns (Figure 35).

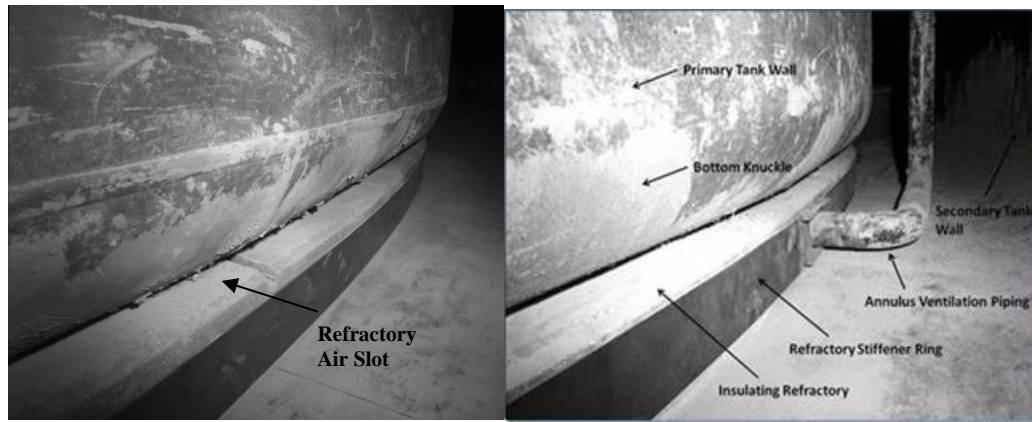


Figure 33. Side view of primary tank and refractory air slot.

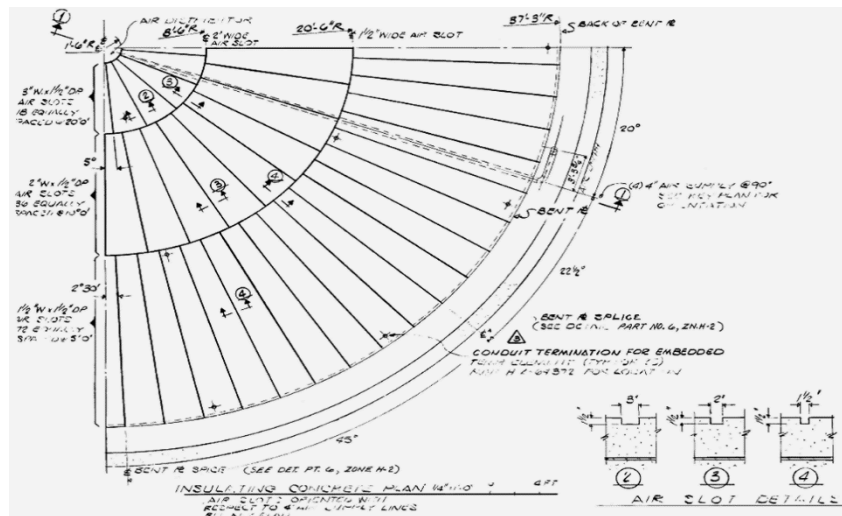
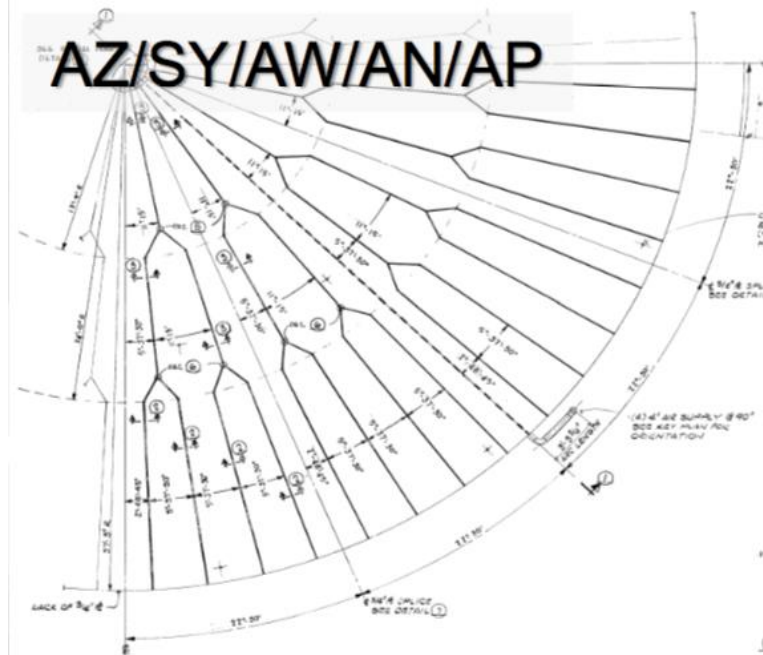


Figure 34. Refractory air slot layout and description for AY-102.



**Figure 35. Refractory slot layout for Tank type AZ, SY, AW, AN and AP.**

During this past year, redesigns of the inspection tool were carried out in order to improve the visual feedback quality, increase the pull force, improve the overall functionality of the inspection tool, and facilitate integration of various environmental and radiation sensors.

Patch LEDs were used to replace the standard bulb LEDs and tests were conducted to investigate the number of patch LEDs needed to provide an adequate amount of illumination. Instead of 2 bulb-LED lights that were used for the previous design, 4 patch-LEDs are being used for the new design (Figure 36). The new design not only increases the amount of light, which is essential for providing better image quality, but also re-positions both the camera and LED light locations to make room for sensor integration on the hood of the inspection tool.

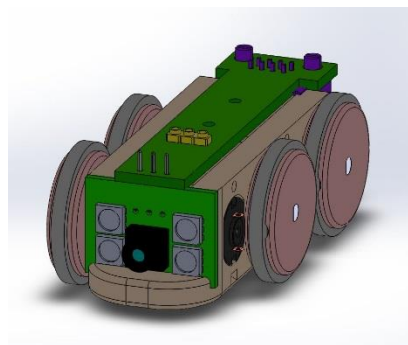


**Figure 36. The redesigned inspection tool without the hood. Both the camera and the LED lights are connected perpendicularly to the base-PCB. Three extra connector-pins (yellow) are added on the base-PCB to provide connections to the sensors.**

A space for an extra magnet was also added at the front of the unit. This was done in order to increase the unit’s magnetic pull-force with the metallic surface. The increase in the magnetic pull-force between the unit and the surface also results in an increase of the overall traction of the

inspection tool. This is important to ensure that the inspection tool is able to overcome the friction of the tether.

### Sensor integration conceptual designs

Work also began on the conceptual design to integrate sensors into the inspection tool. The sensors considered include temperature, infrared, and ultra-sonic (UT) sensors. The first conceptual design integrated a one-wire temperature sensor (Maxim DS18B20), as shown in Figure 37. The hood, which was previously used just for covering the base printed circuit board (PCB), will now house the actual sensors. The conceptual design promotes interchangeability where hoods with different sensors can be fabricated and exchanged on the inspection tool for different inspection objectives.

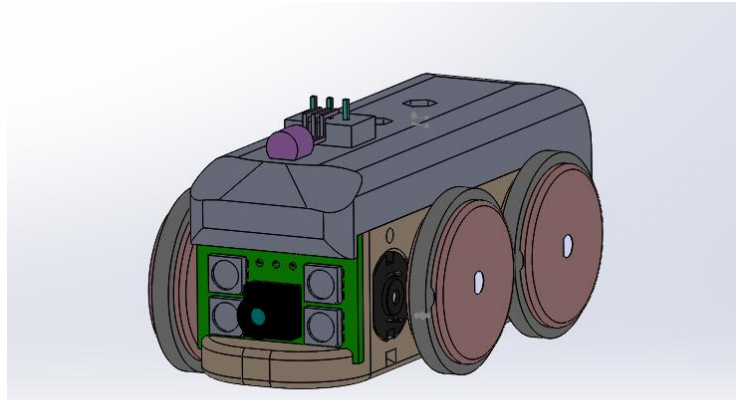


**Figure 37. Initial conceptual design with a temperature sensor attached (purple) to the top of the inspection tool. The design also includes a patch-LED inserted on the front PCB, replacing the bulb LED.**

Three sensors for the inspection tool were received, including a temperature sensor (Maxim DS18B20), a temperature and humidity sensor (Maxim DS1923), and a radiation sensor (Teviso RD2014). Before system integration, the sensors were tested to ensure they were functioning correctly. These tests included the wiring (with necessary supporting electronic components like the resistors and capacitors), system powering and sensor driver programming. For the radiation sensor, a Cs-137 source was used to ensure that it correctly registers the radiation count. All of the sensors are functioning as expected and are ready to be integrated with the sensor drivers into the final system. The results from the sensor testing helped in designing the sensor PCBs that will be attached on top of the mini inspection tool.

The individual PCBs' location within the mini inspection tool is shown in Figure 38. The base PCB carries the power for the motor control, as well as providing communication for both the sensor and camera PCBs. The base PCB provides a common three-pin connector for different sensor PCBs to be attached. This design allows for different sensor PCBs to be designed and fabricated for different sensors, without any modification to the base PCB, thus, providing a generic interface for different sensor integration and expansion. The camera PCB houses both the camera and the LED light source.

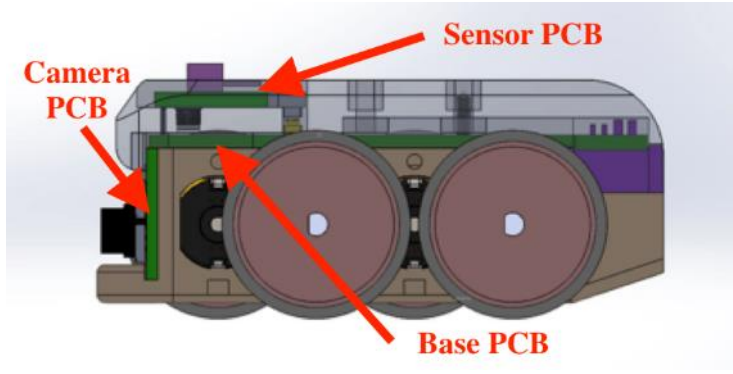


Figure 38. CAD drawing showing various PCBs for the electronic components.

Details of the sensors that are currently being considered are shown in the table below.

Table 8. Potential Sensors for Integration

Sensors Types	Sensors	Communication	Descriptions
Temperature (Maxim DS18B20)		One-Wire	Ambient temperature sensor
Temperature and humidity (Maxim DS1923)		One-Wire	Ambient temperature and humidity sensor
Radiation (Teviso RD2014)		TTL	Beta, gamma, x-rays sensor
Infra-red non-contact temperature sensor (CMCIEL mTS017)		One-Wire	Non-contact Infra-red temperature sensor

The finalized conceptual designs for the integration of sensors described in the previous table are shown below.

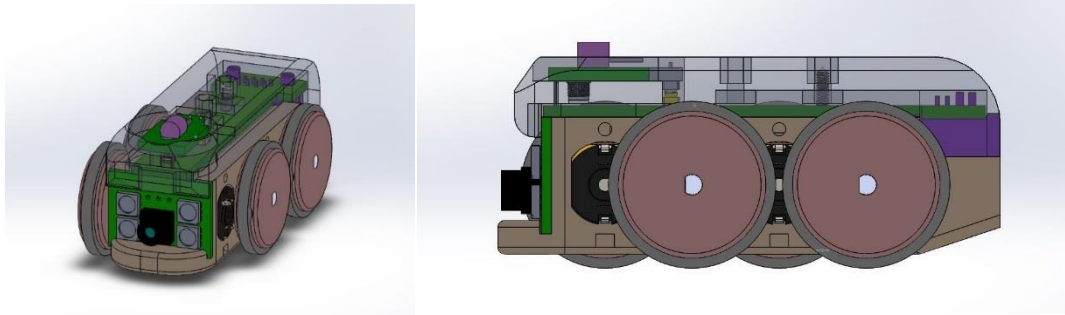


**Figure 39. Conceptual design of temperature sensor integration for measuring the ambient temperature.**

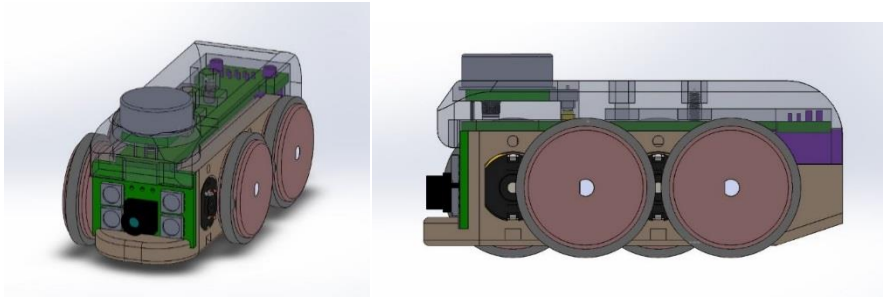


**Figure 40. Conceptual design of iButton integration for measuring both the ambient temperature and humidity.**

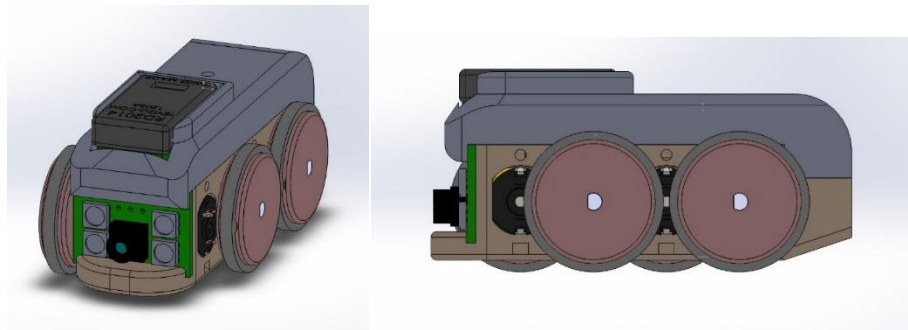


**Figure 41. Conceptual design of radiation sensor integration for measuring beta, gamma and x-rays.**

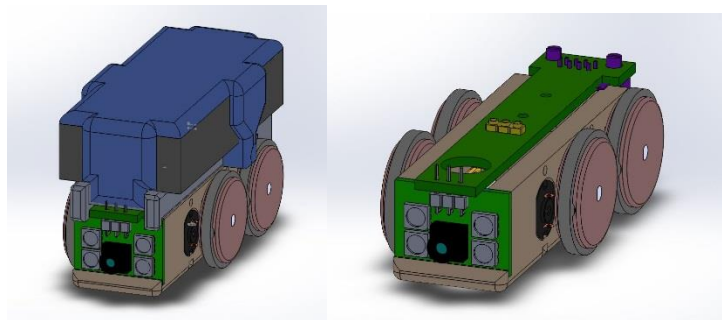


**Figure 42. Conceptual design of non-contact infrared temperature sensor for measuring the surface temperature of the tank bottom. The circular cutout (on right) through the inspection tool's body allows the IR sensing element to be fitted to measure the surface temperature of the tank.**

### Printed Circuit Board (PCB) designs

The PCBs for the base, camera and sensors were designed to accommodate the respective electronic components and provide the power and communication links to the mini inspection tool, as shown in Figure 43. The addition of the PCB will reduce wire clutter and therefore help to reduce the noise experienced by the camera. This redesign also removes tension from the wires while the inspection tool is in operation. Instead, the tension is directed to the PCB, which will be fastened to the body of the inspection tool. The differences between the old and the new design with the PCB are illustrated in Figure 44.

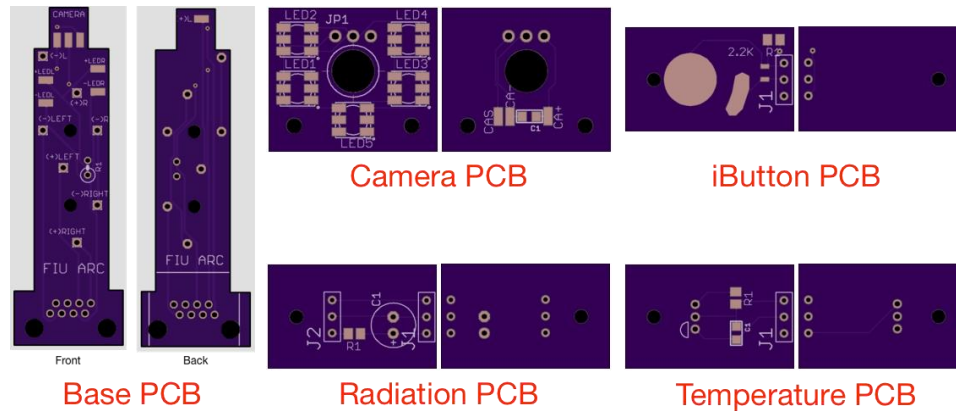


Figure 43. Base, Camera and Sensors PCB designs.

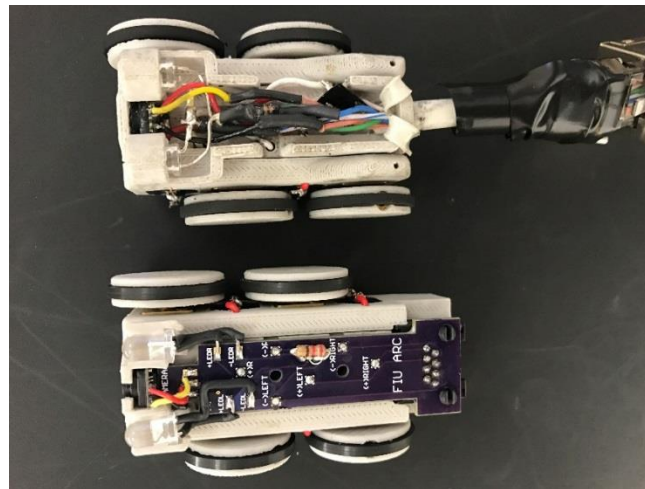


Figure 44. Old inspection tool with wire cluttering issue (top) and new inspection tool with custom-made PCB (bottom).

### Fabrication and system integration

The CAD drawings and the PCBs of the conceptual designs were sent for fabrication. System integration efforts were carried out after they were received. These included population of the electronic components on the PCBs and overall functionality testing of the populated PCBs. Figure 45-left shows the two sensor hoops that are populated with both the temperature and iButton (temperature and humidity) sensors. The sensor hoop has a generic hardware interface with the base-PCB, such that different sensor hoods can be interchanged when needed. Figure 45-right

shows the populated camera PCBs. Two designs with different LED light configurations are currently being tested to determine the optimum lighting required for the camera in the refractory slots. The first design uses all patch LEDs, which provide good localized lighting, while the second design mixes both the patch and bulb LED lights, with the hope of providing both localized and distance lighting.



**Figure 45. (left) Sensor hoods populated with both the temperature and iButton sensors (left) and populated camera PCBs with both the patch and mixed LED lights for the lighting source of the mini inspection tool (right).**

Two fully integrated mini-inspection tools fitted with radiation, temperature and humidity sensor hoods are shown in Figure 46. Unfortunately, due to the lack of availability of the IR non-contact temperature sensor, the conceptual design with the IR sensor shown in Figure 42 was not fabricated.



**Figure 46. Temperature sensor hood (left), inspection tool fitted with iButton humidity and temperature sensor (middle), and inspection tool fitted with RD2014 radiation sensor (right). The sensor hoods share common electrical and communication interfaces.**

## Controller and controller box

A waterproof controller box was designed and fabricated to house all of the electronic components that interface with the inspection tool and the operator. The components include a single board computer (SBC), an analog video capture card, a voltage converter and a motor controller. With all of the components packed in a single enclosure, it would allow plug-and-go capability so that

field-testing can be conducted more efficiently and reduce the turn-around time. The component placement layout would also provide crucial information for a future version where miniaturization may be desired so that it could be attached on top of the delivery platform. Figure 47 shows the schematic drawing as well as the assembled box in the testing stage. An Xbox controller (Figure 48) was also integrated to the controller box so that the operator has the option of controlling both the mini inspection tool and the cable management system manually, when desired. The joystick on the left of the controller is programmed to control the inspection tool’s movement, while the buttons were programmed to control the cable management system’s release and retrieval. In contrast with a keyboard, the addition of the controller made controlling the inspection tool and the cable management system more intuitive and effortless.

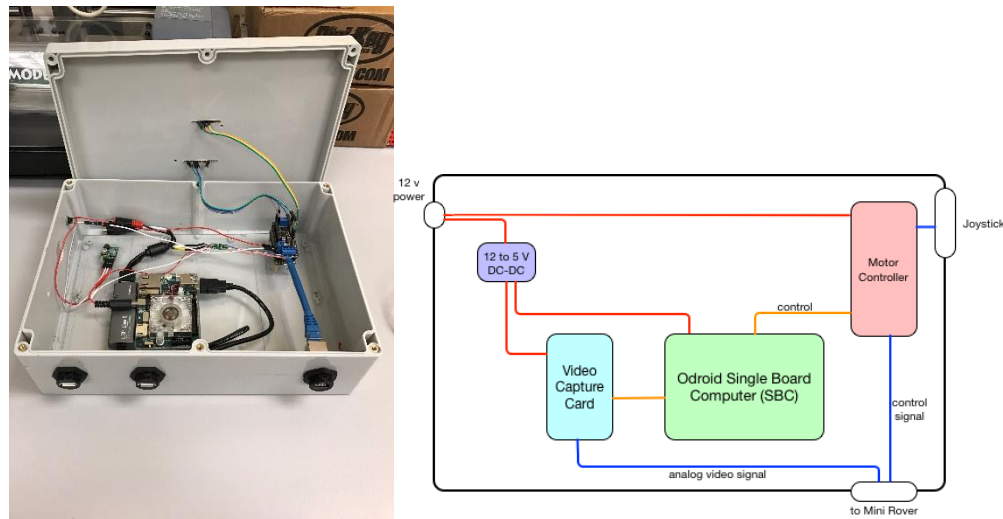


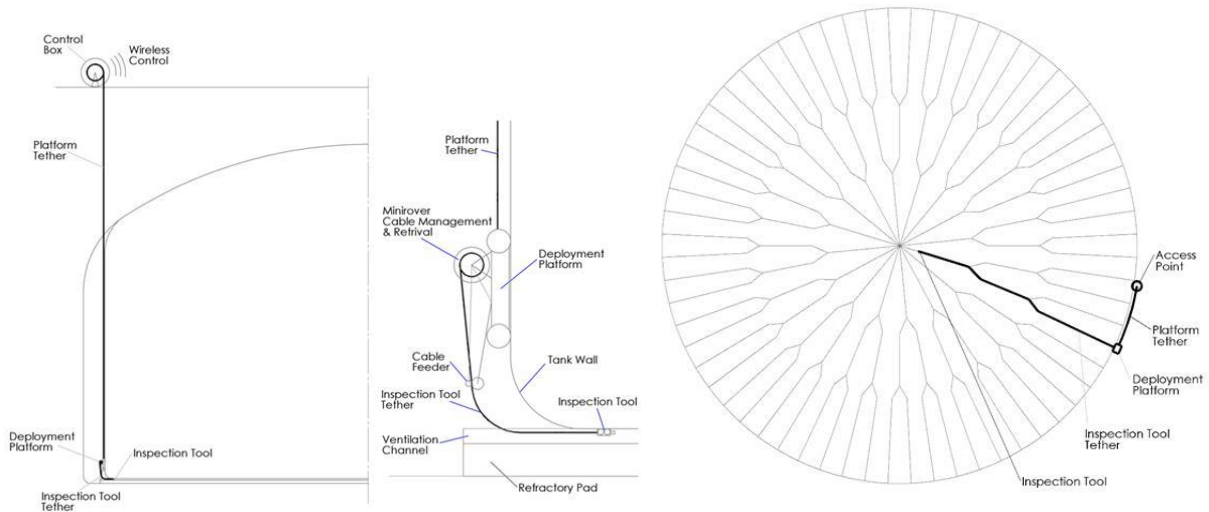
**Figure 47. Waterproof controller box housing all the electronic components that interface with the inspection tool and operator (left) and box diagram showing the layout of the controller box (right).**



**Figure 48. Xbox controller attached to the controller box to provide the operator with the option of controlling both the mini inspection tool and the cable management system manually.**

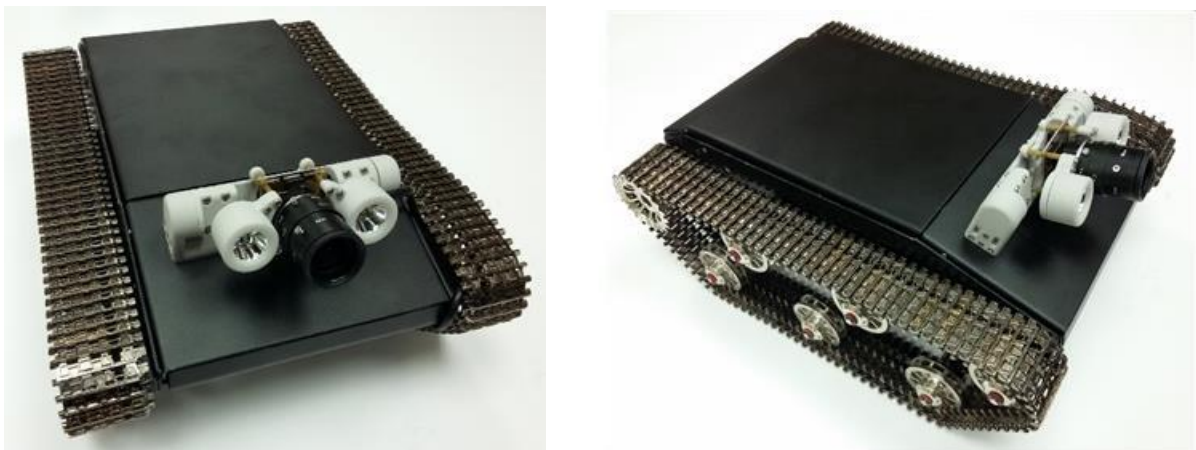
### Cable management system

FIU has been working on designing an automated deployment system suitable for the miniature rover. Figure 49 shows a full-scale illustration of the proposed inspection of the ventilation channel at the bottom of the double shell tanks. During inspection, the miniature tool will drive from a large deployment platform responsible for providing power, control and communication. The parent platform will manage the tool’s tether and retrieve the unit in case of a failure. The platform is being designed to be potentially autonomously driven.



**Figure 49. Ventilation channel proposed inspection.**

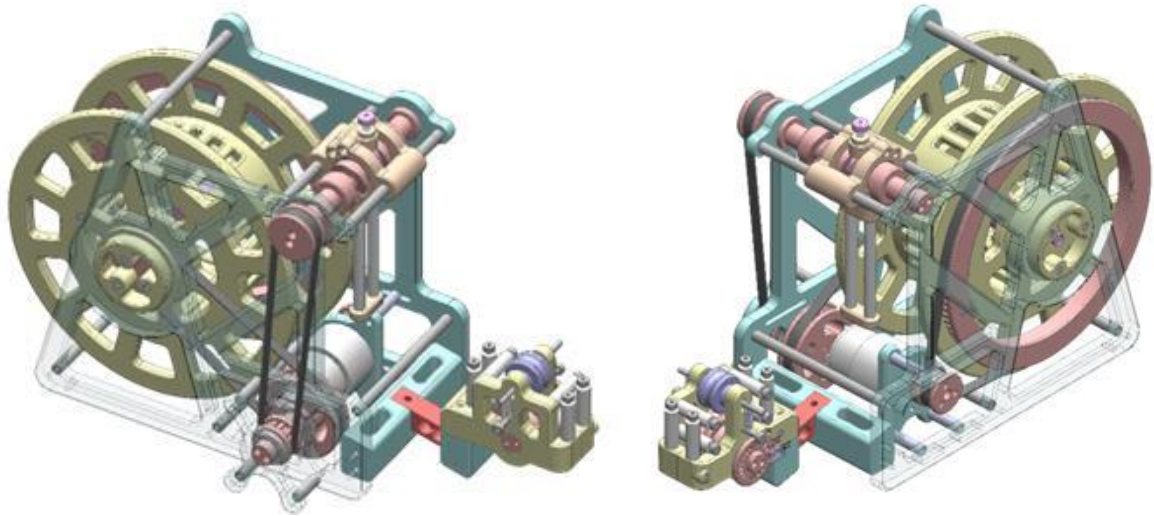
The automated cable management system is necessary to provide a tangle-free means of storing and supplying the tether for the inspection tool. The device is portable and designed to be easily integrated with a small wall crawler, such as the robotic platform currently being developed at FIU, shown in Figure 50. This multi-purpose all-terrain platform has been re-engineered to deploy the miniature inspection tool.



**Figure 50. FIU's robotic platform.**

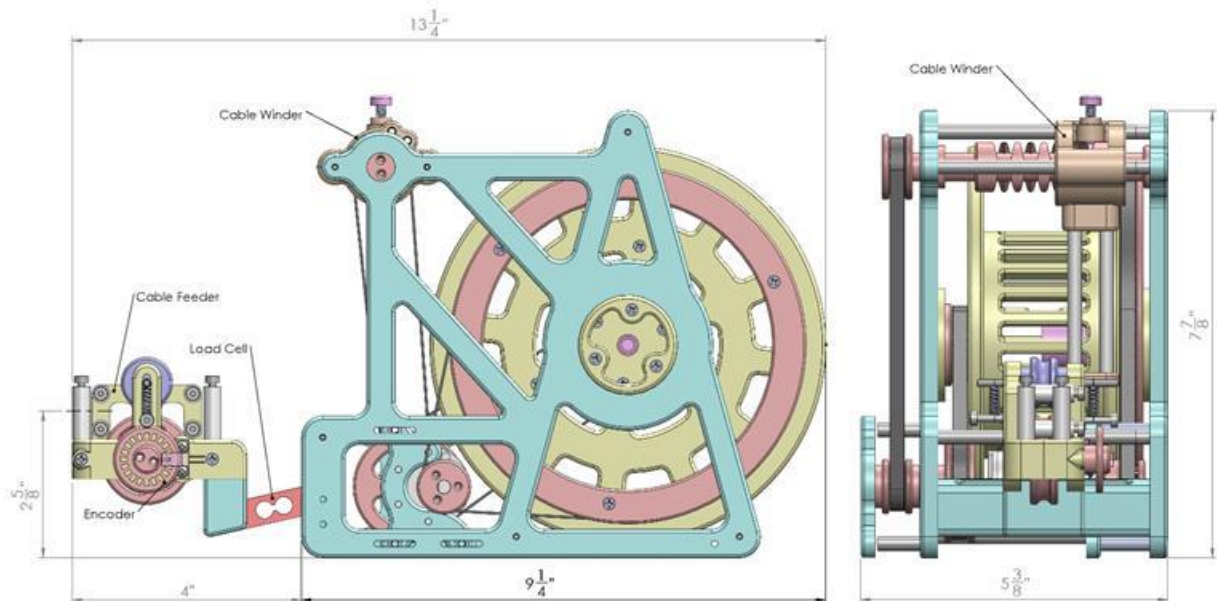
Several reel mechanisms were investigated for tether handling. Figure 51 shows the developed cable management system. There are plans to scale up the cable reel system and use it for the

pneumatic pipe crawler, as well as for the deployment of other inspections tools currently being developed at FIU.



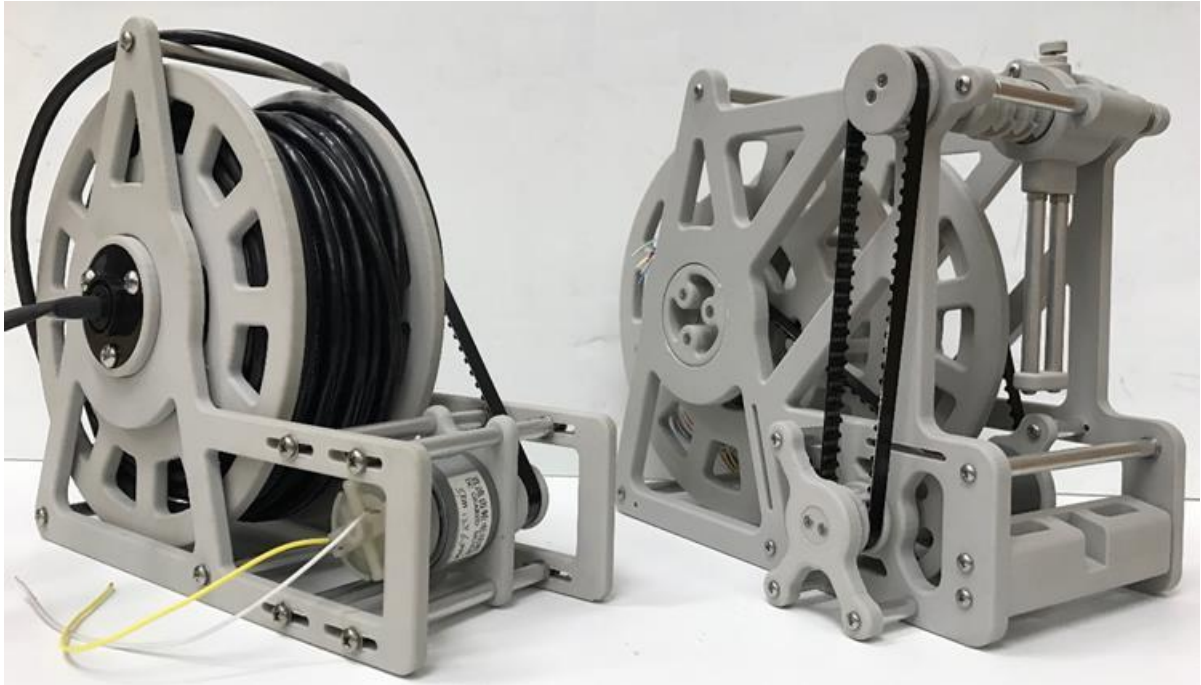
**Figure 51. Automated cable management systems.**

The cable management system consists of a self-layering spool guide to keep the cable reel neat, tidy, and protected from damage. A load cell senses the movement of the inspection tool and a mechanism slides back and forth in sync with the spool wind so that the reel is always properly wound. The system is completely automated and designed to retrieve the tool in case of failure. An automated cable management system is important to contain eventual contamination and prevent radiation spread. Figure 52 shows the overall dimensions of the device.



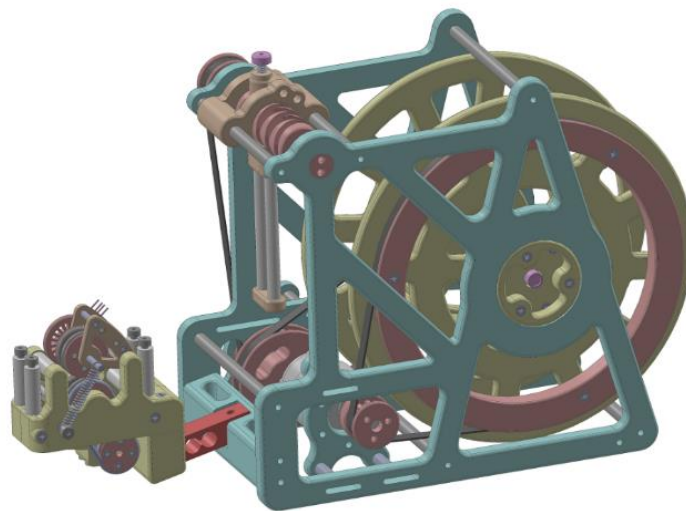
**Figure 52. Automated cable management system dimensions.**

Figure 53 shows the two original prototypes successfully tested at FIU. The design has been in continuous improvement and new features have been incorporated as needed in response to the tests.



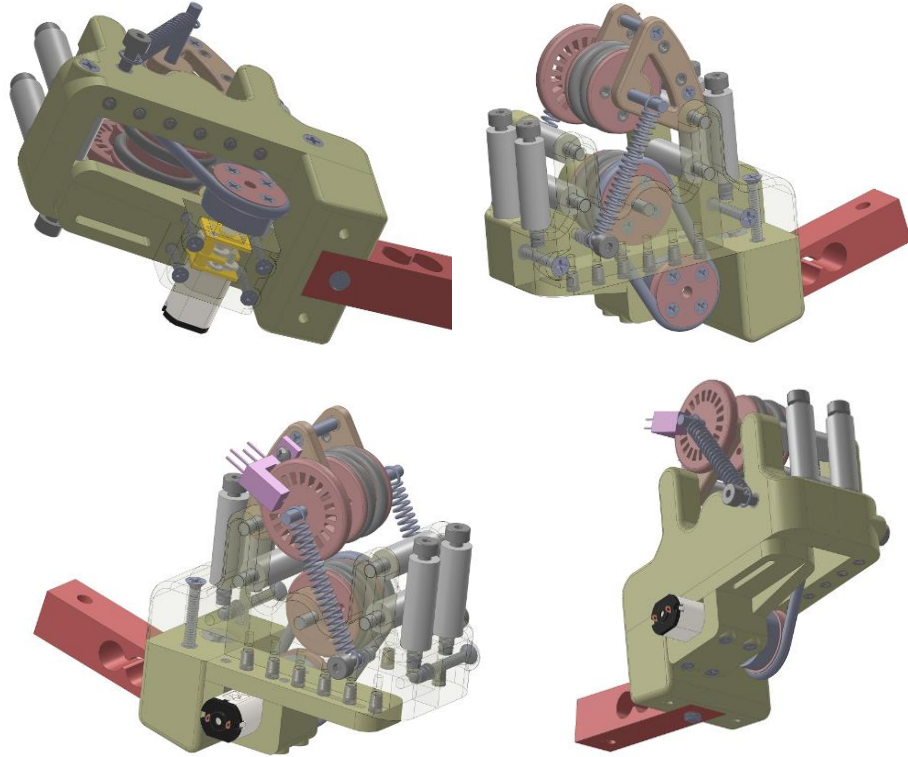
**Figure 53. Original cable management (left) and redesign prototype with winder (right).**

The most recently incorporated improvement was the addition of an active cable feeding capability on the system. Since the mini-inspection tool has limited pull force when navigating in the air refractory, this capability makes use of a strain gauge to sense the tension on the cable and actively releases the cable as needed to minimize the cable tension. Figure 54 shows the cable management system equipped with the active cable feeding capability.



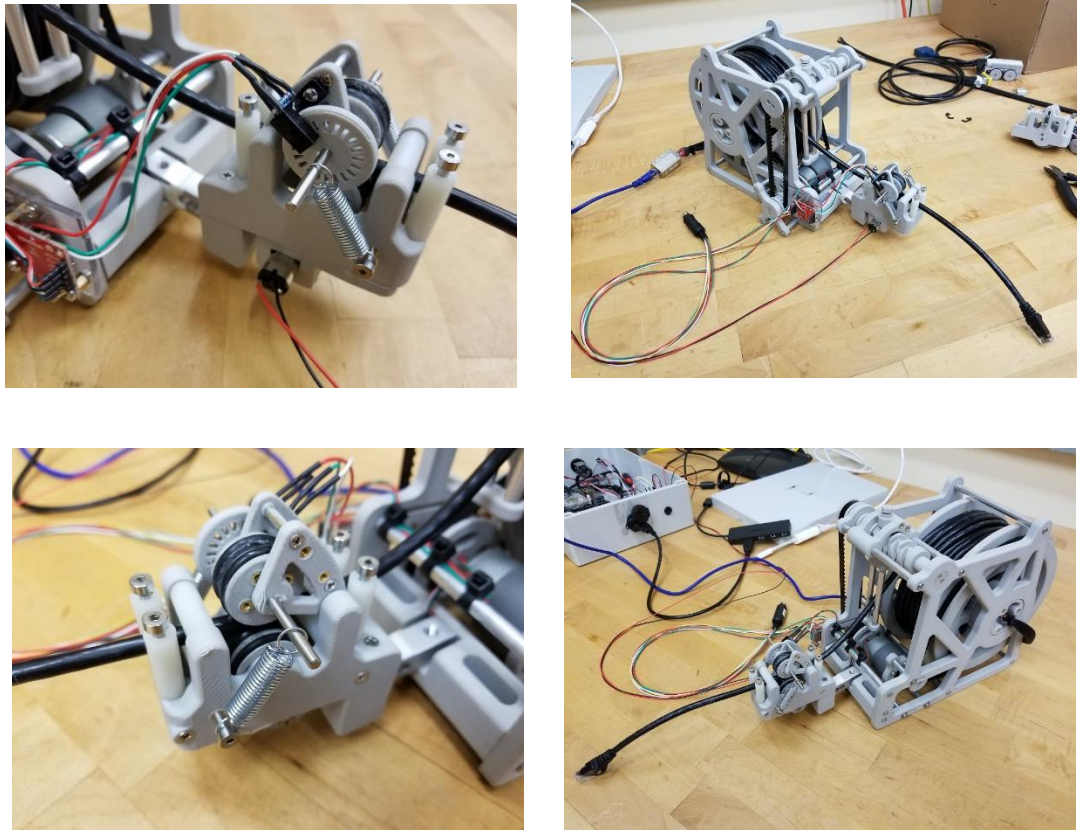
**Figure 54. Redesigned cable management system with an active cable releasing capability.**

The incorporated active cable feeding system, shown in Figure 55, uses a motor to automatically feed the cable to the inspection tool and a tachometer that measures the feeding speed. FIU is also planning to use the load cell embedded in the system mechanism to sense when the cable is in tension, releasing and collecting the tether accordingly, freeing the device from excessive cable dragging and pulling during inspections.



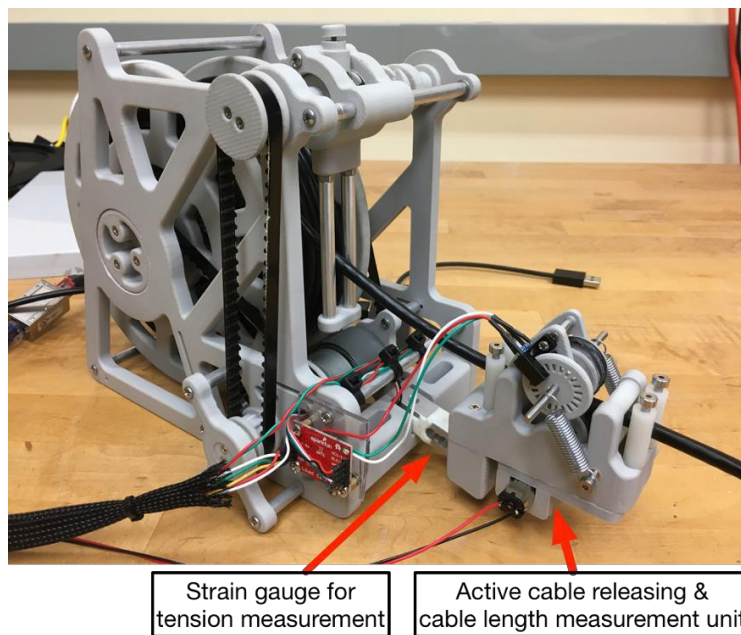
**Figure 55. Active cable feeding systems.**

Figure 56 shows the active cable feeding prototype successfully tested at FIU.



**Figure 56. Prototype of the automated tether management system.**

Finally, Figure 57 shows the most recent prototype currently being tested at FIU.



**Figure 57. Cable management system equipped with active cable release capability.**

## Image processing and semi-autonomous control

Manual control of the inspection tool using a joystick or keypad is challenging for the operators due to the tight channels underneath the tank. Having a semi-autonomous navigational capability would alleviate the complexity of the inspection tasks and allow the operator to focus on the channel inspection. The goal is to implement lane-keeping capability, akin to that of a driverless car, for the inspection tool, so that it will maintain its relative position with respect to the walls of the channels. This is illustrated in Figure 58, where the image stream from the inspection tool's onboard camera is processed to identify the channel boundaries (red lines), which in turn are used for estimating the central line (dotted green line) for the inspection tool to track.

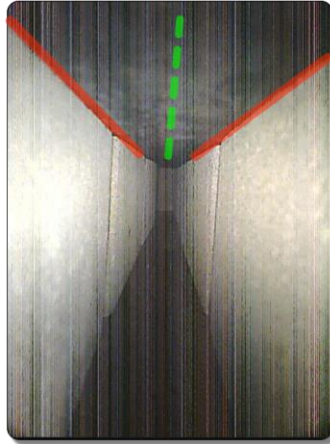


**Figure 58. Image stream obtained from the onboard camera during a test in the mock up channel. Red lines show the wall boundaries while the dotted-green line is the estimated central line, with respect to the wall boundaries.**

An image processing pipeline has been implemented using both the robot operating system (ROS) and OpenCV for detection of the wall boundaries (Figure 59.). The image stream from the inspection tool's onboard camera is first converted to a grayscale image and passed through a thresholding algorithm [Figure 59(b)] to remove the image noise. An edge and line detection algorithm [Figure 59(c-d)] is then applied to the resultant image to extract the line structures in the image and remove outliers. The channel boundaries are then estimated from the detected lines and drawn on the image [Figure 59(e)]. Although the preliminary image-processing pipeline was functional, its performance was highly dependent on the lighting conditions and image noise. Additional improvement was needed to increase the robustness of the pipeline to be more resilient to these two factors.

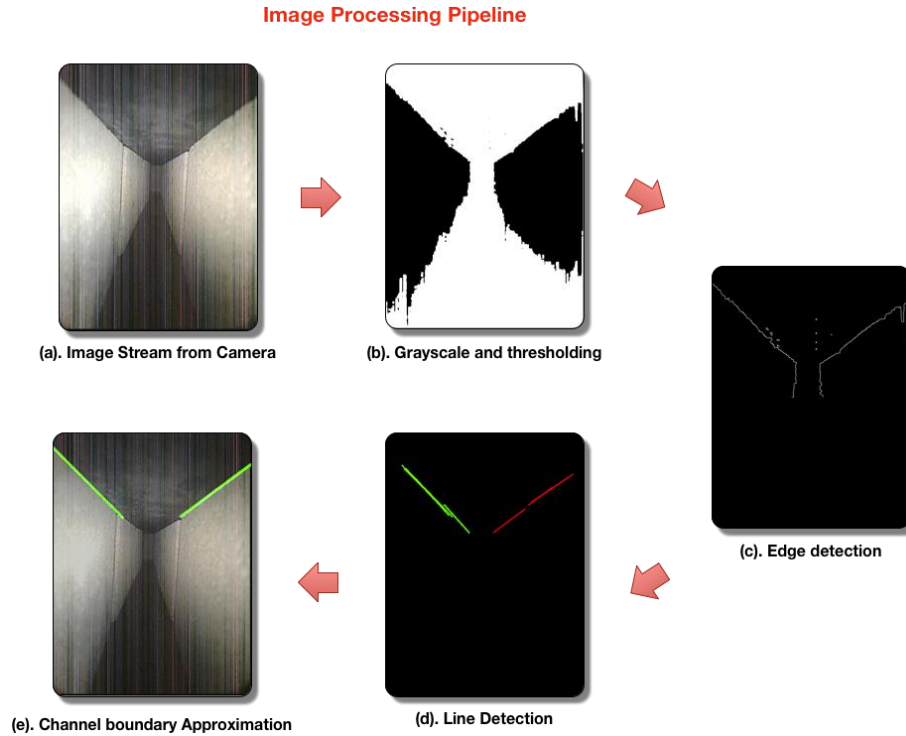


**Figure 59. Image processing pipeline for detecting the channel boundaries.**

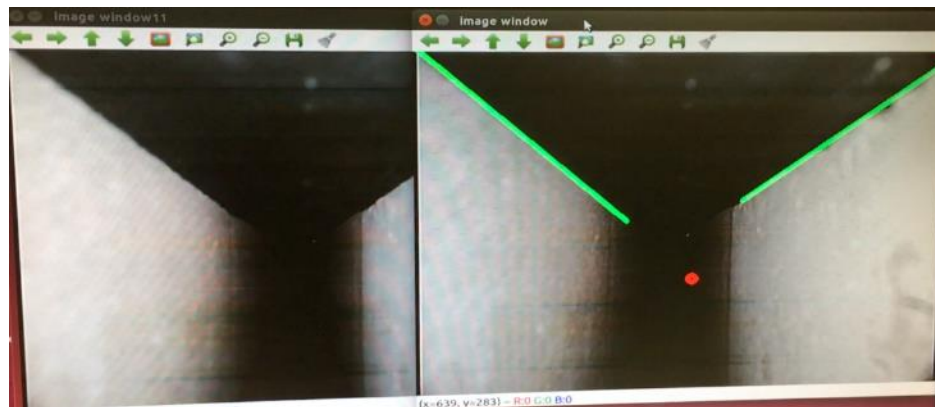


**Figure 60. Raw image from the camera (left) and processed image with the detected channel boundaries overlaid in green (right).**

Additional efforts then concentrated on fine-tuning the camera image processing and proportional-integral-derivative (PID) control of the semi-autonomous control for the mini inspection tool. Some of the parameters for edge and line detection, as well as color segmentation, were fine-tuned. This resulted in a clearer and more stable detection of the lane (Figure 60) for the semi-autonomous control of the inspection tool. A preliminary PID control has been designed and implemented to navigate the mini inspection tool along the central location of the detected lane, while the operator controls the tool’s forward and backward motion. The semi-autonomous operation frees the operator from having to keep the inspection tool away from the narrow refractory wall. Figure 61 shows the PID’s performance in controlling the inspection tool along the reference (Ref) signal.

Although the results are preliminary, the controller was able to navigate the inspection tool within tolerable errors.

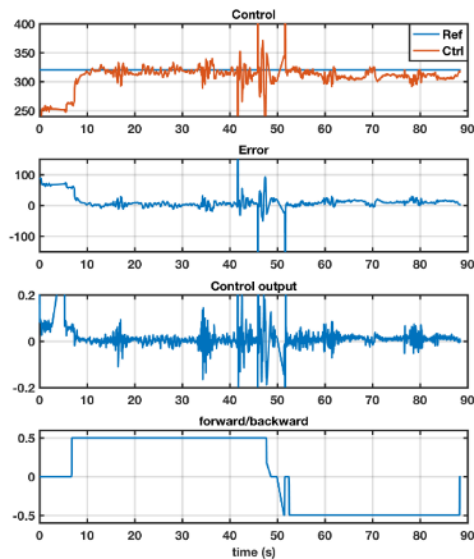


**Figure 61. The control outputs of the PID controller.**

### System testing at the sectional mock-up

A preliminary system test has been conducted at the full-scale sectional mock-up facility built in-house (Figure 62). The mini inspection tool was deployed at the START location, and managed to traverse 38 ft. to the END point. During the testing, the video feedback was streamed live back from the mini inspection tool to the operator, and stored for post inspection analysis. Some of the image captures from the system testing are shown in Figure 63. Results from the testing show that the mini inspection tool is able to pull the tether along the 35 ft. channel and was able to make a 90° turn at the end of the channel. Even though the video feedback was streamed back live to the operator, the image quality was badly affected and corrupted by the motor control signals that were transmitted via the same tether. Work is on-going to mitigate this issue by potentially using a different kind of tether that can provide better shielding capability, or by moving the motor control unit onto the mini inspection tool.

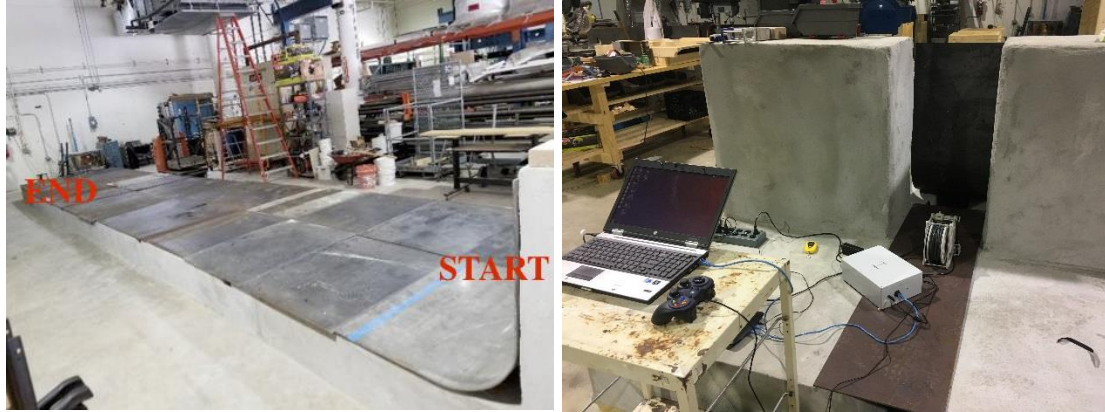


**Figure 62. Full-scale sectional mock-up showing the starting and end point traversed by the mini inspection tool (left) and the experiment setup with operator’s computer, control box and cable management system (right).**



**Figure 63. Image capture of the inner concrete wall of the mock-up (left) and the mini inspection tool reaching the end of the refractory slot (right).**

## PNEUMATIC PIPE CRAWLER

### Background

The pneumatic pipe crawler is an inspection tool designed to travel through the air supply line, leading to the central plenum of a typical DST at Hanford, and to provide live video feedback. For AY-102, the proposed inspection path is approximately 100 feet from grade, down through one of the drop legs, and then lateral to the center bottom of the tank secondary containment, as sketched in Figure 64 below. The route consists of all welded schedule 40 pipes (which are 3 and 4 inches in diameter), reducers and several elbows. The four drop legs branch from the “header ring” with a diameter of 3 inches, transitioning then to 4 inches.



**Figure 64. AY-102 air supply lines.**

The inspection route to the central plenum through the air supply lines has the following requirements:

- Crawl through pipes and fittings (3" and 4" diameter)
- Climb vertical runs
- Tolerate elevated temperatures (170°F)
- Tolerate moderate radiation levels (85 rad/hr)
- Provide a means for removal in the event of a malfunction

Additionally, the crawler will need to provide live video feedback as required; however, other additional instrumentation are also currently being incorporated.

The current design for the pipe crawler is a worm type robot with a modular design, composed of interchangeable cylindrical modules connected with flexible links. Figure 65 shows a rendering of one of the more recent designs of the system.

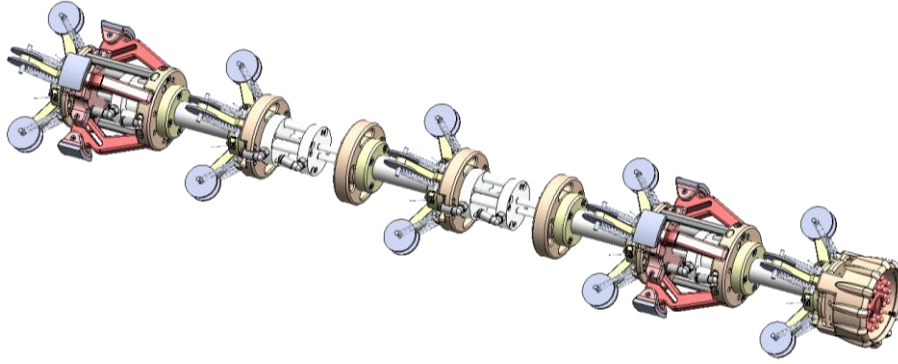


**Figure 65. FIU's pneumatic pipe crawler.**

### Design concept

The design is an evolution of previous pipe crawlers developed at FIU (Pribanic, 2013). The tool inherits the idea of using peristaltic propulsion, powered by pneumatics, and includes an innovative design with a modular approach that utilizes off-the-shelf pneumatic actuators to produce the contractions of the peristaltic motion.

A pneumatic powered crawler is suitable for highly radioactive environments with potential exposure to flammable gases. The locomotion system does not require embedded radiation hardened electronics and electric actuators. The design is also inherently ignition proof, since pneumatic actuators are not likely to produce electric sparks common in some electric motors and actuators.

In addition, the peristaltic propelled crawler offers an appropriate design for the radioactive environment. The device can navigate inside a pipeline without using any external moving parts, such as wheels and continuous tracks, and could be designed to be fully encapsulated in a disposable elastic skin. In extreme cases, the crawler itself can be considered disposable, due to its affordable design.

Another advantage is associated with its modular design, which has the potential to be customizable. Other specific tasks could be accomplished with the addition of extra modules, such as instrumentation, material sampling, and pipe repair.

As shown in Figure 66, the crawler's basic design is composed of five modules linked by flexible connections:

- a) the front camera,
- b) the front and back grippers, and
- c) the two middle expansion modules.

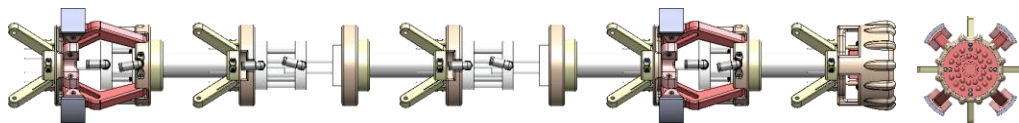


**Figure 66. Pneumatic pipe crawler.**

The crawler also includes three additional components: a control box, a tether, and an instrumentation module which is currently being designed. The new module will use an embedded computer for instrument control and communication.

With the control box, the crawler movement is fully automated and can be controlled remotely using any handheld device connected to the private wireless network of the box. The controlling software is customizable, which increases the versatility of the tool. Figure 67 shows the shows the most current prototype currently being tested at FIU.

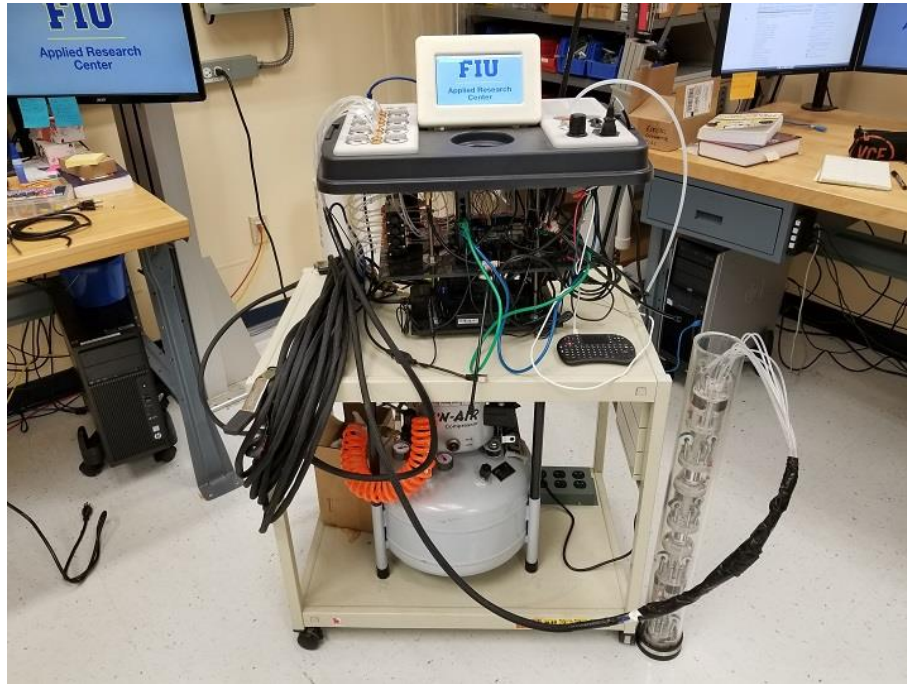


**Figure 67. Current pneumatic pipe crawler prototype.**

The crawler's recent improvements include the addition of a new instrumentation module. The module has been designed to provide additional sensor feedback from the crawler during inspections. The new module will enhance the inspection tool capabilities, robustness and operational feedback.

As illustrated in Figure 68, the following additional sensors are being integrated into the inspection tool:

- Thermal infrared camera to the camera module, providing thermal image mapping, hot spot detection and temperature gradient analysis.
- Ambient temperature, pressure and humidity, providing environmental conditions.
- Wall scanner module, providing radiation, ultrasound, and visual surface mapping.
- Tether force to the last module, providing drag estimation.
- Contact pressure sensors to the grippers, providing grip conditions.
- Inclinometer, providing slope and orientation for each module.

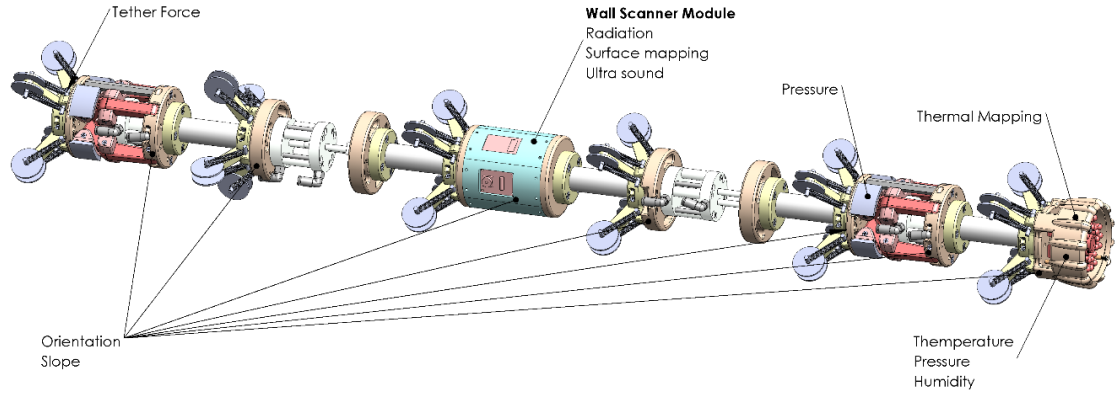


**Figure 68. Sensor integration.**

In addition, an embedded computer integrated with the module will control, manage and communicate with the sensors in the device. A controller area network (CAN bus) protocol will be used to communicate from the on-board computer to the portable control box thru the tether.

The sensors currently being considered for prototyping are listed below. The currently selected sensors are affordable while high precision versions may be considered for site deployment.

Description	Sensor
Thermal infrared camera	FLIR LEPTON® Long Wave Infrared (LWIR)
Ambient temperature, pressure and humidity	Adafruit BMP280 I2C or SPI Barometric Pressure & Altitude Sensor
Radion	Teviso RD2014
Ultrasound	Ultran Group WD25-2
Visual surface mapping	PTC06 Serial Camera Specification
Tether force	Phidgets Micro Load Cell CZL635 (0-20kg) SparkFun Load Cell Amplifier - HX71
Pressure sensors	Sparkfun Force Sensitive Resistor 0.5"
Inclinometer	AltIMU-10 Gyro, Accelerometer, Compass, and Altimeter

The new additional instrumentation module will be a carrousel type scanner that rotates and maps the surface along the pipe inspection. As illustrated in Figure 69, the module uses 6 modular panels that can be customized for different sensors.

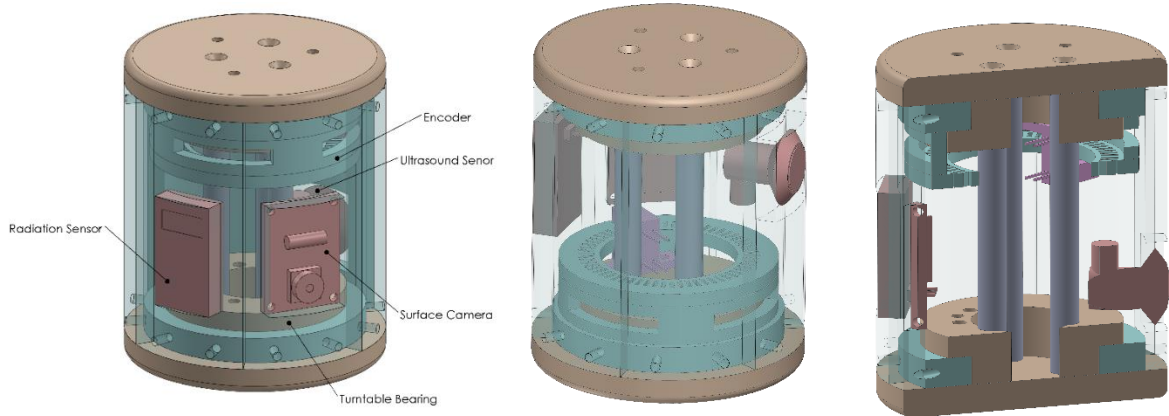


**Figure 69. New instrumentation module.**

As part of the continuous improvement of the crawler, FIU has considered using a pancake pneumatic cylinder in future versions of the actuator modules. Shown in Figure 70, this type of cylinder combined with return springs has the potential to reduce the module size, as well as improve maneuverability and retrieval.

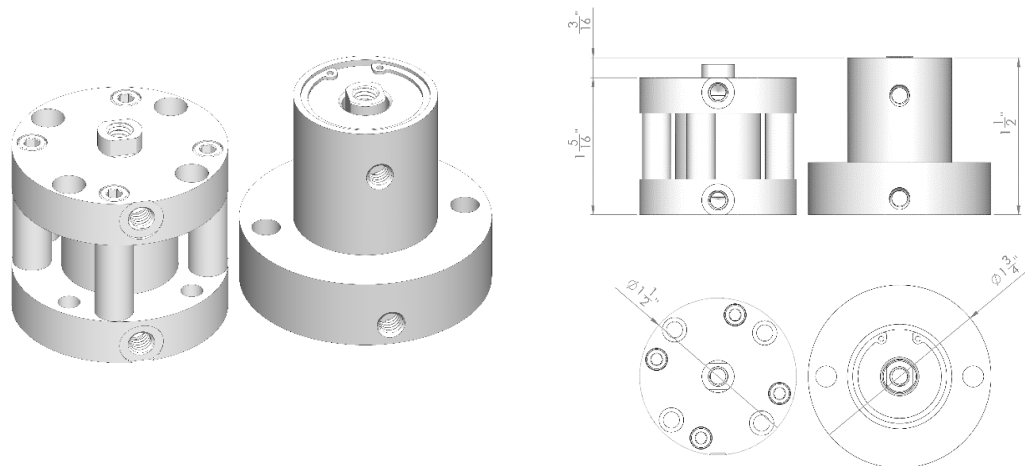


**Figure 70. Crawler current pneumatic actuator (left) and considered pancake cylinder (right).**

FIU has also evaluated several auxiliary technologies such as nondestructive techniques, sensors, LIDAR, SONAR, communication protocols and microcontrollers that have the potential to improve the current crawler design and capabilities. Minor improvements were also made to the software framework that controls the inspection tool.

## DST FULL SCALE SECTIONAL MOCKUP

FIU has been developing a full scale sectional mockup of the bottom section of a double shell tank. The testbed has been designed to be customizable with a modular design that can reproduce inspection conditions in Hanford tanks. This includes various configurations of the refractory pad, cooling channels, supply airlines and plate thicknesses. Defects such as damaged welds, and *in situ* bottom cracks can also be simulated. The mockup will also be capable of evaluating future inspection technologies, delivery systems and robotic devices. The mockup design has been extensively coordinated with the site engineers at WRPS, and extra care will be taken to assure a high correlation between the mockup and the in-field conditions. Figure 71 illustrates an early version of the mockup design, which was redesigned to be more versatile and cost effective.

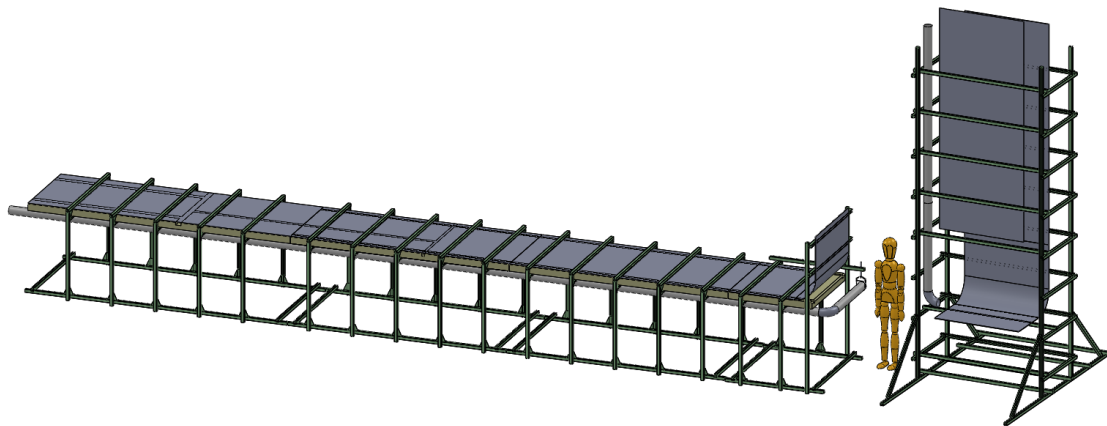


**Figure 71. Original mockup design.**

As seen in Figure 72, the metal structure was removed in a redesign and the sectional mockup was enhanced to address corrosion problems in the secondary liner of the DSTs.

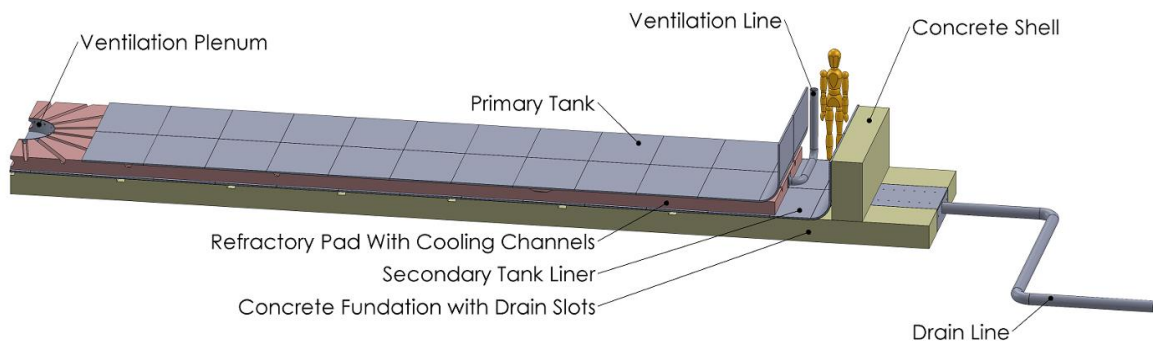


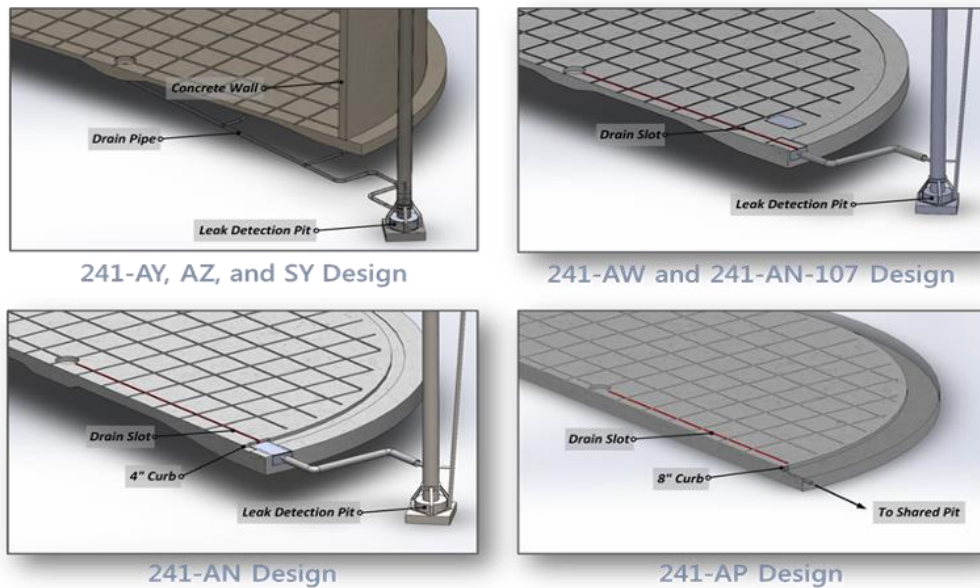
**Figure 72. Current mockup design.**

The redesigned mockup not only includes the ventilation channels in the refractory pad of the primary tank, but it also includes the leak detection system in the foundation slab of the secondary tank liner. The full structure is 8 ft wide and 37.5 ft long and emulates the following elements of the tank:

- concrete foundation with draw slots,
- 6” drain line,

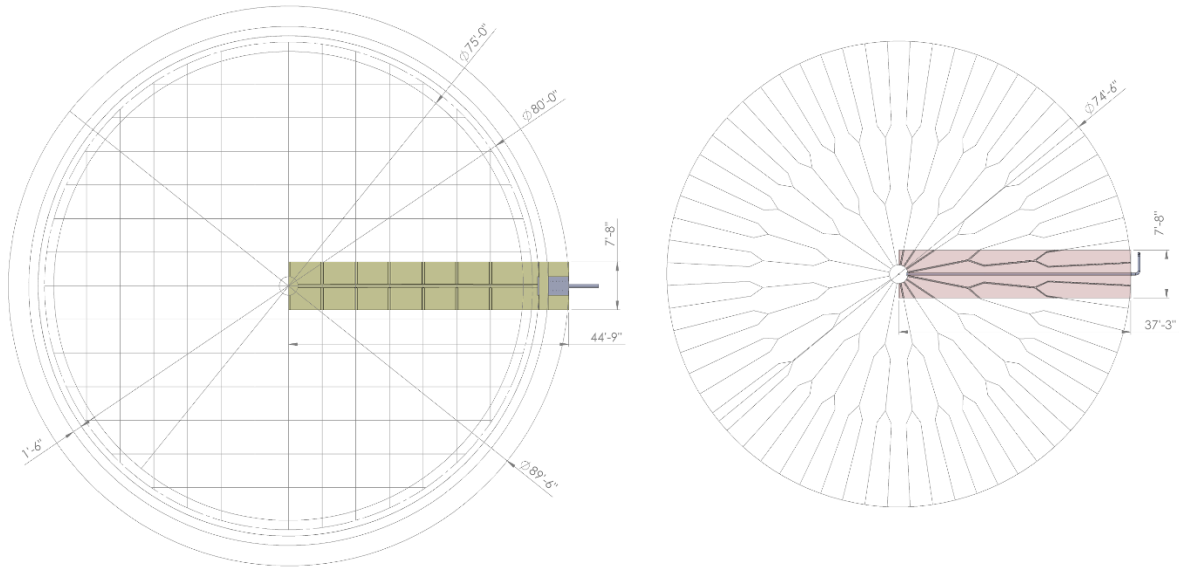
- concrete shell,
- secondary tank liner,
- refractory pad with cooling channels,
- 4” ventilation line,
- primary tank, and
- tank center plenum.

Figure 73 shows the existing leak detection configurations used in the double shell tanks at Hanford. FIU’s mockup is based on the 241-AN, 241-AW and 241-AN-107 designs which constitute a majority of the configurations.



**Figure 73. Existing configuration of the DST’s leak detection system.**

As illustrated in Figure 74, the mockup covers approximately 7% of the DST’s foundation with the 8 ft swath.



**Figure 74. Layout of the tank foundation drains (left) and cooling channels (right).**

Figure 75 shows the layout of the concrete foundation in the mockup under the secondary tank liner. The foundation leak detection system has a maze of sloped drains. In the mockup, the drains are sloped and angled according to the double shell tank’s shop drawings, and they are suitable to address corrosion issues in the inspection of the bottom of the secondary tank liner.

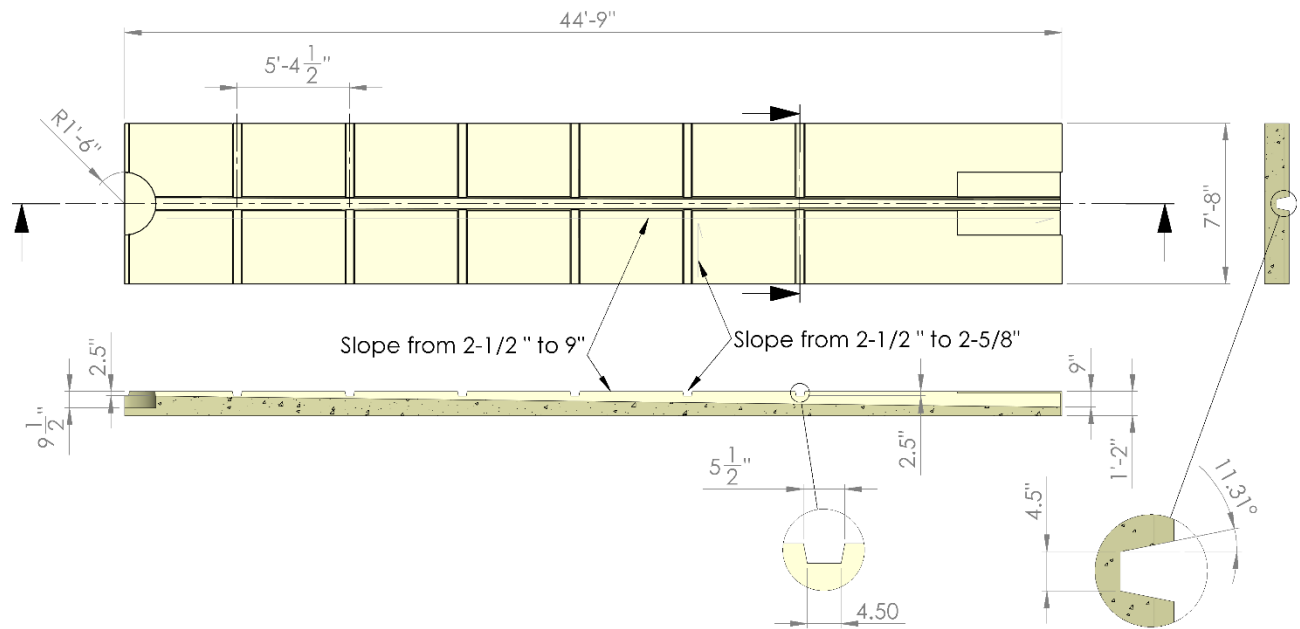
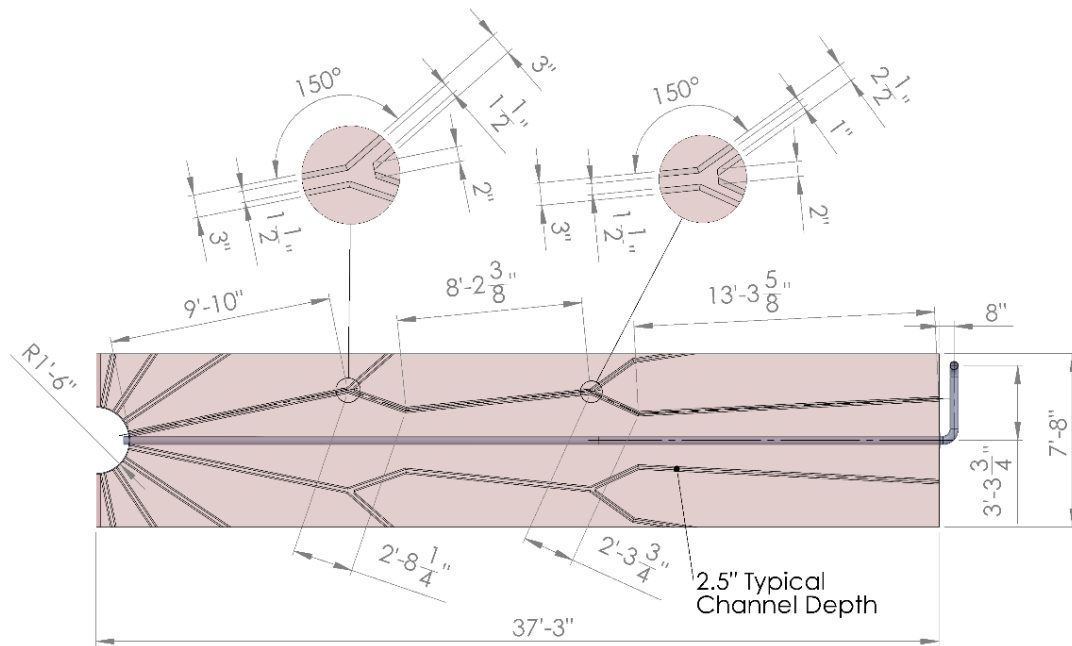


**Figure 75. Concrete foundation with drain slots.**

Figure 76 shows the layout of the refractory pad in the mockup under the primary tank. The mockup has two full length cooling channels reaching from the tank annulus to the center plenum. This configuration is suitable for testing emitter-receiver sensor technologies, such as long-range guided ultrasonic waves, which would require multiple sensors simultaneously located in both

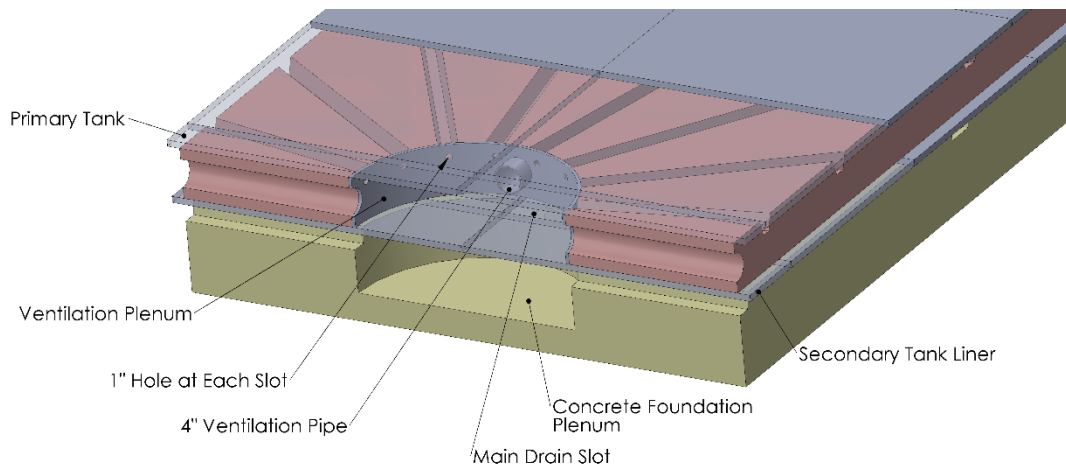
ARC Year-End Technical Progress Report

channels. The refractory mockup also includes one of the carbon steel 4" ventilation pipe lines, the only feasible way to provide access to the tank central plenum.



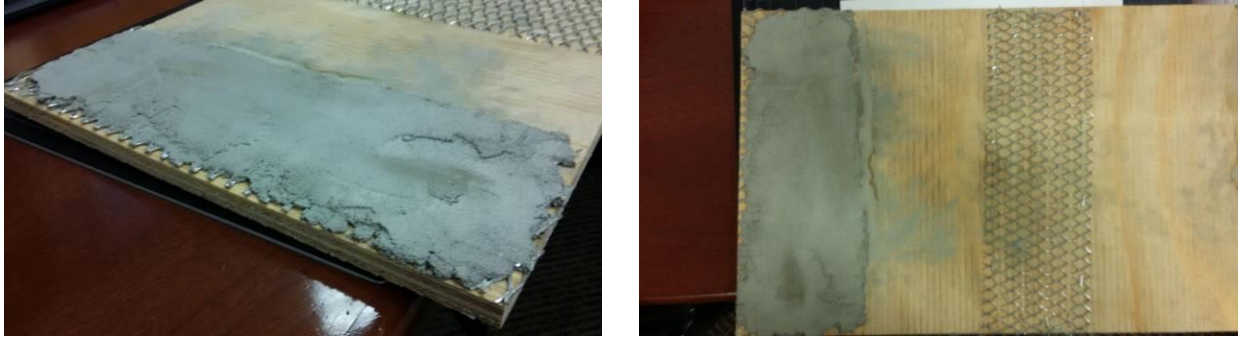
**Figure 76. Refractory pad with cooling channels.**

Figure 77 shows the mockup of the central plenum, which is also constructed in accordance with the DST drawing provided by WRPS.



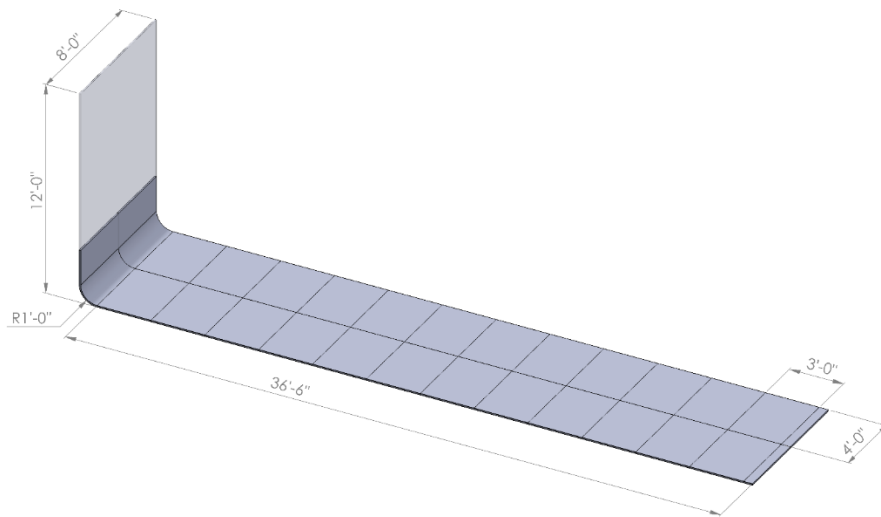
**Figure 77. Tank central plenum.**

The mockup foundation and refractory pad are made of a wood frame coated with concrete. The concrete coating is approximately 1/2" thick in the foundation and in the refractory. The concrete is held by a metal mesh attached to the wood frame. Shown in Figure 78, this combination provides a lighter structure combined with surface properties similar to the refractory in the Hanford tanks.



**Figure 78. Mockup foundation and refractory pad concrete coating.**

In the mockup, the concrete foundation and the refractory pad will lay on the floor covered by the metal plates. The tank walls are made of 3 ft long by 4 ft wide metal plates with 1/4" thickness. The configuration is shown in Figure 79.



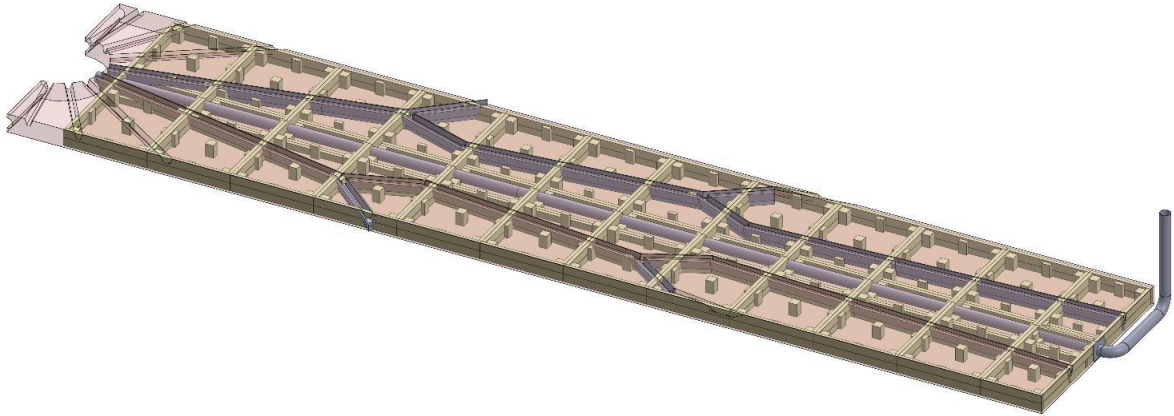
**Figure 79. Primary tank layout.**

Figure 80 shows subsequent stages of the mockup foundation during construction at FIU.



**Figure 80. The full-scale HLW tank mockup.**

Similar to the concrete foundation, the refractory pads have a wooden structure which will be coated with concrete. Figure 81 shows the design of the refractory pad with cooling channels.



**Figure 81. Design of the refractory pad structure with cooling channels.**

The refractory pad are being constructed from sectional boxes made of plywood, as shown in Figure 82. The boxes will have slots cut to form the network of refractory channels. After the slots are created, the wood boxes will be covered in an asphalt felt and a metal lath will be placed on top. A thin layer of concrete (around 1/2") will then be added onto the lath and the secondary liner will be installed. This will complete the initial construction of the test bed.



**Figure 82. Plywood boxes that form the refractory.**

## CONCLUSIONS AND FUTURE WORK

---

The miniature rover inspection tool has been redesigned to improve its overall functionality. PCBs were designed and fabricated for the base, camera and sensors to reduce wire clutter in the inspection tool. It also removed tension from the wires while the inspection tool is in operation. The use of PCBs also allowed patch LEDs to be used as the lighting source, thus increasing the amount of light and improving the image quality of the camera feed.

Sensor integration for the inspection tool was carried out as part of the performance year efforts. Among the sensors considered were temperature, humidity and radiation sensors. The sensors were fitted onto their respective sensor hoods that provide a common power and communication interface with the base unit. This allows the sensor hood to be interchangeable for different inspection tasks.

An active cable management system that automatically releases and reels in cable has been designed to aid the limited pull-force that the inspection tool can generate. In addition, a controller box to house all of the necessary electronic components required to operate the inspection tool and the cable management system has been constructed. Furthermore, an Xbox controller can be attached to the controller box for manual operation of both the inspection tool and the cable management system, when needed.

To ease the inspection operation within the narrow refractory channels, semi-autonomous control of the inspection tool has been designed and is being fine-tuned. Images from the inspection tool's camera were processed to implement lane-keeping capability. This freed the operator from having to keep the inspection tool in the center of the channels, allowing them to focus their attention on the inspection tasks at hand.

Preliminary testing has been conducted at the full-scale sectional mock-up facility built in-house. Test results showed that the mini inspection tool was able to overcome the friction generated by the tether and managed to traverse the full length of the refractory channel. Work is ongoing to correct the signal corruption issues and improve the quality of the images streamed back from the mini inspection tool camera. Future work includes testing the mini inspection tool with the integrated sensors and validating the results in the mock-up facility.

FIU has also continued to test and improve the pneumatic pipe crawler developed for inspection of 3- and 4-inch pipelines. The primary improvement includes the integration of sensors, with the objective of enhancing the inspection tool capabilities, robustness and operational feedback. The integration of the following sensors are being considered: (a) a thermal infrared camera to provide thermal image mapping, hot spot detection and temperature gradient analysis; (b) ambient temperature, pressure and humidity sensors to provide environmental conditions; (c) a wall scanner module to provide radiation, ultrasound, and visual surface mapping; (d) a load cell to provide tether drag estimation; (e) contact pressure sensors to provide grip conditions; and (f) inclinometers to provide slope and orientation of each module of the crawler. The addition of an automated cable management systems will be considered as well. In the next period of performance, the design of a larger scale crawler that can navigate through the 6-inch drain pit pipeline will be developed using the lessons learned from the initial system. FIU will also investigate the development of a conceptual design for a 2-inch version of the pipe crawler.

Lastly, a full scale sectional mockup of the DST floor was designed and its construction is almost completed. FIU will continue to make improvement of the testbed based on guidance from WRPS to assure a high correlation between the mockup and the Hanford tanks. The mockup can also be used to evaluate future inspection technologies, sensors and robotic devices in operational conditions equivalent to those at Hanford.

## **TASK 18.3**

# **INVESTIGATION USING AN INFRARED TEMPERATURE SENSOR TO DETERMINE THE INSIDE WALL TEMPERATURE OF DSTS (FIU YEAR 7)**

## **EXECUTIVE SUMMARY**

---

Corrosion in DSTs is one of the primary concerns at Hanford and other sites. It is managed by stringent operating specifications as given in OSD-T-151-00007 “Operating Specifications for the Double-Shell Storage Tanks” (OSD) [1]. One of the important parameters specified by OSD is the temperature which plays an important role in corrosion. In general, the tank temperatures are determined by various processes and most of these methods are approximations of the actual temperatures at various locations inside the DST’s. Hence, there is an immense need for accurate measurements and calculations of actual temperatures inside the tanks. Of particular interest is at the interface of the tank waste and the inner walls since it accounts for the region highly prone to corrosion.

The present task investigates in the use of an infrared (IR) sensor to measure the outer wall temperatures of the primary shell in the DST. This process is practical since the sensor is expected to “piggy back” on the scheduled inspection tools passing through the annulus of the DSTs. The method checks whether the temperatures are within limits and may aid in obtaining accurate data for input to thermal models and, in some cases, validate the models. During the previous year, bench-scale testing has been initiated to validate the feasibility and use of the IR sensor for DST measurements. The DSTs were represented using rectangular tanks. The IR sensor, as recommended by the WRPS site engineers (Raytek MI3 [4] sensor), was procured, calibrated and preliminary tests were conducted. The sensor results were compared to those obtained from manual measurements using thermocouples. In addition, heat transfer based models were generated and solved using commercially available software (Solidworks 2013) to study the temperature profiles in the primary tank walls.

The bench-scale testing has been successfully completed with enhancements to the previous year’s efforts. This included the automation of the data acquisition system for real-time measurements during the tests and the use of testing temperature conditions that replicate actual DST temperatures. In addition, emissivity calibration tests were conducted to validate the IR sensor for use with other materials such as stainless steel along with carbon steel. Further, the Raytek IR sensor was investigated for integration into two robotic inspection devices: the mini-rover and the pipe crawler. The sensor can be used in conjunction with temperature dependent UT sensors for calibration.

## INTRODUCTION

---

One of the important variables specified by the operating specifications of double shell tanks is temperature. It plays a vital role in the initiation and propagation of corrosion in metals. Since DST's are made of carbon steel and store nuclear waste in various forms, it is essential to know the exact temperatures in the tanks especially at the waste-wall interfaces.

Hence, the present task aims to check the validity of the use of a non-contact pyrometer to measure the outer temperatures of the primary tank wall in DST's. This method of measuring the wall temperature can be used with the current inspection equipment or the sensor can be attached to an annulus inspection camera. At FIU, two robotic inspection tools are being developed and the IR sensor can easily be attached to them as a built-in or as a separate module. "Piggy backing" of the sensor to pre-scheduled operations allows for the collection of temperature data with minimal impact on tank farm operations. The temperature results thus obtained will serve multiple purposes: (a) ensuring that the limits are met and, if not met, allow for immediate corrections; (b) physical properties can be empirically calculated, providing validation/evaluation of the current thermal modeling capabilities; (c) temperature gradients would help in the estimation of solid waste levels in the tanks; (d) the IR sensor can also be used to calibrate other equipment; and (e) expensive and time consuming thermal modeling can be minimized or avoided in certain conditions.

To be used in the DST's, the IR sensor needs to meet the following requirements:

- Must be a non-contact pyrometer
- Must be mounted and remote controlled
- Should be wired (long wire must be available 50' – 75')
- Must be able to get temperature from dull/rusty carbon steel
- Must be able to get an accurate reading from a distance of 1-3 inches
- Must have software compatible with windows machine (Windows 7)
- Software must support data logging
- Temperature measurements will be 0°F to 250°F
- Able to operate in an environment of 40°F to 150°F
- Equipment must have adjustable emissivity
- Spectral range between 8  $\mu\text{m}$  and 14  $\mu\text{m}$
- Aperture less than 1"

Based on the above requirements and discussions with site engineers, the Raytek MI3 infrared sensor was selected and a bench-scale test plan was developed and implemented. The bench-scale experiments were initiated in the previous performance year and concluded this year. This year's work included sensor validation tests, emissivity calibration tests and an investigation into integrating the IR sensor with the mini rover and pipe crawler. A summary of the sensor validation tests and integration with the inspection tools is provided in the next section.

## SENSOR VALIDATION TESTS

---

The Raytek mini IR sensor details and the initial tests and results were discussed in the previous year's report and the research work has been presented at the IMAPS conference [8]. During this past year, there validation experiments were completed by developing an automated data acquisition system and emissivity calibrations for the IR sensor.

The experimental setup consisted of a rectangular stainless steel tank of dimensions 2'x4'x3'. Fluid (water) was heated in the tank and a thick carbon steel plate of 1/2 inch thickness (replicating a section of the DST wall thickness) was suspended onto the fluid surface using strut channels and cables/rods. A side mount heater (4000 W immersion heater from Tempco (TAT 40002)) was used to increase the water temperature and measurements were recorded at various time intervals. The experimental set up of the tank is shown in Figure 83a. During the experiments, the tank was covered with insulation (Figure 83b) to minimize the heat loss to the atmosphere and to acquire accurate data.



Figure 83. a) Experimental set up



b) tank covered with insulation.

The Raytek IR sensor was used to measure temperatures on the outer surface (exposed to the atmosphere) of the plate while it transferred heat from the hot water to the ambient air outside. Heat transfer calculations provided a prediction of the temperatures on the inner surface (exposed to the fluid). Also, thermocouples were inserted at various set points to obtain accurate readings. To validate the use of the Raytek IR sensor, temperature measurements were taken at the top surface using thermocouples. Initially, roller surface K-type thermocouples along with the universal thermocouple connectors (UTC-USB) were used manually to acquire the temperature data. In the second phase, the process was automated using permanently fixed hermetically sealed thermocouples (HSTs) [5] and the multiple channel data acquisition (DAQ) system from omega (OM-DAQ-USB-2401) [6]. The HSTs were fixed onto the outer and inner surface (in contact with water) of the plate using a thermally conductive epoxy (OB-101) [7] to obtain real-time temperature measurements for continuous monitoring. The plate's inner surface with fixed HSTs is shown in Figure 84a.

The omega DAQ system is suitable for 8 differential or 16 single ended analog inputs. It is user programmable for Type J, K, T, E, R, S, N, B thermocouples or voltage input and comes with customized windows compatible software. It provides a 12volts DC output for sensor excitation. Figure 84b shows the DAQ system attached to the thermocouples while Figure 84c shows the dashboard with data displays of temperature.



Figure 84. a) HSTs fixed under the plate b) DAQ system with thermocouples c) DAQ dashboard.

The temperatures were measured at 6 points on the plate using HST’s and at 3 top surface points using the Raytek sensor. The results obtained are tabulated in Table 9.

**Table 9. Temperature (IR Sensor and HSTs) in °F**

Data point	T1	T2	T3	B1	B2	B3	R1	R2	R3
1	111.14	104.23	106.07	114.67	109.28	108.78	109.2	106.4	104.7
2	115.35	111.12	111.19	120.1	115.34	115.12	116.7	112.7	109.9
3	123.27	111.83	117.29	130.2	126.05	125.4	132.9	128.9	124.6
4	132.12	116.57	125.98	140.32	135.96	135.27	143.9	141.7	133
5	142.09	132.99	137.44	150.06	145.25	144.53	152	145.7	141.7
6	152.91	142.71	138.7	160.17	154.42	153.67	157	155	153.1
7	162.73	151.41	148.01	170.05	164.45	163.6	165.2	167.2	166.2

@T – Top surface, B – Bottom surface, R – Raytek

In Table 9, the columns T1, T2 and T3 represent the thermocouple readings while R1, R2 and R3 represent the Raytek sensor readings at the same locations. Thus, these values are compared. It was determined that the average difference between the corresponding readings for location 1 was 5.3°F, while for location 2 and location 3 was 12.3°F and 6.9°F, respectively. It was observed that the temperature difference increased with an increase in temperature. In most cases, the Raytek sensor showed a higher value. In addition, the temperatures at the top 3 locations, T1, T2 and T3 were compared to the bottom 3 locations, B1, B2 and B3 to investigate the heat transfer effects. From the results, it is inferred that the average temperature difference was 6.5°F, 11.4°F, and 8.8°F, respectively, for the three locations. According to theoretical calculations, the average readings can approximate 4-5°F taking into account the temperature gradients with location and time.

In addition, the emissivity experiments were also conducted to check the sensor’s validity for carbon steel and stainless steel materials. The first experiment conducted utilized the carbon steel plate. Since the emissivity value of carbon steel was not precisely available in literature, an initial estimate of 0.75 was chosen and a range of values above and below the initial estimate was recorded. The experiment consisted of the ambient temperature measurement on a carbon steel plate (1/2 inch thick) using both a Raytek and a hermitically sealed thermocouple. The second experiment was conducted on the tank wall which consisted of stainless steel. Emissivity values were changed from 0.3 to 0.6. The experimental set up for emissivity tests and the IR sensor are shown in Figure 85.



**Figure 85. Emissivity experiment with Raytek sensor a) carbon steel plate b) stainless steel tank wall.**

Results obtained from both experiments are given in Table 10 and Table 11. In Table 10, the temperature was recorded at three different points using both sensors. It is evident from the table that the temperature readings were close when the emissivity value ranged from 0.76 to 0.79 and precise at 0.78. Also, it should be noted that for the emissivity change from 0.7 to 0.8, the temperature values were precise within a maximum of 2-3°F. Hence, the emissivity of carbon steel can be taken as 0.78.

**Table 10. Experimental Results with ½ in Carbon Steel Plate (Temperature Readings in °F)**

Emissivity (Raytek)	Raytek (point 1)	Raytek (point 2)	Raytek (point 3)	TC (point 1)	TC (point 2)	TC (point 3)
0.7	69.5	68.5	68.7	72.88	73.25	71.66
0.71	65.9	64.4	66.8	73.43	71.13	75.78
0.72	68.2	70.2	70.2	73.05	71.33	71.07
0.73	68.9	67.4	67.8	73.13	70.77	73.97
0.74	66.4	67.6	66.8	72.92	71.37	72.42
0.75	68.4	68.6	68.1	62.98	66.08	66.49
0.76	66.8	68.7	68.3	68.69	69.97	68.22
0.77	70.6	67.5	66.9	69.65	68.08	70.03
0.78	70.9	69.7	68.9	70.49	70.15	70.58
0.79	70.9	69.8	68.5	71.24	70.14	72.28
0.8	70.6	71.4	70.2	72.19	73.2	72.54

**Table 11. Experimental Results on Stainless Steel Plate (Temperature Readings in °F)**

Emissivity (Raytek)	Raytek	TC
0.3	40.4	73.42
0.4	52.8	73.54
0.5	61.4	73.23
0.6	73.7	74.34

In the case of stainless steel, it was observed (Table 11) that the emissivity value of 0.4 to 0.5 provided an inaccurate temperature reading but at an emissivity of 0.6, both Raytek and thermocouple readings were close with less than a 1°F temperature difference. So, the emissivity of stainless steel can be taken as 0.6. With these results, a method has been established to accurately calibrate the sensor for different material types and emissivity values.

## SENSOR INTEGRATION WITH INSPECTION TOOLS

Integration of the IR sensor with the inspection devices developed in task 18.2 was also investigated. The miniature magnetic rover developed for carbon steel pipe inspections was chosen as a base model to integrate the mini IR sensor.

The IR sensor head was initially placed on an empty chassis of the mini rover to estimate the size and appearance of the unified system, shown in Figure 86a. The sensor head was placed along the length of the rover and the cable can be directly attached to the tether of the mini rover.

The sensor head was then temporarily mounted to the actual mini rover and basic temperature readings were obtained. The sensor head attached to the mini rover inside the scaled DST mock-up channels is shown in Figure 86b and c.

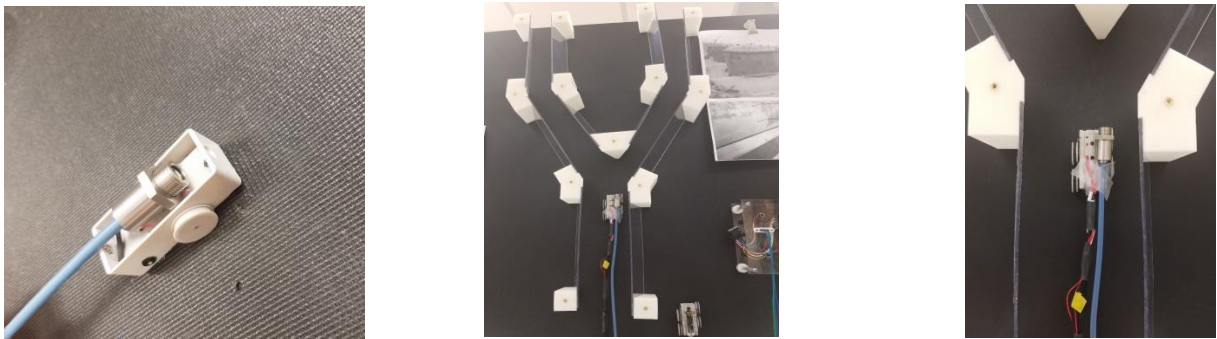


**Figure 86. IR sensor head on the rover: a) empty chassis b) actual rover in the tank channels c) detailed view.**

Alternative sensor locations, as shown in Figure 87, were considered, since frontal, rear and angular measurements are often needed inside the pipe.

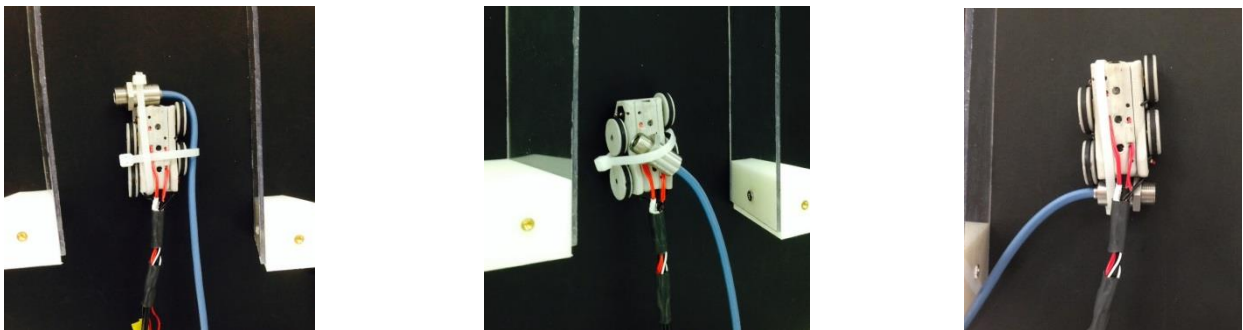


**Figure 87. IR sensor head attached at: a) front b) top (angular) c) rear.**

Various mounting techniques such as clip-on-and-clip-off versus glue or adhesive bonding versus screws, etc. are currently being considered for semi-permanent mounting of the sensor head to the mini rover and similar pipe inspection tools to investigate the feasibility of its use in pipes and tanks.

The integration of the IR sensor with the pneumatic pipe crawler inspection device developed for tank inspections was also evaluated. The pneumatic crawler is modular and the sections connecting the modules provide a decent base for IR sensor incorporation. The IR sensor was fixed temporarily on the pneumatic pipe crawler as shown in Figure 88a. This area is untouched by the

springs or the pipe. The pneumatic crawler with the Raytek sensor was inserted into the clear pipe PVC loop as shown in Figure 88b.



**Figure 88. a) IR sensor head on the pneumatic pipe crawler b) sensor head and crawler inside the clear pipe.**

Currently, FIU is researching options for permanent integration of the IR sensor with the pneumatic pipe crawler. Options include designing an additional sleeve to house the sensor and remodeling the crawler tether housing in the modules to accommodate the IR sensor's tether. In addition, tests will be run in carbon steel pipes using this assembly.

## **CONCLUSIONS AND FUTURE WORK**

---

Bench scale experiments were conducted to validate the use of the Raytek mini IR sensor for use with the inspection devices to be deployed to actual sites. Automated data acquisition systems were used along with the HSTs permanently fixed to the inner and outer surface of the test piece for accurate thermal measurement and validation. Also, a temperature range as specified for the DST's (120-170°F) was used. The experiments were conducted to investigate the sensitivity of the Raytek IR sensor to different emissivity values and materials. A method has been established to accurately calibrate and test the Raytek mini IR sensor. The tests were conducted with hot water (liquid medium).

In addition, the option of potential integration of the IR sensor with inspection devices for deployment into the tanks was investigated. This task will be merged with the mini-rover and crawler tasks in the next performance year to make design modifications for integration.

## REFERENCES

---

1. OSD-T-151-00007, Operating specifications for the Double-Shell Storage Tanks, Rev 1, Washington River Protection Solutions, Richland, WA.
2. Holsmith, B. (2015). Double Shell Tank Primary Wall Temperature Measurements: Suggested New Technology White Paper, Washington River Protection Solutions, Richland, WA.
3. The Principles of Noncontact Temperature Measurement, produced by Raytek® available online at [http://support.fluke.com/raytek-sales/Download/Asset/9250315\\_ENG\\_D\\_W.PDF](http://support.fluke.com/raytek-sales/Download/Asset/9250315_ENG_D_W.PDF)
4. [www.raytek.com](http://www.raytek.com)
5. <http://www.omega.com/pptst/HSTC.html>
6. <http://www.omega.com/search/eseach.asp?start=0&perPage=10&summary=yes&sort=rank&search=OM-DAQ-USB-2401&submit=Search&ori=OM-DAQ-USB-2401>
7. [http://www.omega.com/pptst/OB-100\\_OB-200\\_OT-200.html](http://www.omega.com/pptst/OB-100_OB-200_OT-200.html)
8. Aravelli, D. McDaniel, A. Abrahao, A. Awwad, C. Davila, “Thermal Measurement and Modeling of Nuclear Waste in the Double Shell Tanks at Hanford Nuclear Waste Site Using Miniature Sensors,” International Microelectronics Assembly and Packaging Society (IMAPS) 2016, Pasadena, CA, October 11-13, 2016.

## **TASK 19.1 PIPELINE CORROSION AND EROSION EVALUATION (FIU YEAR 7)**

### **EXECUTIVE SUMMARY**

---

A fitness-for-service (FFS) program has been implemented by Washington River Protection Solutions (WRPS) to assess the structural integrity of pipelines, tanks and tank farm waste transfer system. The purpose of the program was to inspect primary piping, encasements, and jumpers for corrosion/erosion which has been accomplished in the previous years. As recommended, at least 5% of the buried carbon steel DSTs waste transfer line encasements were inspected. Data has been collected for a number of these system components and analyzed.

Previous efforts from FIU included the evaluation of ultrasonic transducers that can provide real-time thickness measurements for transfer system components. Initially, a market study was conducted on various commercially available ultrasonic transducer systems according to the requirements listed by the WRPS/DOE personnel. Out of the many options, some of the sensors were procured and tested. Since the data acquisition systems were expensive; two of the viable options were down selected.

During this past year, one of the down selected UT sensor systems, from the manufacturer Permasense, was acquired and initial bench-scale validation tests have been successfully conducted. The bench-scale test loop consisted of 2- and 3-inch diameter pipe sections with elbows and straight sections and four Permasense guided wave sensors attached to it. Thickness measurements were obtained over a period of 4 months and consistent results were acquired using the wireless guided wave sensors. To assess the real-time thinning of the carbon steel pipe sections, an engineering scale test loop was designed and a potential simulant (sand water slurry) has been proposed. A test plan was developed to vary the volumetric concentration of the simulant being circulated though the test loop for a period of about 7 months while using the Permasense sensors for detection and measurement of potential erosion/corrosion in the pipe sections.

## INTRODUCTION

---

The Hanford Site Tank Farm has implemented a Fitness-for-Service (FFS) program for the Waste Transfer System. The FFS program, based on API-579-1/ASME FFS-1, examines structural parameters of the waste transfer systems in order to develop erosion/corrosion rates for relevant system components. The FFS information is acquired from opportunistic evaluations of pipelines that have been removed from service. FIU-ARC engineers work closely with key Hanford high level waste (HLW) personnel and the contractor, Washington River Protection Solutions, LLC (WRPS), to support the FFS program, deliver solutions for sensor evaluations, conduct bench-scale testing followed by data acquisition and analysis for corrosion and erosion assessment.

The objective is to assist DOE and WRPS in providing realistic estimates of the remaining useful life of the components and to incorporate those estimates into future design plans. Previous efforts at Hanford included the installation of sensors on a number of the POR 104 components, to provide real time pipe wall thickness measurements. Due to various limitations, alternative approaches for remote permanently mounted pipe wall ultrasonic thickness measurement systems are being investigated.

FIU efforts to support this scope have included investigating key options available in the market for remote permanently-mounted ultrasonic transducer (UT) systems for HLW pipe wall thickness measurements. Specific applications include straight sections, elbows and other fittings used in jumper pits, evaporators, and valve boxes. FIU assessed the use of various ultrasonic systems that are either commercially available or used previously at Hanford and selected the most promising systems for further evaluation. One of the two down selected systems (Permasense UT sensor system) was acquired and initial bench-scale validation testing was conducted.

Currently, FIU is in the process of implementing the real-time thickness measurement in an engineering scale test set-up. A design loop has been established using 2- and 3-inch diameter straight and bend pipe sections to mount the sensors. The loop will be eroded using a sand-water slurry and the Permasense sensors will be used for thickness measurements.

The proposed research will provide information that will assist engineers with understanding the failure potential of HLW transfer components due to corrosion and erosion. This information can assist in determining if and when lines need to be removed, saving time and resources on unneeded excavation of transfer lines. This information can also assist engineers with designing new transfer systems by establishing more detailed/accurate guidelines governing the life expectancy of the transfer system and its components.

## PERMASENSE UT SENSOR EVALUATION

---

After efforts by WRPS to obtain real time thickness measurements using a pipe wrap system were found to be difficult [1], FIU began investigating alternative approaches to obtain the thickness measurements. Some of the operating parameters for the sensors include their need to be able to take measurements via permanent mounting and be installed in confined spaces. To this end, FIU investigated a variety of ultrasonic sensors for measuring the thickness of 2- and 3-inch diameter pipes. A majority of the companies that carry relevant transducers did not have products that met the site needs. In particular, most sensors evaluated required the use of a liquid couplant. For this application of long-term real-time measurements, a dry couplant is more practical.

After initial discussions with WRPS engineers, FIU purchased an Olympus 45MG Digital Ultrasonic Thickness Gage [2]. The system is a dual crystal transducer that comes with a two-step reference block and a liquid couplant sample. Hence, a dry couplant was purchased and tested. The results showed that the dry couplant was unable to provide accurate readings. In addition, vacuum tests were also conducted to eliminate the air gap between the test piece and the sensor surface. These results were also found to be highly inaccurate.

Hence, other options without the use of a gel couplant were investigated. Four of the options considered were: Ultrason sensors, Permasense sensors, Acellent smart sensors, and electromagnetic acoustic sensors (Innerspec EMAT). Descriptions of the UT sensors and the experiments conducted have been presented in the previous year end report. The down selected Permasense UT sensor system and its bench-scale validation testing are described here.

In addition, SRNL developed a replaceable erosion/corrosion coupon that detects the mass loss due to erosion using a gravimetric method. It is also designed to obtain and study the surface roughness profiles from wear and pitting corrosion. The coupon can hold a pencil UT sensor for real-time measurements. This testing will also be incorporated into the current work at FIU.

### **Permasense Guided Wave Sensors**

This system was developed by a UK based manufacturer, Permasense [4], and is shown in Figure 89(a). The Permasense UT system is an integrated wireless system [Figure 89 (b)] and uses a novel guided wave technology for acoustic wave propagation. This UT sensor system provides actual thickness measurements in pipes and can be used on 2-inch diameter pipes and elbows. It can also be customized for mounting with a mechanical clamping system [Figure 89 (c)]. The limitations include an expensive data acquisition system and only 2 sensors can be installed on the circumference of a 2-inch diameter pipe. This is to avoid cross-talk between the sensors in the limited space.

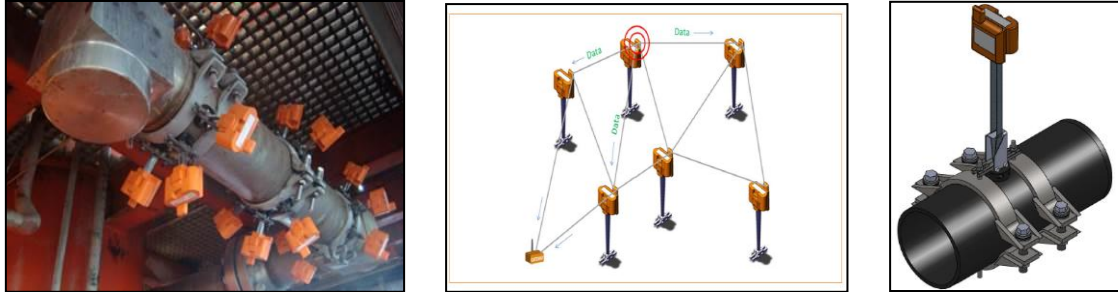


**Figure 89. (a) UT sensors, (b) Wireless network, and (c) Mounting system.**

These sensors have proven applications in oil and gas industries and similar areas. As a recent example, erosion/corrosion monitoring using the permanent mount Permasense system in European refineries has been successfully implemented. Thinning of pipes was determined based on real-time continuous monitoring.

The sensors are capable of operating up to 600°C (1100°F). This is due to their patented waveguide technology that holds the sensor head (with ultrasonic transducers, electronics, and battery) away from the hot metal. The sensor’s measurements are transmitted wirelessly back to a gateway (wireless access point) mounted near the main unit. A system schematic is shown in Figure 90(a).

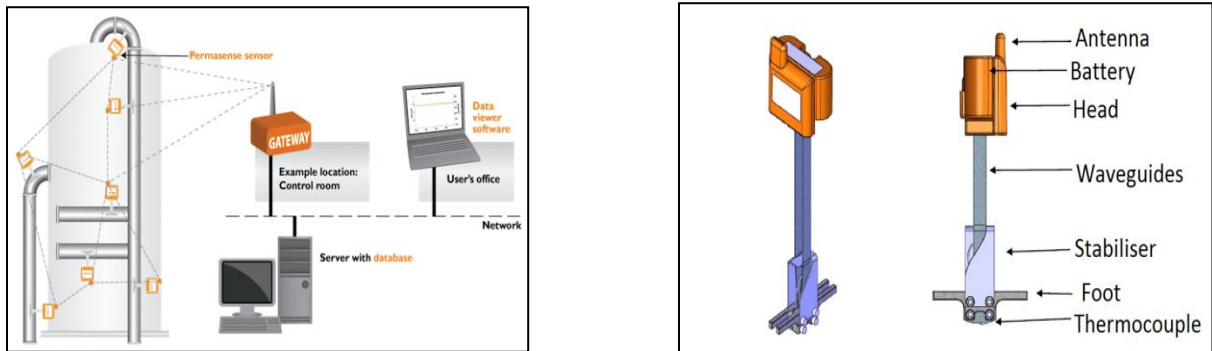


**Figure 90. (a) Permasense corrosion monitoring system and (b) Permasense WT 210 series UT sensor [4].**

Since there is no cost associated with measurement acquisition or measurement retrieval, the frequency of measurement can be configured to be as frequent as every 15 minutes. Connection of the gateway to the operator’s existing information technology infrastructure allows the data to be viewed from personnel desks. Sensor battery life of up to 10 years allows continuous data delivery between turnarounds without access to a sensor’s physical location.

The WT-210 series sensor is as shown in Figure 90 (b). It consists of the 304 stainless steel wave guides, sensor head, antenna, battery and a stabilizer. In addition, there is a built in thermocouple probe to monitor the pipe surface temperature which also allows the wall thickness measurement to be temperature compensated when required. The sensors communicate using the wirelessHART protocol, creating a self-forming and self-managing wireless mesh, which delivers continuous wall thickness measurements.

## Experimental Testing

Preliminary test setup and validation/verification of the obtained Permasense sensors has been conducted. The design of the test loop for circulating the simulant is currently being finalized and the construction of the loop and execution of the testing will follow. Each of these is explained briefly in the following sections.

### Preliminary Bench-Scale Test Setup and Sensor Validation

The bench-scale test set up was constructed using a pipe section that included 2- and 3-inch diameter carbon steel pipe sections. In this set up, both straight and 90° elbow sections were used and joined by a reducer.

Once the pipe sections were welded, the sensors were installed by the Permasense personnel as per the requirements. Figure 91 shows the installed sensors, one on the 2-inch elbow and the other on the 3-inch straight section. It should be noted that the installation required a specific torque (30Nm/22 lbf-ft) applied to the clamps to completely eliminating the air gap between the sensor tip and the test surface. The clamps were custom designed for each section.

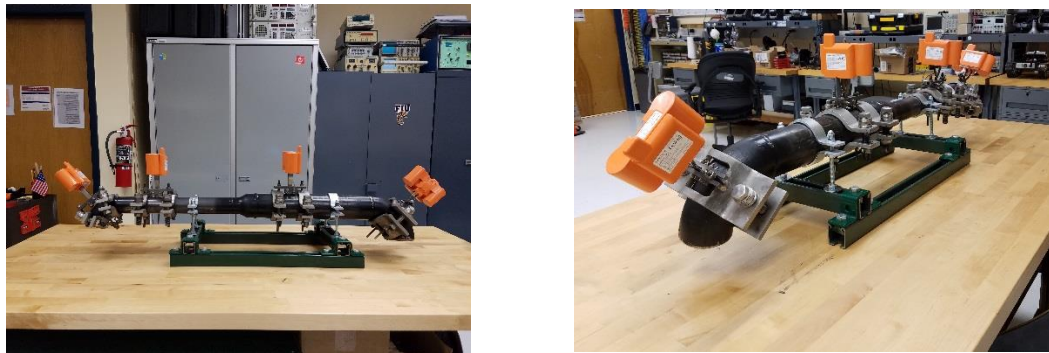


**Figure 91. Permasense sensor system a) on pipe section b) detailed view.**

Bench-scale testing of the sensors consisted of thickness data acquisition for a period of 4 months in order to verify the system's accuracy and robustness in measuring pipe thicknesses. Upon installation of the sensors, the system was integrated with a wireless Gateway and software (consisting of SQL server database) for data collection and analysis. The wireless gateway (from Emerson) has a range of 10-150 ft. from the sensors. The software has the capability to record real time data approximately every 15 minutes. It was configured to collect data every six hours.

The sensors have collected data for over 4 months. A typical output of the excel spreadsheet generated by the software is provided in Table 12. From the table, it is evident that the thickness readings were stable up to two decimal places of accuracy throughout testing.

**Table 12. Sample UT Sensor Measurements for 3-in Straight Section**

ID	Name	Sent Time	UT measurement (mm)	Temperature (°C)	Temp. compensation Flag
#00001	3 inch straight	10/25/2016 18:09	5.487	19.93	1
#00001	3 inch straight	10/25/2016 18:13	5.483	19.87	1
#00001	3 inch straight	10/26/2016 9:54	5.489	18.9	1
#00001	3 inch straight	10/26/2016 9:57	5.483	19.49	1
#00001	3 inch straight	10/26/2016 11:04	5.484	19.84	1
#00001	3 inch straight	10/26/2016 11:17	5.483	19.93	1
#00001	3 inch straight	10/26/2016 17:20	5.487	19.55	1
#00001	3 inch straight	10/26/2016 23:24	5.488	19.22	1
#00001	3 inch straight	10/27/2016 5:27	5.49	19.61	1
#00001	3 inch straight	10/27/2016 11:31	5.489	19.17	1
#00001	3 inch straight	10/27/2016 17:34	5.489	19.61	1
#00001	3 inch straight	10/27/2016 23:37	5.488	19.25	1
#00001	3 inch straight	10/28/2016 5:41	5.488	18.87	1
#00001	3 inch straight	10/28/2016 11:44	5.489	18.9	1
#00001	3 inch straight	10/28/2016 17:47	5.488	19.61	1
#00001	3 inch straight	10/28/2016 23:50	5.489	19.55	1
#00001	3 inch straight	10/29/2016 5:54	5.489	19.93	1
#00001	3 inch straight	10/29/2016 11:58	5.485	19.93	1
#00001	3 inch straight	10/29/2016 18:00	5.487	19.55	1
#00001	3 inch straight	10/30/2016 0:03	5.488	19.61	1
#00001	3 inch straight	10/30/2016 6:06	5.488	18.63	1
#00001	3 inch straight	10/30/2016 12:09	5.489	19.61	1

In addition, sample 2-inch elbow measurements from October 2016 to January 2017 are provided in the plot shown in Figure 92. The maximum thickness was measured to be 4.346 mm and the minimum value was 4.336 mm. The average for the sample data was 4.340 mm and the standard deviation of the data was 0.0015.

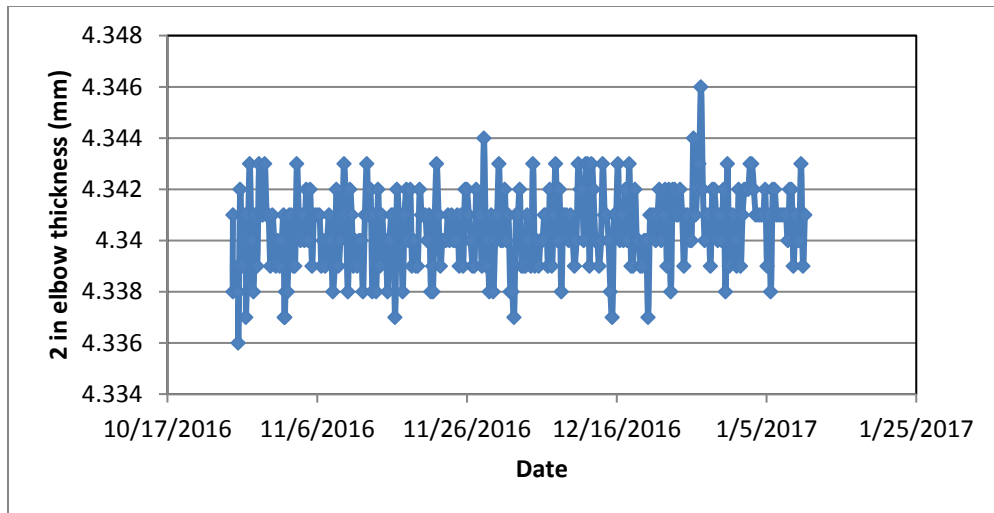


**Figure 92. Sample thickness measurements for 2 in elbow section from Oct 2016 to Jan 2017.**

Results during the testing period showed that there was no significant change in the average readings, demonstrating the stability of the system. In addition, the thickness readings matched the manufacturer’s specified thickness.

**Experimental Test Loop**

For the next phase of this effort, measurements of wear rates on the pipes will be obtained in real time. One of the methods for obtaining the data is to circulate a caustic/abrasive fluid such as NaCl,

$\text{Na}_2\text{SO}_4$ ,  $\text{NaOH}$ ,  $\text{HCl}$  or a sand/water solution through a closed loop pipe section to record the thinning of the pipe using the UT sensors. Of the solutions considered, the sand/water solution was selected since it is environmentally friendly and significant erosion can be obtained in a relatively short period of time. Caustic solutions generate fumes at high temperatures and require rigorous safety handling and disposal procedures. An initial design of the test loop is shown in Figure 93. This design incorporates 2- and 3-inch diameter schedule 40 carbon steel straight pipe sections along with long radius elbows and a reducer. The loop is approximately 6 ½ ft x 7 ft in dimension and will consist of a pump and a reservoir to circulate the simulant. The reservoir will be a 70 gallon vertical polyethylene tank with a stirrer/mixer. The design includes a bypass with steel ball valves to control the flow of the simulant as the pump does not have a variable frequency drive (VFD). The loop will consist of several sections attached with flanges and connectors for ease of installation and removal/replacement, as needed. In addition, instrumentation such as flow meters and temperature sensors will be installed in the test loop. The flow meters will act as flow measuring stations to record the flow that will be varied as per the test matrix to simulate various flow conditions. Temperature sensors may also be needed when the simulant temperatures are varied.

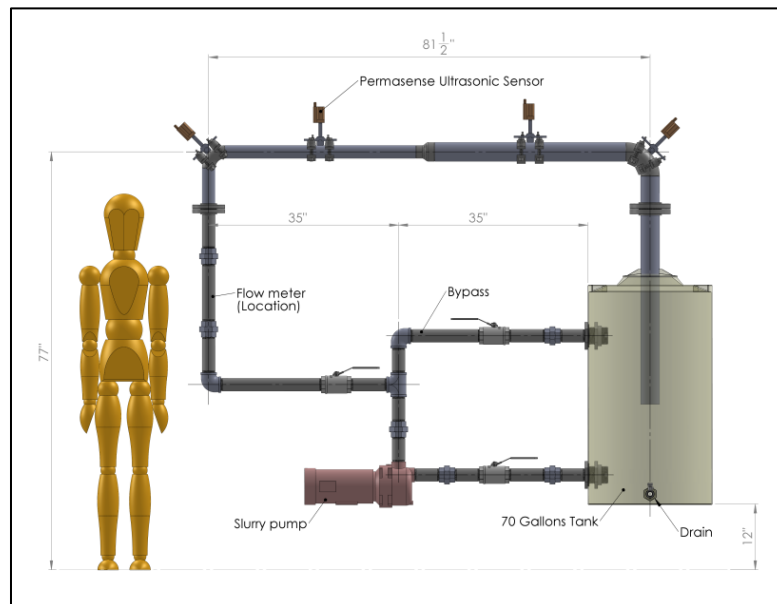


**Figure 93. Pipe loop design for aging.**

A total of four Permasense sensors will be placed on the 2- and 3-inch diameter straight and bend pipe sections (elbows) of the loop as shown in the figure. For the initial testing, as described in the previous section, the sensors were installed by the manufacturer. Currently, FIU is looking into procedures of removing and replacing the sensors on the new simulant loop design with the assistance of the Permasense manufacturer.

An important feature in the test loop will be a slurry pump that can handle abrasive simulants and generate flow velocities up to 2.5 m/s and flow rates up to 110 gpm. The maximum values are based on typical flow requirements needed for erosion found in the literature [8]. A number of pumps were evaluated for this purpose and the candidate selected is a 3 HP self-priming centrifugal pump with 230 V, 12.5 amps, 1 phase, 2-inch inlet/outlet and a maximum head of 60 ft (Figure 94). The slurry pump, manufactured/distributed by Dayton [7], includes a stainless steel impeller

which makes it suitable for corrosive media. It can also handle solids up to 1 inch in diameter and can pump liquids with temperatures up to 160°F.



**Figure 94. Pump for sand water media [5].**

### SRNL Coupon Testing

With support from SRNL, FIU testing will also include their coupon system developed for erosion corrosion. The fabricated erosion coupon is made of stainless steel and is designed in a way such that it can: (a) be used in a weight loss method, (b) house a pencil UT sensor, and c) be removed and tested for surface roughness. The installation of the coupon and a UT sensor probe on an elbow is shown in Figure 95.



**Figure 95. a) Coupon, b) Coupon installed on an elbow.**

The erosion/corrosion coupon developed by SRNL has significant beneficial features. It provides the ability to measure extremely low values of mass loss ( $\sim 0.00001$  g), thickness changes (0.0001 inch) and surface roughness profiles, while minimizing the disruption of the flow field in the process system.

The replaceable coupon is designed to minimize scratching or other deleterious effects that may occur during installation and removal. An index mark is provided so it can be reinserted, if desired, in the same orientation. The coupon holder is designed with a polymeric sleeve to isolate the coupon from vibration, which could cause material loss by fretting. In addition, the holder provides electrical isolation from the piping system, thereby eliminating galvanic effects between the pipe and the coupon. The coupon is designed to optimize accurate placement (location and angle) of the high resolution UT system, eliminating human error and thus providing repeatable, precise

real-time (in situ) thickness measurements. The coupon and holder can be scaled to fit multiple pipe sizes or installed in other system configurations (e.g., vessels or under nozzles) and is designed to meet ASME pressure vessel requirements.

**Testing**

As discussed previously, there are several simulant options for circulation in the test loop to determine real-time wear rate. Out of the options, the first stage of testing will use a sand and water solution due to its ease of procurement, testing and disposal. Based on the results obtained during the first phase of testing, other options (chemicals such as NaOH) might be considered in future tests. The schedule for sand-water testing is given in Table 13. The sand media used will be up to 10% of solids by volume and the size of the sand particles will be typically 200, 600 and 900 microns. The volume concentration and size of the particles for testing have been selected based on similar literature values [8, 9].

**Table 13. Sand and Water Testing**

<b>Simulant</b>	<b>Circulation Period (estimated)</b>
Water (loop validation)	1 week
Sand and water slurry (5%)	3 months
Sand and water slurry (8%)	2 months
Sand and water slurry (10%)	2 months

The test loop will be constructed as indicated in the design (Figure 93) and the testing will be conducted based on the schedule above to measure real-time thinning of the carbon steel pipe sections. The measurements will be obtained every 6 hrs. and the data will be analyzed to determine if modifications to the system need to be made.

With support from SRNL, the FIU testing phase will also include their coupon system as described in the previous section. The use of the replaceable erosion coupon could facilitate shorter duration wear tests. Depending on the active degradation mechanism, the replaceable coupon may provide validation of thickness change by using three independent measurement techniques: high resolution UT, conventional micrometer and weight loss.

## CONCLUSIONS

---

Each of the UT sensor systems mentioned in the previous section have certain advantages and limitations. Based on discussions with the site engineers, two of the options have been down selected for further investigation. These include the Permasense guided wave technology and the Ultrason couplant free sensors. Selections were based on applicability to various pipe sizes, ability to determine thicknesses accurately, and cost. One of the major challenges associated with a custom built remote permanently mounted UT system for pipe wall thickness measurements is the pricing of the systems.

FIU has acquired the Permasense sensors and validated the sensors for accurate static measurements of the 2- and 3-inch diameter pipe sections. This has been accomplished by the installation of the Permasense sensors on a custom built pipe layout to replicate typical waste transfer system pipe fittings. Initial bench-scale validation results have led to the next stage in engineering scale testing of the sensors under real-time thinning using a sand-water slurry.

Currently, FIU is designing a full-scale test set up to monitor and measure the erosion-corrosion in pipe sections using the Permasense guided wave sensors. The UT sensors and their wall loss measurement ability will be tested and validated under various environmental conditions such as humidity and temperature. For practical implementation, an environmental chamber will be built enclosing a section of the test loop.

In addition, FIU will also be incorporating a novel application developed by SRNL for corrosion detection. SRNL developed a replaceable erosion/corrosion coupon to measure the mass change (loss or gain) and to obtain and study the surface roughness profiles obtained from wear and pitting corrosion while conducting real-time UT sensor measurements.

## REFERENCES

---

1. B. J. Vasquez, RPP – RPT – 55812, Engineering Evaluation of Remote Permanently Mounted Pipe Wall Ultrasonic Thickness Measurement Devices, Rev 0, Washington River Protection Solutions, Richland, WA.
2. [www.olympus-ims.com](http://www.olympus-ims.com)
3. Aravelli, A., McDaniel, D. and Davila C., “Assessment of Guided Wave Ultrasonic Transducer Systems for Wall Thickness Measurements”, Summary Document submitted to DOE –EM under Cooperative Agreement # DE-EM0000598 (FIU-ARC-2016-800006470-04c-242).
4. [www.permasense.com](http://www.permasense.com)
5. Philip T. and Jake D., “Monitoring and simulation resolves overhead corrosion – online corrosion monitoring in tandem with simulation modelling identified the root cause of corrosion in a crude unit overhead”, [www.eptq.com](http://www.eptq.com) – PTQ Q1 2016.
6. <https://www.grainger.com/product/LITTLE-GIANT-1-8-HP-PPS-115-230V-Magnetic-2P043>.
7. [https://www.grainger.com/ec/pdf/4YU37\\_1.pdf](https://www.grainger.com/ec/pdf/4YU37_1.pdf).
8. Wood R. J. K and Jones T. F., “Investigations of sand–water induced erosive wear of AISI 304 stainless steel pipes by pilot-scale and laboratory-scale testing”, *Wear*, Vol. 255, Issue 1-6, Aug-Sep 2003, Pg. 206-218, <http://www.sciencedirect.com/science/article/pii/S0043164803000954>.
9. Naz., M. Y., Ismail, N. I., Sulaiman, S. A., Shukrullah, S., “Characterization of erosion of gas pipelines by dry sand”, *Instrumentation Science and Technology*, 2017, VOL. 45, NO. 1, 62–72. <http://dx.doi.org/10.1080/10739149.2016.1194295>
10. Morris, K., “Investigation of Various Water Sources on the Corrosion of Carbon Steel and Aluminum”, 2017, Honors Research Project, Dept. of Chemical Engineering, University of Akron, OH, USA.
11. <http://hghouston.com/resources/technical-newsletters/corrosion-in-caustic-solutions>
12. Lu, B., “Erosion-Corrosion in Oil and Gas Production”, *Research and Reviews in Materials Science and Chemistry*, Vol. 2, Issue 1, 2013, Pages 19-60, ISSN 2319-6920.

## **TASK 19.2**

# **EVALUATION OF NONMETALLIC COMPONENTS IN THE WASTE TRANSFER SYSTEM (FIU YEAR 7)**

### **EXECUTIVE SUMMARY**

---

Nonmetallic materials are used in the United States Department of Energy's Hanford Site Tank Farm waste transfer system. These materials include the inner primary hoses in the hose-in-hose transfer lines (HIHTLs), Garlock<sup>®</sup> gaskets, ethylene propylene diene monomer (EPDM) O-rings, and other nonmetallic materials. These nonmetallic materials are exposed to  $\beta$  and  $\gamma$  irradiation, caustic solutions as well as high temperatures and pressure stressors. How the nonmetallic components react to each of these stressors individually has been well established. However, simultaneous exposure of these stressors has not been evaluated and is of great concern to Hanford Site engineers.

FIU engineers worked closely with key Hanford HLW personnel to develop an experimental test plan to determine how these nonmetallic components react to various simultaneous stressor exposures. The materials selected for testing included EPDM and Garlock<sup>®</sup> coupons, EPDM HIHTL inner hoses and EPDM O-rings as well as Garlock<sup>®</sup> gaskets. An experimental test loop was constructed and the components were aged for durations of 180 and 365 days. The system can accommodate eighteen component assemblies. Each assembly consisted of one EPDM HIHTL, one EPDM O-ring and one Garlock<sup>®</sup> gasket. There were three assembly aging sets, one for each temperature. Each set has six assemblies in it; three for each of the two time periods.

Prior to aging of the components, a sample set was mechanically tested to obtain various baseline properties as per ASTM standards. The aging of the materials involved exposing each sample to a 25% NaOH solution at ambient (38°C), operating (54°C) and design temperatures (79°C) for durations of 180 and 365 days. After aging/conditioning, the mechanical and material properties of the aged samples were measured and compared with the baseline results to obtain an understanding of degradation caused by the stressors. This report provides results from mechanical property testing of EPDM and Garlock<sup>®</sup> material coupons as well as the blowout/leak testing for HIHTL, EPDM O-rings and Garlock<sup>®</sup> gaskets after a 180-day aging period only since the material testing for the 365-day aged samples had not been conducted at the time of reporting. Results showed the difference in the HIHTL blowout pressures to be within the error margins while a more significant difference was observed with the material tensile testing. An 88% and 57% reduction in the average tensile strength was observed with the Garlock<sup>®</sup> and the EPDM materials, respectively, when compared to their baseline tensile strength. In addition, analysis using a scanning electron microscope with energy dispersive X-ray spectroscopy (SEM-EDS) was conducted on the EPDM inner hose samples to determine how far the NaOH penetrated into the ethylene propylene diene monomer (EPDM). Preliminary results show that the sodium hydroxide is penetrating into the inner hose at the higher temperatures.

## INTRODUCTION

---

Nonmetallic materials are utilized in the waste transfer system at the Hanford tank farms; these include the inner hose of the hose-in-hose transfer lines (HIHTLs), Garlock® gaskets and ethylene propylene diene monomer (EPDM) O-rings. These materials are exposed to simultaneous stressors including  $\beta$  and  $\gamma$  radiation, elevated temperatures, caustic supernatant as well as high pressures during normal use. In 2011, the Defense Nuclear Facilities Safety Board recommended to the U.S. Department of Energy (DOE) to conduct post service examination of HIHTLs and Teflon gaskets to improve the existing technical basis for component service life. Suppliers of the nonmetallic components often provide information regarding the effects of some of the stressors, but information is not provided for simultaneous exposure. An extensive test plan was developed by Sandia National Laboratories to understand the simultaneous effects of the aforementioned stressors [1]; however, this test plan was never executed. Additional studies conducted by Lieberman provides information on HIHTLs at elevated temperature and pressure but little information is gained regarding the synergistic effects with the caustic supernatant [2]. FIU has been tasked with supporting this effort by conducting multi stressor testing on typical nonmetallic materials used at the Hanford tank farms.

This report provides the mechanical property testing of EPDM and Garlock® material coupons as well as the blowout/leak test results for HIHTL, EPDM O-rings and Garlock® gaskets after a 6-month aging period. In addition, the experimental test loop used to age the test specimens is described.

## EXPERIMENTAL TESTING

All material samples had their baseline mechanical performance and properties tested as per ASTM standards prior to any exposure. Once the baseline properties were determined, each material sample was aged, which involved exposing each sample to a chemical simulant at ambient (38°C), operating (54°C) and design temperatures (79°C) for durations of 180 and 365 days. Tests were conducted on both material coupons as well as in-service configuration assemblies. After aging/conditioning, the mechanical properties of the samples were again measured as per ASTM standards.

### *In-Service Configuration Aging*

The in-service configuration aging experimental setup consisted of 3 independent pumping loops with two manifold sections on each loop (Figure 96). Each of the 3 loops was run at a different temperature (38°C, 54°C and 79°C). Each manifold section held three test samples and was used for a corresponding exposure time of 6 months and 1 year. Each test sample consisted of a HIHTL hose section, an EPDM O-ring and a Garlock® gasket placed in a series configuration. Isolation valves on each manifold allowed for removal of samples without affecting the main loop and the rest of the samples. The temperature of the chemical solution circulating within each loop was maintained at a preset temperature by an electronically controlled heater. A 25% sodium hydroxide solution was used as a chemical stressor that circulated in each of the loops. The chemical stressor's pH was checked every 30 days to ensure that the concentration levels remained constant.

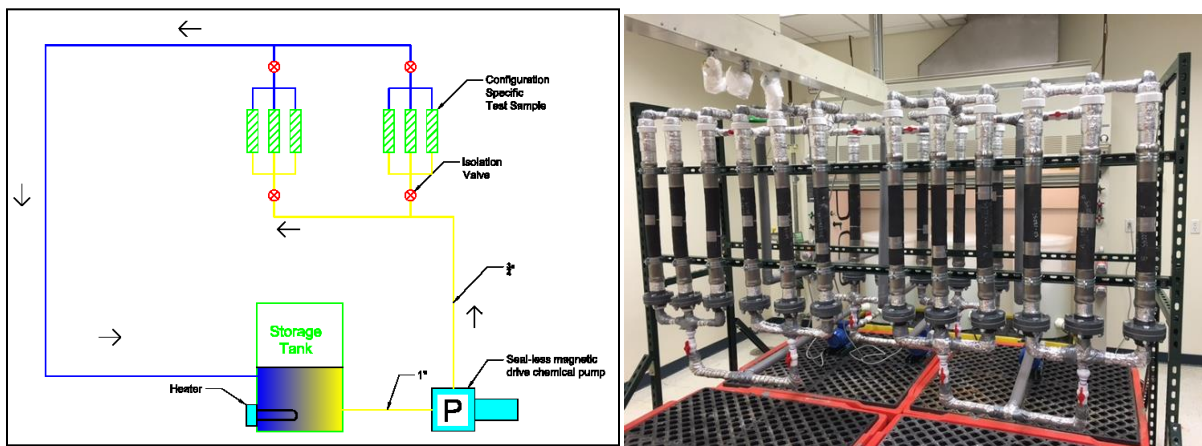


Figure 96. In-service component aging loop.

The coupon aging experiment setup consisted of one coupon aging vessel submerged in each of the three test loop’s storage tanks. This resulted in exposing the coupons to the same conditions as the in-service configuration tests; the circulating fluid is the same 25% sodium hydroxide solution. Each vessel contained 12 coupons (6 of each type of EPDM and Garlock® materials) and was submerged in the bath for duration of 180 and 365 days.

## 6-Month Testing Results

### *Hose-In-Hose*

Three sample hoses from each loop were pressurized until rupture. Their pressure profiles as well as initial and final lengths were measured. The rupture pressure was compared to the baseline values. Figure 97 shows the results of the 6-month aged hose burst pressure tests and Figure 98 shows a ruptured hose section.

As can be seen from Figure 97, the burst pressure profiles for the hoses aged at the various temperatures do not show a significant degradation in the average burst pressures of the hoses when compared to the average baseline results. A maximum degradation of 168 psi was observed between the baseline and the hoses aged at the highest temperature of 79°C. The hoses aged at the mid temperature of 54°C resulted in an average degradation of only 21 psi while the hoses aged at the coolest temperature of 38°C resulted in an average degradation of 99 psi. An interesting observation is that the hoses aged at the coolest temperature (38°C) resulted in a greater degradation in their average burst pressure than the hoses aged at the mid temperature (54°C). This might indicate that when the temperature is below a certain point, the effect it has on the hose strength is negligible. This hypothesis can be verified once the burst pressure tests are conducted on the hoses aged for 365-days.

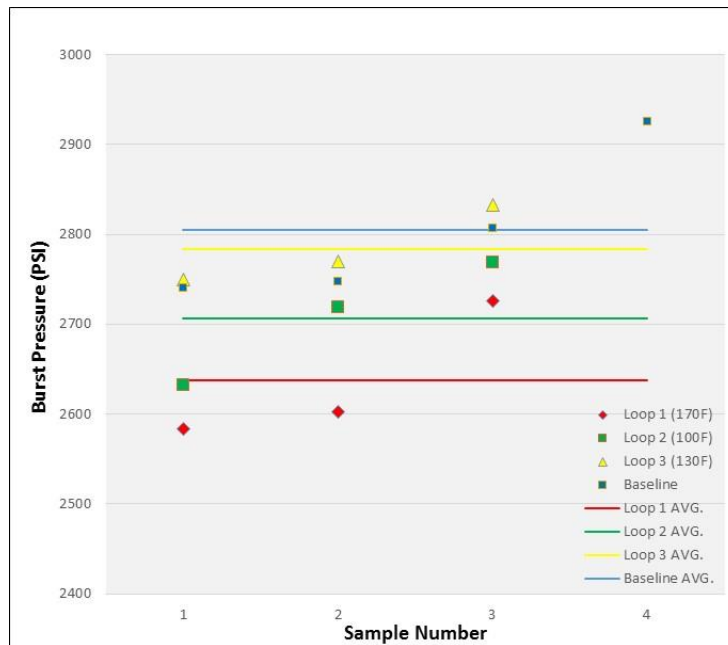


Figure 97. HIHTL burst pressure profiles.



Figure 98. Ruptured hose section.

**EPDM O-Ring Testing**

The aged O-ring pressure testing was conducted for nine EPDM O-ring specimens (three from each loop). Table 14 shows the results of the testing and Figure 99 shows the O-ring test apparatus. An average pressure of 1650 KPa was maintained for five minutes without any leaks.

**Table 14 . 6-month O-Ring Pressure Test Results**

Sample Number	O-01-4	O-01-5	O-01-6	O-02-4	O-02-5	O-02-6	O-03-1	O-03-2	O-03-3	Average
Water Temperature (°C)	23.00	23.00	22.00	22.00	22.00	22.00	22.00	22.00	22.00	22.22
Ambient Temperature (°C)	26.00	26.00	24.00	24.00	24.00	24.00	26.00	26.00	26.00	25.11
Humidity (%)	65.00	66.00	85.00	85.00	85.00	85.00	76.00	76.00	76.00	77.67
Holding Pressure (Pa)	1.63E+06	1.61E+06	1.61E+06	1.65E+06	1.61E+06	1.63E+06	1.68E+06	1.72E+06	1.75E+06	1.65E+06
Pressure Maintained?	Yes	N/A								
Time Until Failure (s)	N/A									



Figure 99. O-ring test apparatus.

**6-Month Garlock® Gasket Testing**

The aged Garlock® gaskets pressure testing was conducted for nine Garlock® gasket specimens (three from each loop). Table 15 shows the results of the testing and Figure 100 shows the test apparatus. Of the nine specimens, only four gaskets were able to maintain pressure. Of the four that maintained pressure, an average pressure of 487 KPa was maintained for five minutes without any leaks. The leaks are believed to be due to the gaskets being compressed when they were installed in the aging loop. Since the Garlock® material maintains a memory after it has been compressed, when it is reinstalled into the pressure test rig, it does not always create a good seal.

**Table 15. 6-Month Garlock® Gasket Testing Results**

Sample Number	G-01-4	G-01-5	G-01-6	G-02-4	G-02-5	G-02-6	G-03-1	G-03-2	G-03-3	Average
Water Temperature (°C)	22.44	22.44	22.44	22.44	22.44	22.44	22.44	22.44	22.44	22.44
Ambient Temperature (°C)	26.67	26.67	26.11	26.11	26.11	26.11	26.11	26.11	26.11	26.23
Humidity (%)	50.00	50.00	54.00	54.00	54.00	54.00	54.00	48.00	53.00	52.33
Holding Pressure (Pa)	1.09E+06	1.12E+06	1.12E+06	0.00E+00	1.05E+06	0.00E+00	0.00E+00	0.00E+00	0.00E+00	4.87E+05
Pressure Maintained?	Yes	Yes	Yes	No	Yes	No	No	No	No	N/A
Time Until Failure (s)	N/A	N/A	N/A	0.00	N/A	0.00	0.00	0.00	0.00	N/A



**Figure 100. Gasket test apparatus.**

**6-Month Coupon Testing**

Three of the EPDM and Garlock® samples were aged in each of the three loop tanks maintained at 38°C, 54°C and 79°C, respectively. All procedures used for testing were derived from the ASTM D412-16 standard [3]. Figure 102 and Figure 103 show results from the tensile strength tests for the EPDM and Garlock® coupons, respectively, while Figure 104 shows a comparison of the results to the baseline data.

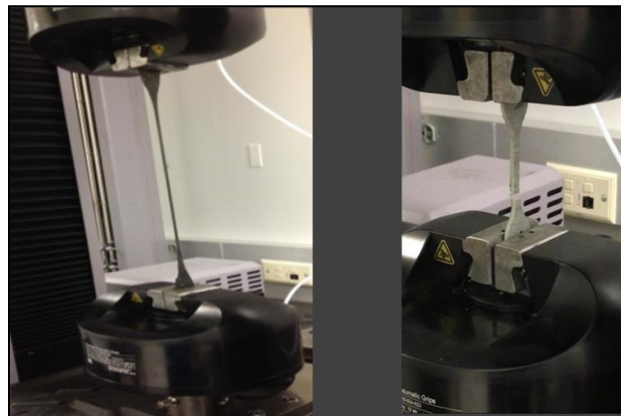


**Figure 101. Tensile strength testing of EPDM and Garlock® coupons.**

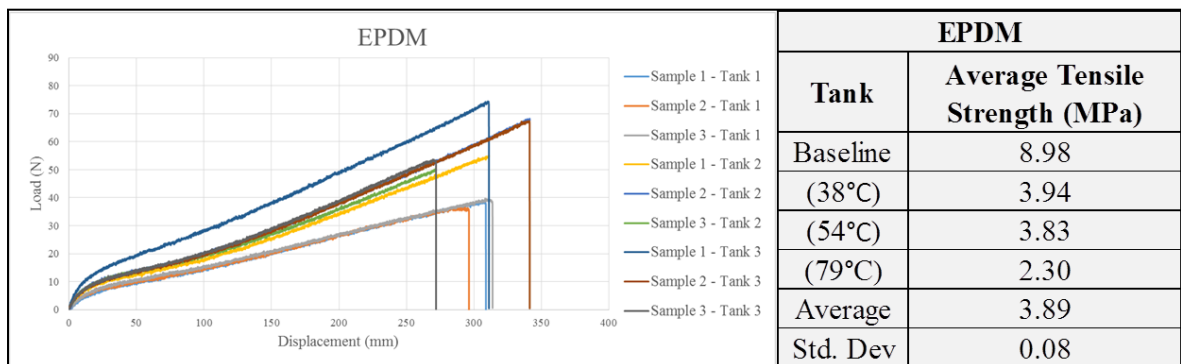


**Figure 102. EPDM coupon tensile strength.**

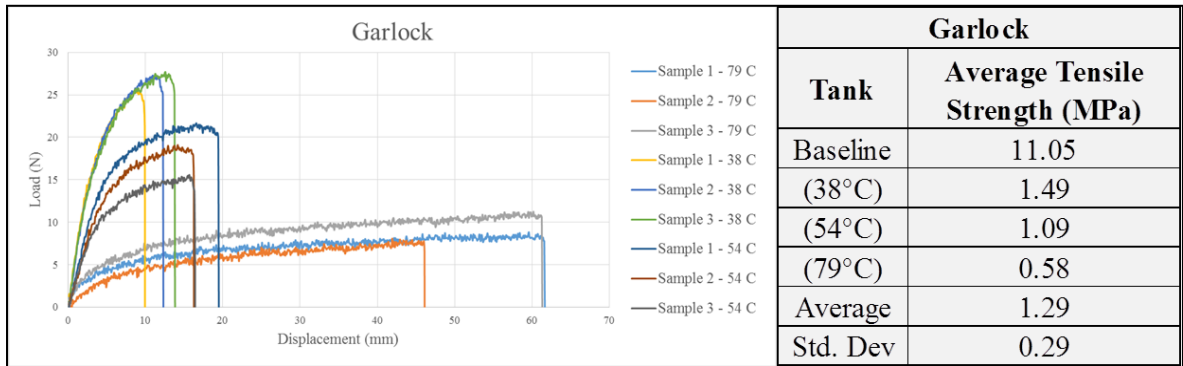


Figure 103. Garlock® coupon tensile strength.

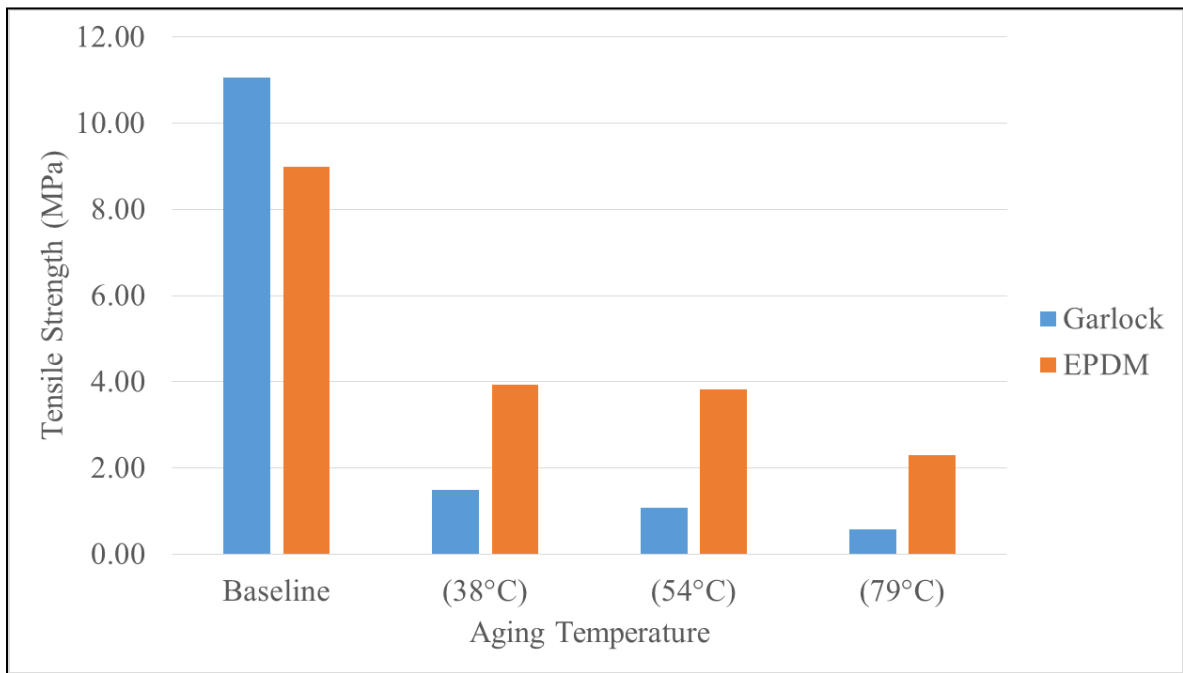


Figure 104. Coupon tensile strength comparison to baseline data.

As can be seen from Figure 102, Figure 103 and Figure 104, even though the Garlock® material has a higher initial strength than the EPDM, it loses much of its strength when exposed to the caustic solution. This could be the result of Garlock® being comprised of a paper-type material that loses its strength when it becomes wet. Even when Garlock® material is wet, a trend in strength degradation can be seen as the solution temperature increases. A similar trend is observed with the EPDM material; as the temperature increases, its tensile strength decreases. An 88% and 57% reduction in the average tensile strength was observed with the Garlock® and the EPDM materials, respectively, when compared to their baseline tensile strength.

Sample coupons were taken from the hoses used during the 6-month burst pressure tests as well as the non-aged hoses (Figure 105). As can be seen in Figure 106, the aged coupon (on bottom) from loop 1 (79°C) has a discoloration on its inner surface when compared to the un-aged coupon sample. The discoloration appears to be only on the surface of the material and does not appear to have penetrated into the material.



**Figure 105. Hose sample coupons.**



**Figure 106. Aged (bottom) vs. un-aged (top) coupons.**

Analysis using a scanning electron microscope with energy dispersive X-ray spectroscopy (SEM-EDS) was conducted on the EPDM inner hose samples. The intention was to determine how far the NaOH penetrated into the ethylene propylene diene monomer (EPDM). Figure 107 shows the results from the unaged (baseline) sample. As expected, there is no NaOH found within the EPDM. Figure 108 shows the results of the hose sample aged for 6-months at 79°C. As can be seen in the figure, there are signs of both sodium and calcium present within the sample. From these preliminary results, it appears that the sodium hydroxide is penetrating into the inner hose at the higher temperatures. Once the results from the lower temperature samples are obtained, FIU can correlate how the temperature effects the penetration of the NaOH into the EPDM hoses. In addition, the samples will be analyzed in order to determine the source of the calcium inside the samples.

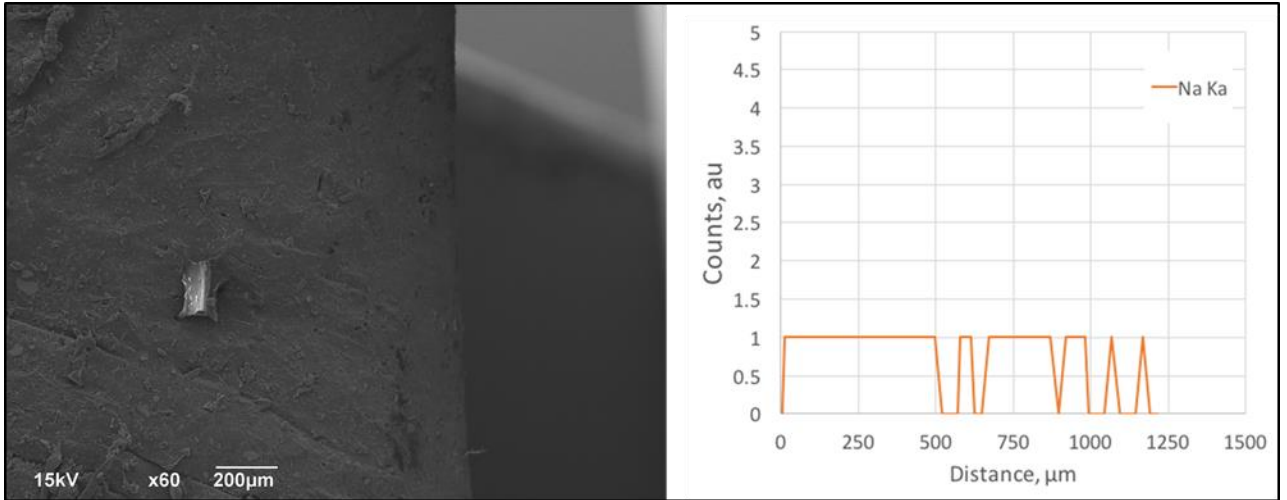


Figure 107. Unaged (baseline) hose sample.

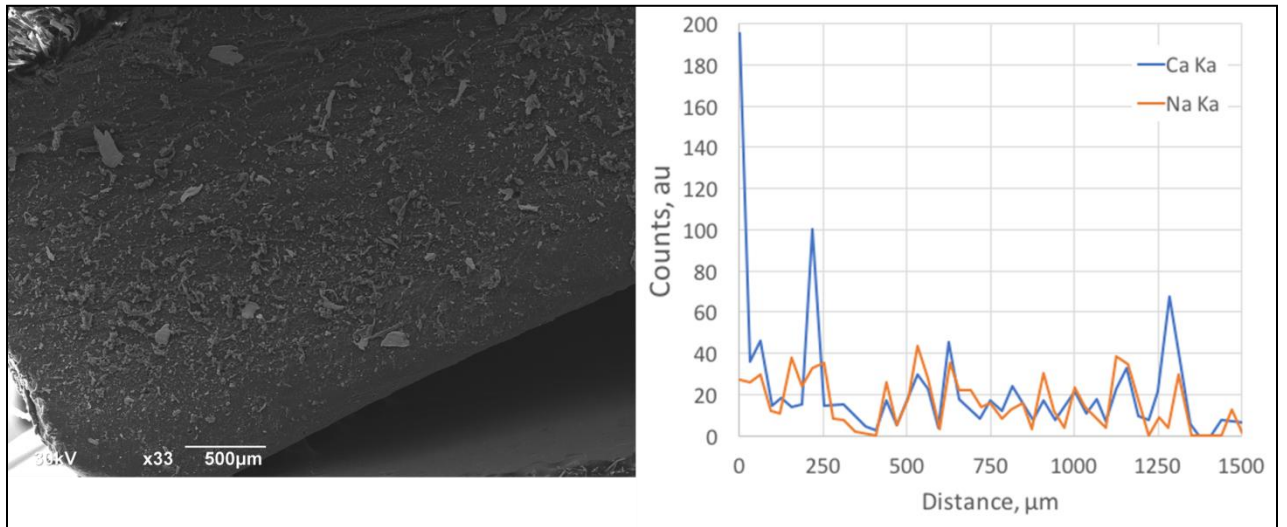


Figure 108. 6-Month aged hose sample (79°C).

## CONCLUSIONS AND FUTURE WORK

---

After analyzing the experimental data from the six-month aged samples, minimal degradation was observed in the bursting pressure of the hoses aged at the different temperatures. When compared to the baseline results, a maximum degradation of around 1100 Kpa was observed. However, when the tensile strength of the material coupons were analyzed, a much greater degradation was observed. When the average tensile strength of the EPDM and the Garlock<sup>®</sup> coupons aged at 79°C were compared to the baseline samples, a degradation of 75% and 95% in the tensile strength was observed for the EPDM and the Garlock<sup>®</sup> samples, respectively. When analysis using a scanning electron microscope with energy dispersive X-ray spectroscopy (SEM-EDS) was conducted on the EPDM inner hose samples, the sodium hydroxide was observed to have penetrated into the material at the 79°C temperature. The SEM-EDS analysis of all the hose samples is ongoing. Therefore, a complete comparison cannot be done at this time. Also, even though the one-year coupon aging has been completed, the material analysis has not yet begun. The next phase of testing will include conducting burst pressure tests on the one-year aged hose specimens as well as the tensile tests on the EPDM and the Garlock<sup>®</sup> material coupons samples. In addition, the SEM-EDS analysis of the six-month as well as the one-year hose specimens will be completed. After all the tests have been conducted and the data analyzed, additional testing phases may be considered. This may include the effects of elevated pressure in addition to elevated temperature and exposure to caustic solutions. Additional materials may also be evaluated, including the use Teflon and Tefzel.

## REFERENCES

---

1. H Brush, C. O. (2013). Test Plan for the Irradiation of Nonmetallic Materials. Albuquerque, New Mexico: Sandia National Laboratories.
2. Lieberman, P. (2004). Banded (Band-It) and Swaged Hose-In-Hose (HIHTL) Assembly Service Life Verification Program. Santa Clarita, California: National Technical Systems.
3. ASTM D412-16 Standard Test Methods for Vulcanized Rubber and Thermoplastic Elastomers—Tension, ASTM International, West Conshohocken, PA, 2016, <https://doi.org/10.1520/D0412-16>